

Time Series Searching, Forecasting, and  
Classification with Applications in Bioinformatics  
時系列の探索・予測・分類とその生命情報学  
への応用

Coleman Yu  
余 浩旻



# Abstract

Time series data are ubiquitous across many different fields. Much of the data are inherently time series data. Additionally, some data, such as strings, images, and object shapes, that are not originally time series data, can be transformed into time series. Many data mining tasks, such as classification, clustering, and motif finding, have been defined for time series data. Hence, by developing appropriate transformation methods, we can apply a plethora of well-established time series methods to our problems.

This thesis contributes three aspects in time series data mining and bioinformatics. They are a novel application of time series classification to solve complex biological problems by transforming biological data into time series, developing a more expressive distance measure framework that removes certain underlying assumptions, and using nearest neighbors as covariants to improve the performance in the task of forecasting.

In the first part, we demonstrate the utility of time series analysis in bioinformatics by studying the problem of predicting Human Dicer Cleavage Sites. Recall that bioinformatics operates at the intersection of biology, biotechnology, and informatics. In this work, we formulate a specific biology problem, which is predicting Human Dicer Cleavage sites in microRNA biogenesis, into a machine learning framework. In particular, this is a multivariate time series classification problem, which is the informatics component of bioinformatics. Due to current limitations in biotechnology, we are constrained to using 1-D RNA sequence inputs rather than 2-D or 3-D data, because these are more expensive to obtain. We propose MTSCCleav, a method that encodes RNA sequences and the probabilities of base pairs in predicted secondary structures into time series data. To the best of our knowledge, we are the first to make use of the probabilities of base pairs in this kind of classification task on RNA data. By doing this, we frame the problem of predicting Human Dicer Cleavage sites into a Multivariate Time Series Classification (MTSC) problem. Existing approaches rely on opaque deep neural networks or complex feature engineering. They are slow, and the

feature engineering is over-designed. In contrast, our approach is simple, intuitive, and computationally efficient. The proposed transformation methods allow us to use any well-established time series tools to analyze this biological problem. Experiments demonstrate that MTSCCleav achieves comparable and even better accuracy to state-of-the-art methods while delivering a 3.7X to 28.8X speedup. Furthermore, our perturbation experiments reveal that regions near the center of pre-miRNAs are essential for cleavage-site prediction, consistent with the existing literature.

In the second part, we address the limitations of existing similarity measures. Similarity search is a core subroutine in time series data mining tasks. For example, recent studies show that a simple 1-NN classifier with an appropriate distance measure can outperform many advanced, complicated methods. While Dynamic Time Warping (DTW) and Uniform Scaling (US) are prevailing measures for handling local distortions and global scaling, respectively, and some studies have demonstrated that combining both DTW and US is necessary to obtain meaningful results. Current approaches apply a single scaling factor to the entire sequence. We argue that since distinct phases of a process often evolve at different speeds, a single scaling factor is insufficient. We introduce the first distance measure framework, namely PSD, that achieves invariance to multiple scaling factors. We also provide speed-up techniques to enable efficient computation of the PSD. Experiments show that PSD better reflects the similarity between time series with multiple phases, and that the identified phases (segmentation) provide a clearer understanding of the data.

In the third part, we study a time series primitive, namely matrix profile, in the application of time series forecasting. For a given time series  $T$  and an integer  $m$ , the matrix profile provides the information about (1) the location of its nearest neighbor and (2) the distance between it and the nearest neighbor of **each**  $m$ -subsequence in  $T$ . Obviously, the matrix profile also provides us the information for the  $k$ -nearest neighbors of each subsequence simply by running the same algorithm for  $k$  times. In our application, we are only interested in the left nearest neighbors of each subsequence because they refer to the historical occurrences. We can obtain the immediate subsequences of these historical occurrences as covariates to feed into the forecaster to improve its accuracy. Experiment shows that these covariates, which can be obtained through a computationally cheap data mining primitive called Matrix Profile, can improve the existing forecaster.

Collectively, this thesis advances the fields of time series data mining and bioinformatics by demonstrating the use of time series analysis to address fundamental

biological questions, proposing a new, more expressive distance measure framework, and using augmented properties (i.e., the information related to the nearest neighbors) of subsequences to enhance the prediction.



# Acknowledgements

To begin, I want to express my deepest gratitude to my PhD supervisor at Kyoto University, Prof. Tatsuya Akutsu. I thank him for his kindness and patience. He is a brilliant researcher who can explain complex concepts simply. In a seminar, he showed that simply using clear notation makes presentations much easier to follow. More importantly, he helps students when they are in “valleys” in their lives. When a car is off track, it needs a push—so do people. I am equally indebted to my MPhil supervisor at The Hong Kong University of Science and Technology (HKUST), Prof. Raymond Chi-Wing Wong. He has continued to help and advise me even after I graduated from HKUST.

Akutsu-sensei taught me the importance of reading good materials. In the weekly seminars, he organized reading seminars, assigning some of his favorite books for us to read and discuss. His favorite book is “Probability and Computing” by Mitzenmacher and Upfal. Additionally, through the journal club he organized, students were asked to present the core ideas from their ten selected papers published in leading venues, such as Nature, Science, Cell, and PNAS. Reading beyond my fields helped me identify research gaps others missed. I think some great ideas are born when we merge the ideas from different fields. He also emphasized the importance of mathematics and proof. It is what computer scientists can stand out in the field of bioinformatics. I think it becomes especially true now, since advances in AI make it possible for almost everyone to code (i.e., Vibe coding). He advised me to use the existing tools, libraries, and studies to leverage my own research. He also taught me that a good researcher must master both oral and written presentation; otherwise, others may misinterpret your talent and the effort you put in. When we are reading a paper, he urges us to identify the novelty and analyze the pros and cons of the paper.

Raymond taught me the power of focus and “First Principles”. I was always surprised that he did not use reference management software like Zotero, preferring to annotate hard copies and even type .bib files manually. He told me that when he starts to do research, he will print out the papers and get focused on the

stack of papers (hard copies) in front of him. I am not saying it is beneficial not to use tools, but I want to emphasize the power of focus that underlies his work routine. He taught me that every good research starts with a set of good papers. He also emphasized that there is no right or wrong in research, only what you choose to do about it. His research receipt works as follows. When you are tackling a problem, you first review the relevant existing studies to understand the state of the art (SOTA) for it. If the existing work addresses your particular problem, you can apply and adapt it to your problem setting. But most of the time, since your problem must be a particular version of a general problem, the existing general solution should not work well for it. It means that you have some room to improve it. And this is the research gap!. It reminds me of when we deal with the NP-complete problem. As Kleinberg and Tardos's Algorithm Design (Chapter 10) suggests, an NP-complete problem (assuming  $P \neq NP$ ) does not allow us to have an algorithm that possesses all three of the following desired properties simultaneously: Efficiency, Correctness, and Generalization. Hence, it is sometimes preferable to address a specific instance of the problem rather than the general one. He also emphasized the theory. He consistently noted that you need to add theory to the paper to strengthen it. He always mentioned that you need three motivations (why you are doing it) and three contributions (what you have done). Sometimes, I ask why he can write so fast, and he replies, "If you know what you are doing, then you write fast.". He also taught me that when you don't know some of the ideas, you just go back to the original idea. Doing a "deep first search" can help you reach the first principle, a concept that Elon Musk, one of the greatest entrepreneurs of our time, always emphasized.

Without these two supervisors, I would not have made it this far. I could not have finished this program.

I would like to take this opportunity to share some of my thoughts on my PhD journey. I hope the readers may learn something from what I have gone through. My PhD journey was, to quote Dickens, "the best of times and the worst of times", and to quote Churchill, "This was their finest hour". For the best parts, it allows me to explore both in my daily life and in my research. I tried many things, walked many roads, drank many colas and alcohol, and met many people. This helped me see problems from new perspectives. Regarding the worst parts, I am reminded of a quote from one of my favorite movies, "Les Choristes": "Fond de l'étang". It literally means "Bottom of the Pond". At times, I felt like a frog at the well's bottom, trying hard to get out. Research is fun but also hard. Research is about exploring something new. It is about publishing (so others can learn from

it). When I am stuck, the best solution is to aim for a reachable, well-defined goal. The goal should be clear, with obvious rewards and requirements. Also, make sure the effort of your actions can be accumulated. Like the frog, do not jump randomly, but aim to move to stable platforms towards escape. Then, each jump matters for your progress. Two of the materials helped me; they are “Eat the Frog!” and “THE PH.D. GRIND”.

I would like to thank my thesis committee members, Prof. Tatsuya Kawahara and Prof. Hisashi Kashima. I appreciate their willingness to serve as committee members, to provide me with valuable advice. I would like to acknowledge Tamura-sensei and Mori-sensei (a former member) of the Akutsu laboratory. Tamura-sensei taught me to focus on the input-output relationship when encountering new algorithms/methods, and Mori-sensei introduced me to the fascinating application of time-series analysis to gene expression data, especially in trajectory inferences (i.e., pseudotime). I would like to thank the many communities that made my life in Japan colorful. Thank you to the people of the dormitories where I lived at the Uji and Yoshida campuses. I am grateful to my Japanese language teachers. I also cherish the friends I met through Akutsu’s laboratory and the extracurricular activities, including Kendo, Table Tennis, Naginata, Karate, and Aikido. I also met many interesting people from various international student events.

I am honored to receive the Asian Future Leaders Scholarship Program (AFLSP) scholarship to support my studies in Japan. I have made a great choice by enrolling in Kyoto University Design School, which has provided me with many valuable interdisciplinary experiences and opportunities to meet people outside my field. In this program, I have conducted fieldwork in Okinawa, Hong Kong, and Bali, a rare opportunity for researchers in computer science. I would also like to thank the Institute for Chemical Research (ICR) for the Research Assistant position in the Akutsu laboratory.

Finally, I would like to express my deepest gratitude to my family and my friends who have stayed by my side with their countless acts of support; I have nothing to return to them but my love and time.

A special acknowledgment goes to my niece. As you grow up, I hope you explore the world and fulfill your eagerness for knowledge. Find materials that interest you. One day, you might find this thesis online and, I hope, find it worth reading and inspiring.



# List of Publications

This thesis is based on the following papers.

- (Chapter 3) **Coleman Yu**, Raymond Chi-Wing Wong, and Tatsuya Akutsu, “MTSCCleav: a Multivariate Time Series Classification (MTSC)-based Method for Predicting Human Dicer Cleavage Sites”, submitted to *IEEE Access*, under review
- (Chapter 4) **Coleman Yu**, Tatsuya Akutsu, and Raymond Chi-Wing Wong, “Scaling with Multiple Scaling Factors and Dynamic Time Warping in Time Series Searching”, submitted to *IEEE Access*, under review
- (Chapter 5) **Coleman Yu**, Raymond Chi-Wing Wong, and Tatsuya Akutsu, “Leveraging Nearest Neighbors for Time Series Forecasting with Matrix Profile”, in preparation

Other publications

- **Coleman Yu** and Raymond Chi-Wing Wong, “A Melody Composer for both Tonal and Non-Tonal Languages”, the 43rd International Computer Music Conference 2017, Shanghai, China on 16-20 Oct, 2017
  - In this study, we apply a data mining method called frequent pattern mining to capture the relationships between the pitch trend in the melody and the tone trend in lyrics and use these relationships to create a new melody for the user-given lyrics. The pitch trend and the melody trend are both time series data. It motivates me to conduct research about time series analysis from a data mining perspective. Through this study, I have a chance to apply the data mining techniques in a completely different field.
- Yi Zheng, Bogdan Enescu, Jianchang Zhuang, and **Coleman Yu**, “Data replenishment of five moderate earthquake sequences in Japan, with semi-automatic cluster selection”, *Earthquake Science*, 34:310-322, 2021

- In this study, we apply a data mining method called DBSCAN, which is a clustering method, on seismicity data, to automatically select the nearest significant earthquake cluster of a given mainshock. The clustering results are then fed into a downstream replenishment method to discover missing early aftershocks, which follow relatively large or moderate earthquakes.

## Poster presentations

- **Coleman Yu** and Tatsuya Akutsu, “Aligning gene expression time series with invariance to uniform scaling with multiple scaling factors”, International Workshop on Bioinformatics and Systems Biology, Boston, USA (IBSB 2018) on 16-18 July, 2018
  - In this study, we present an idea that, for time series analysis, rather than focusing on the whole sequence analysis, it is more important to focus on the subsequences of a time series. In this poster, we use gene expression data as an example to explain. Genes are expressed over time. But the expression rate is not a constant. The varying rate would be discussed in Chapter 4. The importance of the subsequence has been discussed in the framework of time series forecasting in Chapter 5. We use a data mining primitive called Matrix Profile. Given a subsequence  $Q$  with length  $m$ , we can find the nearest neighbor (location and the similarity of it with  $Q$ ) in another time series  $A$ . The underlying distance metric is z-normalized ED. If  $Q$  is an  $m$ -subsequence extracted from  $A$ , it means that we annotate each  $m$ -subsequence with its nearest neighbor information. To demonstrate that this nearest-neighbor information is useful, we use it to improve a time-series forecasting model. If information is useful covariates, the performance can be improved. In addition, the usage of finding useful covariates to improve the final prediction results has also been demonstrated in Chapter 3. In that example, we find a covariate, which is the secondary structure, associated with the probability of each base pair, for the mRNA sequence data, as shown in Figure 3.1.

# Contents

|   |      |
|---|------|
| <b>Abstract</b>   | i    |
| <b>Acknowledgements</b>   | v    |
| <b>List of Publications</b>   | ix   |
| <b>List of Figures</b>  | xv   |
| <b>List of Tables</b>   | xvii |
| <b>1 Introduction</b>   | 1    |
| 1.1 Background . . . . .  | 1    |
| 1.2 Contributions . . . . .   | 2    |
| 1.3 Organization . . . . .  | 2    |
| <b>2 Preliminaries</b>  | 5    |
| 2.1 Distance Measures . . . . .   | 5    |
| 2.1.1 Euclidean Distance (ED) . . . . .   | 6    |
| 2.1.2 Dynamic Time Warping (DTW) . . . . .  | 7    |
| 2.1.3 Derivative Dynamic Time Warping (DDTW) . . . . .  | 7    |
| 2.1.4 Weighted Dynamic Time Warping (WDTW) . . . . .  | 7    |
| 2.1.5 Weighted Derivative Dynamic Time Warping (WDDTW) . .  | 8    |
| 2.1.6 Shape Dynamic Time Warping (shapeDTW) . . . . .   | 8    |
| 2.1.7 Amercing Dynamic Time Warping (ADTW) . . . . .  | 9    |
| 2.2 Classification . . . . .  | 10   |
| 2.2.1 Ridge Classifier . . . . .  | 10   |
| <b>3 MTSCCleav: a Multivariate Time Series Classification (MTSC)-based Method for Predicting Human Dicer Cleavage Sites</b> | 13   |
| 3.1 Background . . . . .  | 14   |

|          |   |           |
|----------|---|-----------|
| 3.2      | Methods . . . . .   | 17        |
| 3.2.1    | Data Preparation . . . . .  | 18        |
| 3.2.2    | Time Series Encoding . . . . .  | 21        |
| 3.2.3    | Time Series Classification . . . . .  | 25        |
| 3.2.4    | Evaluation Metrics . . . . .  | 28        |
| 3.3      | Results . . . . .   | 29        |
| 3.3.1    | Channel Ablation Study . . . . .  | 30        |
| 3.3.2    | Predictive Performance . . . . .  | 32        |
| 3.3.3    | Running Time Analysis . . . . .   | 34        |
| 3.3.4    | Subsequence Importance . . . . .  | 35        |
| 3.3.5    | Summary . . . . .   | 35        |
| 3.4      | Discussion . . . . .  | 36        |
| 3.5      | Concluding Remarks . . . . .  | 37        |
| <b>4</b> | <b>Scaling with Multiple Scaling Factors in Time Series Searching</b>               | <b>39</b> |
| 4.1      | Background . . . . .  | 40        |
| 4.2      | Related Work . . . . .  | 43        |
| 4.3      | Preliminaries . . . . .   | 44        |
| 4.3.1    | Euclidean Distance (ED) . . . . .   | 45        |
| 4.3.2    | Dynamic Time Warping (DTW) . . . . .  | 45        |
| 4.3.3    | Uniform Scaling (US) . . . . .  | 48        |
| 4.3.4    | Uniform Scaling & Dynamic Time Warping (USDTW) . . . . .                            | 49        |
| 4.3.5    | Lower Bounds for DTW and USDTW . . . . .  | 49        |
| 4.4      | Piecewise Scaling Distance . . . . .  | 53        |
| 4.4.1    | Piecewise Scaling & Dynamic Time Warping (PSDTW) . . . . .                          | 55        |
| 4.4.2    | Speedup Techniques . . . . .  | 57        |
| 4.4.3    | Guided Distance . . . . .   | 62        |
| 4.5      | Experiments . . . . .   | 62        |
| 4.5.1    | Experimental Setup . . . . .  | 62        |
| 4.5.2    | Experimental Results . . . . .  | 65        |
| 4.6      | Concluding Remarks . . . . .  | 69        |
| <b>5</b> | <b>Leveraging Nearest Neighbors for Time Series Forecasting with Matrix Profile</b> | <b>71</b> |
| 5.1      | Background . . . . .  | 71        |
| 5.2      | Related Work . . . . .  | 75        |
| 5.3      | Method . . . . .  | 76        |

|                     |  |           |
|---------------------|--|-----------|
| 5.3.1               | Problem Formulation . . . . .                      | 77        |
| 5.3.2               | Evaluation Method . . . . .                        | 78        |
| 5.3.3               | Gradient Boosting Regression Tree (GBRT) . . . . . | 79        |
| 5.3.4               | Matrix Profile . . . . .                           | 80        |
| 5.4                 | Experiments . . . . .                              | 82        |
| 5.5                 | Concluding Remarks . . . . .                       | 84        |
| 5.5.1               | Future Work . . . . .                              | 84        |
| <b>6</b>            | <b>Conclusion and Future Directions</b>            | <b>87</b> |
| <b>Bibliography</b> |  | <b>91</b> |



# List of Figures

|     |  |    |
|-----|--|----|
| 2.1 | Alignments. . . . .  | 6  |
| 3.1 | Predicted secondary structure of the sequence $S$ of pri-miRNA “hsa-let-7a-1” <sup>1</sup> . Experimental evidence suggests that the two deviated mature miRNAs are $UGA \cdots GUU$ and $CUA \cdots UUC$ . They are $S(6 : 27)$ and $S(57 : 77)$ (Both ends are inclusive.). The ends are highlighted in <b>bold</b> . Since $S(6 : 27)$ ( $S(57 : 77)$ ) is near the 5’ (3’) end, we call it “5p (3p) mature miRNA”. The two scissors indicate the two cleavage sites. The color intensity of the nodes reflects their base-pair probability in this predicted secondary structure. The deeper the color, the higher the probability. The unpaired nodes are uncolored. The raw figure is generated by RNAfold web server <sup>2</sup> . . . . . | 15 |
| 3.2 | The overall pipeline of this study. Symbol notations: Cylinder - Dataset, Rectangle - Process, Parallelogram - Input / Output, Rounded Rectangle - Component. . . . .  | 17 |
| 3.3 | Relationship of the proposed encoding methods. . . . .   | 21 |
| 3.4 | Features generation in the transformation . . . . .  | 26 |
| 3.5 | Convolutions of HYDRA for each input time series with a set of random kernels $w$ , organized into $g$ groups with $k$ kernels each. . . . .   | 27 |
| 3.6 | CD diagrams of channel ablation study. . . . .   | 32 |
| 3.7 | CD diagrams to compare different classifiers. . . . .  | 34 |
| 3.8 | CD diagrams to compare different encoding methods. . . . .   | 34 |
| 3.9 | Results of the perturbation experiment. . . . .  | 36 |
| 4.1 | Applying nearest neighbor interpolation on $Q$ , which result in Scaled $Q$ , that can better reflect its similarity with $C$ . . . . .  | 41 |
| 4.2 | $Q$ and $C$ are in different rates. A stretching version of $Q$ is similar to a prefix of $C$ , but not the whole $C$ . . . . .  | 41 |
| 4.3 | Intuition of piecewise scaling (PS). . . . .   | 42 |

|      |   |    |
|------|---|----|
| 4.4  | Z-normalization. Resulting time series have mean = 0 and std = 1.   | 45 |
| 4.5  | Visualization of $D$ with local constraints. The black cells form the warping path.   | 47 |
| 4.6  | Visualization of LB <sub>Keogh</sub> and LB <sub>Shen</sub>   | 51 |
| 4.7  | Relationship of $L_Q$ and $L_C$ .   | 59 |
| 4.8  | Visualization of the GunPoint dataset. Left (Right): A time series of the “Gun” (“Point”) scenario. Critical periods, such as “Aiming”, are annotated.  | 63 |
| 4.9  | The red solid time series shows an instant in the target set. The blue dashed time series shows an instant in the query set.  | 63 |
| 4.10 | Runtime and number of distance calls comparison of GunPoint dataset. (a)-(d) $P = 1$ , (e)-(h) $P = 2$ , (i)-(l) $P = 3$ .  | 67 |
| 5.1  | Flattening a 2D window of size $(1 + M) \times w$ to a 1D vector of length $w + M$ . The resulting vector serves as the <i>predictor</i> for the regressor. Its expected <i>response</i> is the vector of length $h$ . The regressor learns from this predictor-response pair. We also call the regressor a forecaster because it aims to forecast.   | 72 |
| 5.2  | The <i>left</i> ( <i>right</i> ) matrix profile and the <i>matrix profile</i> of a time series. The <i>matrix profile</i> shows the distances between each $m$ -subsequence and its nearest neighbor, where $m$ is a user-given value. The <i>left</i> ( <i>right</i> ) matrix profile shows the same information but is limited to its left (right) nearest neighbor. For a particular $m$ -subsequence shown by the right gray box, its nearest neighbor is the left gray box, as indicated by the dashed line in the <i>left matrix profile</i> and the <i>matrix profile</i> . Similarly, the nearest neighbor of the left gray box is the right gray box, as indicated by the dashed line in the <i>right matrix profile</i> and the <i>matrix profile</i> . The first (last) point in each box is denoted by a <i>red</i> circle (triangle). $h$ denotes the length of the immediate subsequence of the nearest neighbor. Intuitively, this subsequence should be similar to the immediate subsequence (i.e., future) of the right gray box. To note, the <i>left</i> ( <i>right</i> ) matrix profile starts (ends) at a later (earlier) index because the corresponding nearest neighbor with length $m$ does not exist. | 73 |

# List of Tables

|     |   |    |
|-----|---|----|
| 3.1 | Selected representative records from miRBase. For the last two columns, the first line shows the name, the second line shows its location in the original sequence, and the third line indicates whether its existence has experimental evidence. The selected one is highlighted in <b>bold</b> . . . . .            | 18 |
| 3.2 | The whole sequence of “hsa-let-7a-1” and its predicted secondary structure by RNAfold. The corresponding positions of the two mature miRNAs and the probability of the unpaired “U” are highlighted in <b>bold</b> . . . . .  | 19 |
| 3.3 | The first row shows the “four strings” of “hsa-let-7a-1”. Their complementary strands are shown in the second row. As a whole, they are referred to as the “eight strings”. . . . .   | 20 |
| 3.4 | Time series encoding. $P$ is the corresponding base-pair probability sequence of $S$ . $p_i = 1$ if we encode $S$ without incorporating base-pair probability sequence. . . . .   | 23 |
| 3.5 | Comparison of rocket-based classifiers [1]. $\mathcal{N}(0, 1)$ : a standard normal distribution, $U(0, 1)$ : a uniform distribution between 0 and 1, 1 <sup>st</sup> order difference: $\Delta T = t_2 - t_1, t_3 - t_2, \dots, t_n - t_{n-1}$ . . . . .   | 28 |
| 3.6 | Channel ablation study. The best results are highlighted in <b>bold</b> . . . . .   | 31 |
| 3.7 | Performance on the 45 combinations between encoding methods and the ROCKET-based classifiers. The best results are highlighted in <b>bold</b> . . . . .   | 33 |
| 3.8 | Comparative analysis between MTSCCleav with the best combination of the encoding method and classifier, with the SOTA, Di-Cleave, on the three datasets. The best results of using MiniROCKET have also been shown to compare the computational efficiency. The best results are highlighted in <b>bold</b> . . . . . | 33 |
| 4.1 | Details of the ten datasets for the experiments . . . . .   | 65 |

|     |  |    |
|-----|--|----|
| 4.2 | The accuracy comparison for eight distance measures of the GunPoint dataset . . . . .  | 66 |
| 4.3 | The accuracy comparison for six PSED-guided distance measures of the GunPoint dataset . . . . .  | 66 |
| 4.4 | The accuracy comparison for eight distance measures of the ten datasets . . . . .  | 68 |
| 4.5 | The accuracy comparison for six PSED-guided distance measures of the ten datasets . . . . .  | 68 |
| 4.6 | The number of distance calls and runtime on PSED_vanilla and PSED_parallel_bsf of the ten datasets . . . . .   | 69 |
| 5.1 | Dataset Statistics. $N$ is the number of time series in the dataset, while $ T  = n$ is the length of each time series. “rate” refers to the measuring rate. $w$ is the size of the look-back window. $h$ is the size of the forecasting window, also known as the forecasting horizon. $T_{\text{train}}$ is the training subsequence of $T$ . $T_{\text{test}}$ is the test subsequence of $T$ . To note, $ T_{\text{train}}  +  T_{\text{test}}  = n$ . . . . . | 83 |
| 5.2 | Experimental Results without original covariates (bold represents the best result and underlined represents the second best) (* refers to the results reported from [2]). . . . .  | 84 |
| 5.3 | Experimental Results with original covariates (bold represents the best result and underlined represents the second best) (* refers to the results reported from [2]). . . . .   | 84 |

# Chapter 1

## Introduction

### 1.1 Background

Human generates a ton of data nowadays. We are producing more new data in one single day today than in the first twenty-one centuries of AD combined. We are drowning in information but thirsty for knowledge. It is natural for us to develop computational methods to accelerate the process of “harvesting” knowledge from information.

Computational tasks focus on the relationship between input and output. We would like to find the hidden function behind. To note, there are two ways to solve a computational problem. One is the algorithmic approach, and the other is the machine-learning approach.

There are two large categories of machine learning. They are supervised learning and unsupervised learning. Classification may be the most intuitive form of supervised learning. The input is data points with labels. We learn a model from the relationship between data points and the labels. The model predicts the labels for the new data points. They have many applications. For example, in medical applications, it involves classifying patients as healthy or diseased, or tumors as benign or malignant. The term “supervised” means the model has access to labeled data. In other words, it requires labeled training examples that provide ground truth. So, the model can learn the boundary between the categories. Our first study focuses on a classification problem in biology.

A representative of unsupervised learning is undoubtedly clustering. We aim to group data into distinct clusters. The key difference is that the data lack predefined labels. By grouping them, we aim to identify natural patterns hidden in the data. One example is clustering cells based on their gene-expression profiles. These

clusters might reveal distinct cell types. Note that we do not have the ground truth for the cluster set. In bioinformatics, we typically use enrichment analysis to determine whether specific gene functions are enriched in these clusters. Cell types often show enrichment for genes responsible for specific functions. This set of genes defines their biological role. In clustering, we first need to define a measure of similarity between two objects and decide what details should be ignored. This is called invariance. For example, in image classification, it should be invariant to zooming and rotation.

## 1.2 Contributions

In this study, our contributions mainly include three parts. First, we demonstrate a machine learning approach to analyze a biology problem in chapter 3. We propose the usage of the base pair probability sequence from the predicted secondary structure of RNA sequence as new information (i.e., covariates) for the classification task. We apply Rocket-based classifiers to identify the human dicer cleavage sites. Because of the simplicity of the transformation method and the classifiers, our proposed method achieves 3.7X to 28.8X speedup while achieving better or comparable results than the current state-of-the-art method. Second, we solve an algorithmic problem on distance measure in Chapter 4. We propose a new distance measure framework, namely PSD, that can incorporate any existing distance measures to achieve invariance for two time series with multiple rates (i.e., different scaling factors). Experiments show that our methods outperform ED, DTW, and the other five DTW-based methods. Moreover, we propose using the segmentation result returned by PSD to improve the accuracy of other distance measures. Third, we improve a forecaster with the usage of a data mining primitive, namely Matrix Profile, in Chapter 5. We propose leveraging left nearest neighbors for each forecasting window as new covariates to improve the accuracy of the underlying forecaster. We use a simple gradient boosting regression tree as the underlying forecaster. The experiment shows that this simple method can improve the accuracy of the forecaster.

## 1.3 Organization

In Chapter 2, we review some of the basic knowledge in biology and time series data mining, in particular, we focus on distance measures and the main core underlying Rocket-based classifiers, which is the Ridge classifier. In Chapter 3, we introduce

our study of the problem of predicting human dicer cleavage sites. We proposed a novel approach to frame this task as a multivariate time series classification problem by introducing nine encoding methods and making use of Rocket-based classifiers. In Chapter 4, we introduce a new distance measure framework, namely PSD. It releases the assumption that there is only one scaling factor existing throughout the whole time series. In Chapter 5, we introduce how to create new covariates in time series forecasting using matrix profile. This method can improve the accuracy of the existing forecaster by providing useful covariates. In Chapter 6, we give a conclusion to these two studies and provide future work on them.



# Chapter 2

## Preliminaries

In this chapter, we provide background on time series, with a focus on distance measures and classification, particularly the ridge classifier, which is used in the ROCKET-based classifiers for time series classification. The remaining preliminary knowledge will be provided in the corresponding chapters. Section 2.1 gives an overview of the existing distance measures used in the evaluation in Chapter 4. Section 2.2 reviews the additional knowledge about the classifiers used in Chapter 3. We start with the definition of a time series.

### 2.1 Distance Measures

A general form of a time series  $T$  is an ordered pair of  $n$  real-valued variables,  $T = (b_1, c_1), (b_2, c_2), \dots, (b_n, c_n)$ , where  $b_i$  is the behavioral attribute and  $c_i$  is the contextual attribute, where  $1 \leq i \leq n$ .  $c_i$  refers to the time stamp at which the measurement  $b_i$  is taken. Since the measurements are always taken in a uniform manner,  $t_i$  is simply incrementing from 1 to  $n$  uniformly. Hence, we can represent a time series more concisely as  $T = t_1, t_2, \dots, t_n$ , where  $t_i = b_i$ .

We may be interested not only in the entire time series but also in a segment of it, called a subsequence. A subsequence  $T(i : j)$  of a time series  $T$  is a shorter time series, which is a contiguous subset of time points in  $T$ , that starts from position  $i$  and ends at position  $j$ . Formally,  $T(i : j) = t_i, t_{i+1}, \dots, t_j$ , where  $1 \leq i \leq j \leq n$ . We call  $T(1 : m)$  as the prefix of length  $m$  of  $T$ ,  $m$ -prefix in short.

To quantify the similarity between two time series, we need to define a distance measure, also known as a similarity measure, between them. Many distance measures have been proposed in the literature. Among them, the most established measures are undoubtedly Euclidean Distance (ED) and Dynamic Time Warping

(DTW). They are representatives of the two board classes of distance measures, namely “lock-step” and “elastic”.

### 2.1.1 Euclidean Distance (ED)

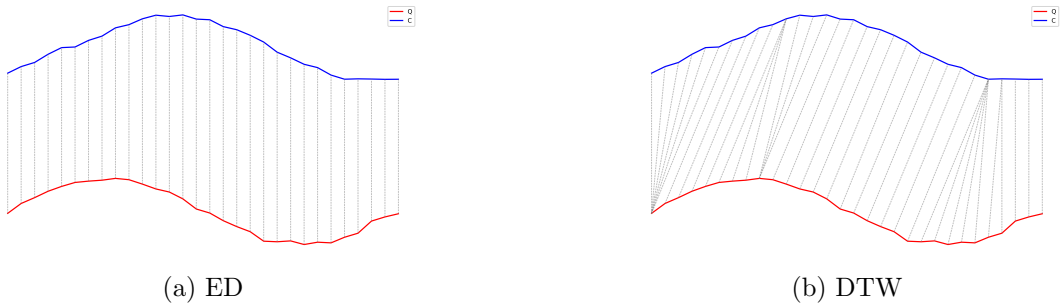


Figure 2.1: Alignments.

ED is a lock-step distance measure. Given two time series  $Q$  and  $C$  with the same length  $n$ , it compares the time point  $q_i$  of  $Q$  with the time point  $c_i$  of  $C$  at the same time (index). Note that, traditionally, lockstep distance measures require the two time series to have the same length because of the one-to-one alignment, as shown in Figure 2.1. However, in the setting of query by content, where it is always the case that  $|Q| < |C|$ , we can still apply a lock-step distance measure by either comparing  $Q$  with  $C(1 : |Q|)$  or padding  $Q$  using its last element to lengthen it to the same length of  $C$ . Minkowski distance is a generalization of Euclidean distance. Minkowski distance is the  $L_p$ -norm of the difference between the two time series  $X$  and  $Y$ , defined as:

$$D(X, Y) = \left( \sum_{i=1}^n |x_i - y_i|^p \right)^{\frac{1}{p}} \quad (2.1)$$

When  $p = 2$ , it corresponds to the Euclidean distance. When  $p = 1$ , it corresponds to the Manhattan distance. When  $p = \infty$ , it corresponds to the Chebyshev distance. In our studies, we focus on the Euclidean distance. Other lock-step distance measures include Pearson correlation distance. It accounts for the linear association between the two time series using the Pearson correlation coefficient. To note, there is another measure called Edit Distance for strings. And Edit Distance is also sometimes abbreviated as ED in string processing or bioinformatics. In this study, we focus on time series analysis and use ED to denote Euclidean distance rather than edit distance.

### 2.1.2 Dynamic Time Warping (DTW)

Dynamic Time Warping is an elastic measure [3]. In contrast to lock-step distance measures, elastic distance measures allow one-to-many point matching, as shown in Figure 2.1. The one-to-many point matching allows the elastic distance measures to warp in the time axis (i.e., temporally) such that it can handle the local temporal distortions. While it will be detailed in Chapter 4, it is briefly explained here. In short, it minimizes the cumulative distance between two time series, subject to constraints, by finding an optimal warping path  $W^*$  in a cost matrix, where  $W$  is the set of all possible paths. The constraints typically are (1) Boundary conditions, (2) Continuity, and (3) Monotonicity. This warping path provides feasibility for the point alignments to go beyond the 1-1 point alignment, as in the case of a lock-step distance measure,

### 2.1.3 Derivative Dynamic Time Warping (DDTW)

The Derivative Dynamic Time Warping (DDTW) is a variant of DTW [4]. Instead of comparing original raw values, it compares two time series using their first-order derivatives, but with an approximation. In DTW, a point on a rising trend may be mapped to a point on a falling trend. It goes against our intuition. It can be solved by comparing their first-order derivatives, which encodes the slope information. The derivative  $T'$  of a time series  $T$  is computed approximately as follows.

$$t'_i = \frac{(t_i - t_{i-1}) + \frac{t_{i+1} - t_{i-1}}{2}}{2} \quad (2.2)$$

This estimate is simply the average of “the slope of the line through  $t_i$  and  $t_{i-1}$  (i.e., its left neighbor)” and “the slope of the line through  $t_{i-1}$  (i.e., its left neighbor) and  $t_{i+1}$  (i.e., its right neighbor)”. The  $1/2$  term in the second item of the numerator comes from the fact that the separation in time of the  $t_{i-1}$  and  $t_{i+1}$  is 2. Note that the estimate is not defined for the first and last elements of the time series in the above equation. In these boundary cases, we use the estimates of the second and penultimate (i.e., the second-to-last thing) as the estimates for the first and last elements, respectively.

### 2.1.4 Weighted Dynamic Time Warping (WDTW)

The Weighted Dynamic Time Warping (WDTW) is a variant of DTW [5]. It is a penalty-based DTW designed to prevent pathological paths. Recall that a

warping window (e.g, Sakoe-Chiba band) is enforced on the cost matrix of DTW, such that some paths are excluded. Only the paths that reside entirely in the warping window are feasible. This constraint may be too strict. WDTW uses a softer way for the same purpose. Instead of using a window to forbid the alignment of  $x_i$  and  $y_j$  that are far away in time. WDTW weights the cost of such alignment by multiplying it by a modified logistic weight function (MLWF)  $\omega(k)$ , defined as follows.

$$\omega(k) = \frac{\omega_{\max}}{1 + \exp(-g \cdot (k - m_c))} \quad (2.3)$$

Where:

- $k = |i - j|$ . It is the phase difference (i.e., distance on the time axis from the diagonal. The diagonal refers to the line where  $i = j$ .)
- $\omega_{\max}$  is the desired upper bound for the weight parameter, which is suggested to be set to 1.
- $m_c$  is the midpoint of a sequence.  $m_c = m/2$ .
- $g$  is a constant that controls the level of penalization. It controls the curvature (slope) of the function.

Intuitively, if  $x_i$  and  $y_j$  are far apart temporally, it will have a larger weight to discourage their alignment and vice versa.

### 2.1.5 Weighted Derivative Dynamic Time Warping (WD-DTW)

[5] also proposed the weighted version of DDTW. In brief, a weight is applied to the local cost function when computing DTW on the first derivative.

### 2.1.6 Shape Dynamic Time Warping (shapeDTW)

The Shape Dynamic Time Warping (shapeDTW) is a variant of DTW [6]. The main modification to the original DTW is the way the local distance between points is computed. Recall that DTW compares single scalar points. shapeDTW compares local descriptors. The local descriptors are constructed using a sliding window on the original series, such that for each point  $x$ , a  $L$ -subsequence with  $x$  as the center is extracted to compute the higher-level feature of  $x$ .  $L$  is the user-given length of the subsequence to consider. By default, it is set to 15 in Aeon,

which is a time series library in Python. There are several ways to construct such a descriptor. For example, a raw subsequence (i.e., a set of neighbor points surrounding the point of interest), Piecewise aggregate approximation (PAA) [7, 8], slope, derivative, HOG-1D [9].descriptor.

Then, the distance between descriptors is calculated rather than between raw values. When a raw subsequence is chosen to construct the local descriptors, a common metric used for comparing two local descriptors is the Euclidean distance. In the evaluation, a raw subsequence is chosen to construct the local descriptors, which is the default setting in Aeon.

### 2.1.7 Amercing Dynamic Time Warping (ADTW)

The Amercing Dynamic Time Warping (WDTW) is a variant of DTW [10]. It is also designed to constrain the amount of warping, as in cDTW and WDTW. While cDTW imposes a hard window and WDTW uses multiplicative weights (i.e, MLWF), ADTW introduces an additive penalty for non-diagonal alignment. The word “Amercing” means “fining”. The non-diagonal alignments are required to pay the fines. Unlike WDTW, which uses a multiplicative weight based on the position of the alignment, ADTW applies an additive penalty  $\omega$  based on the action of warping. The non-diagonal alignments are penalized. Formally, the recursive relation for ADTW is defined as:

$$D(i, j) = d(q_i, c_j) + \min \begin{cases} D(i - 1, j - 1), \\ D(i - 1, j) + \omega, \\ D(i, j - 1) + \omega \end{cases} \quad (2.4)$$

ADTW penalizes the last two alignment actions.  $\omega$  is a user-given hyperparameter. It should be a non-negative scalar constant. In practice, it is defined through cross-validation, which determines the optimal  $\omega$  by training on a subset of data or heuristic search, which searches values in a user-given range.

To note, ADTW generalizes ED and DTW. If  $\omega = 0$ , no need to pay the fine for the non-diagonal alignment, which reduces to DTW. If  $\omega \rightarrow \infty$ , the non-diagonal alignment becomes prohibitive, and it reduces to ED.

## 2.2 Classification

In Chapter 3, we use ROCKET (RandOm Convolutional KErnel Transform) and its variants, including MiniRocket, MultiRocket, and Hydra, as the time series classifiers on the time series resulting from our encoding methods. Technically, they are not classifiers in their own right but rather feature extractors. These features are also called summary statistics. They are high-dimensional feature vectors that capture the characteristics of the original time series. The summary statistics are then fed to the classifiers to output the final classification results.

### 2.2.1 Ridge Classifier

The classifier that is usually chosen to work with ROCKET and its variants is a ridge classifier. The main advantage of it is speed. ROCKET and its variants generate a large number of features.

A ridge classifier is a wrapper that uses a ridge regression model as a routine to perform classification. It first maps the categorical labels of targets into continuous numbers, does the regression, and finally thresholds the numerical results from the regressor to obtain the classification result.

Given a training dataset  $D = \{(x_i, y_i)\}_{i=1}^n$  with  $n$  instances, where  $x_i \in \mathbb{R}^P$  is the feature vector with  $P$  dimensions and  $y_i \in \{+1, -1\}$  is its label, it minimizes the following optimization function.

$$\min_w \left( \sum_{i=1}^n (x_i^T w - y_i)^2 + \lambda \|w\|_2^2 \right) \quad (2.5)$$

Where  $\|w\|_2^2 = \sum_{j=1}^p w_j^2$  is the  $L_2$  norm of the weight vector and  $\lambda > 0$  controls the penalty. We explain the equation in brief. There are two terms inside the bracket. The first term is simply the sum of the residual, same as the one in the least squares method. The second term is called the  $L_2$  penalty and is used to introduce bias in the fit to avoid overfitting. Hence,  $\lambda$  serves as a regularization hyperparameter between the trade-off between bias and variance.

Since the above optimization function in a ridge classifier has a closed-form solution, it can be solved using linear algebra rather than iterative optimization, as in logistic regression. Besides, the generated features by the random kernels in ROCKET and its variants are highly correlated. Ridge regularization, also known as the  $L_2$  norm, can handle this case. Ridge regression shrinks regression

coefficients toward zero by adding an L2 penalty. It reduces model complexity and helps with multicollinearity.



# Chapter 3

## MTSCCleav: a Multivariate Time Series Classification (MTSC)-based Method for Predicting Human Dicer Cleavage Sites

MicroRNAs (miRNAs) are small non-coding RNAs (ncRNAs) that regulate gene expression at the post-transcriptional level, thereby playing essential roles in diverse biological processes. The biogenesis of miRNAs requires dicer to cleave at specific sites on the precursor miRNAs (pre-miRNAs). Several machine learning approaches have been proposed to predict whether an input sequence contains a cleavage site. However, they rely heavily on complex feature engineering or opaque deep neural networks. It results in a lack of generalizability and a long running time. There is a need for an alternative modeling paradigm that is accurate, fast, and simple.

We proposed a novel approach to frame the task as a multivariate time series classification problem. Nine encoding methods have been proposed to convert the sequence and the predicted secondary structure into a time series. We also leveraged the probabilities of the base pairs in the predicted secondary structure. Computational experiments demonstrate that our proposed method can achieve better or comparable results in terms of using a simpler, more intuitive model and less computational time. It achieves 3.7X to 28.8X speedup. Through perturbation

experiments, we found that regions close to the center of pre-miRNAs are essential for predicting human dicer cleavage sites.

By transforming the RNA sequence and its secondary structure information into a time series and utilizing simple, state-of-the-art time series classifiers, we achieved comparable or even superior performance in a simpler and faster manner.

Code is available at: <https://github.com/colemanyu/time-series-classification-cleavage>.

### 3.1 Background

One of the most important theories in molecular biology is the central dogma. It depicts the flow of genetic information [11, 12]. Proteins are the functional units. The information stored in DNA is used to create them. Genes (segments) in DNA are used as templates for messenger RNAs (mRNAs) synthesis. An mRNA acts as a set of instructions to assemble a chain of amino acids, which form a linear polypeptide. To become biologically active, this chain is folded into a specific 3D structure, a proper configuration that enables it to perform its desired functions. This folded polypeptide is called a functional protein, or simply a protein. This entire process closely resembles how a computer program runs on a machine. The source code does not function by itself. First, it is translated into an assembly code (a lower-level, less human-readable form) and then into an executable file that can actually perform the intended tasks [13].

These mRNAs are called “coding RNAs” because they code for proteins. There are other genes in which the final product is the RNA molecule itself. They are called non-coding RNAs (ncRNAs). Two types of small ncRNAs are particularly important. They are microRNAs (miRNAs) and small interfering RNAs (siRNAs). Their discovery was recognized with the 2006 Nobel Prize in Physiology or Medicine<sup>1</sup>, awarded for work completed only eight years prior [11].

In this study, we focus on miRNAs. An miRNA can regulate the expression of several proteins. Hence, understanding the biogenesis of miRNAs is of great value. It involves the processing of primary miRNAs (pri-miRNAs). RNAs are 3D molecules. However, it is hard to measure the 3D structure (tertiary structure) from the experiment and predict it from 1D sequence. We can understand their properties by analyzing their 1D sequence or 2D structure, known as secondary structure. RNA sequence is easily obtained through sequencing. The sequence

---

<sup>1</sup>The Nobel Prize in Physiology or Medicine 2006 - NobelPrize.org:  
<https://www.nobelprize.org/prizes/medicine/2006/summary/> (Accessed on: 2025-06-13).

and its predicted secondary structure of a pri-miRNA “hsa-let-7a-1” is shown in Figure 3.1.

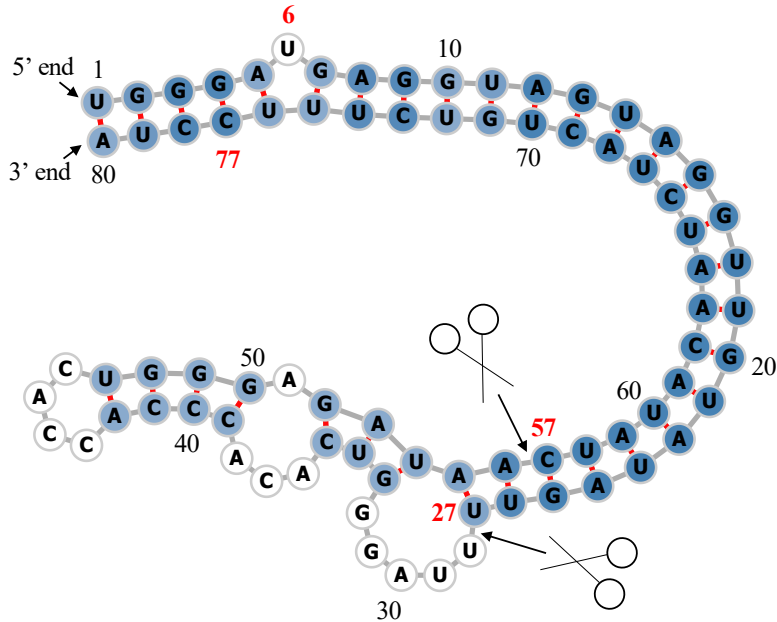


Figure 3.1: Predicted secondary structure of the sequence  $S$  of pri-miRNA “hsa-let-7a-1”<sup>2</sup>. Experimental evidence suggests that the two deviated mature miRNAs are  $UGA \cdots GUU$  and  $CUA \cdots UUC$ . They are  $S(6 : 27)$  and  $S(57 : 77)$  (Both ends are inclusive.). The ends are highlighted in **bold**. Since  $S(6 : 27)$  ( $S(57 : 77)$ ) is near the 5' (3') end, we call it “5p (3p) mature miRNA”. The two scissors indicate the two cleavage sites. The color intensity of the nodes reflects their base-pair probability in this predicted secondary structure. The deeper the color, the higher the probability. The unpaired nodes are uncolored. The raw figure is generated by RNAfold web server<sup>3</sup>.

Recall that a pri-miRNA contains a hairpin loop, also called a stem loop. A microprocessor complex comprising Drosa and DCGR8 cleaves the pri-miRNA to form a precursor miRNA (pre-miRNA) inside the nucleus. The stem-loop is still preserved, but the two arms become shorter. After that, the pri-miRNA is transported by Exportin 5 from the nucleus to the cytoplasm. It is further cleaved by an enzyme called dicer [14]. Dicer cleaves the stem-loop from the two arms at the two cleavage sites, shown as the two scissors in Figure 3.1. The stem-loop is removed. It results in a short double-stranded miRNA molecule, known

---

<sup>2</sup>Its miRBase entry: <https://mirbase.org/hairpin/MI0000060>. (Accessed on: 2025-06-12).

<sup>3</sup>RNAfold web server: <http://rna.tbi.univie.ac.at/cgi-bin/RNAWebSuite/RFold.cgi>. (Accessed on: 2025-06-12). The figure is viewed in “forna”. This view option can be chosen on the website.

as an miRNA duplex, which consists of the 5p strand and the 3p strand<sup>4</sup>. These molecules may be subjected to additional trimming. The miRNA duplex is loaded into an RNA-induced silencing complex (RISC). RISC unwinds the duplex and tends to retain the strand with the less stable 5' end as the guide strand. The other strand is called the passenger strand. The retained strand guides the RISC to silence the target mRNA. Note that both strands can become the guide strand.

Dicer plays an important role in the biogenesis of miRNAs. It is reasonable to argue that the structure of the pre-miRNAs informs dicer about the cleavage process. It would be of great benefit to understand how dicer selects cleavage sites from the neighborhood information near the cleavage sites. Studies [15, 16, 17] revealed that the secondary structures are essential for cleavage site determination. Hence, to predict or classify whether a subsequence, extracted from the sequence of a pri-miRNA, contains a cleavage site, we can make use of both the sequence and secondary structure information. PHDcleav employed support vector machines (SVM), leveraging sequence and structure-based features for the classification [18]. LBSSizeCleav improved upon it by considering the loop and bulge lengths [19]. [20] proposed an ensemble learning approach, using a gradient boosting machine for better accuracy. [21] developed a deep learning model, namely DiCleave. This model used an autoencoder to learn the secondary structure embeddings of pre-miRNAs from all the species in the miRBase database and leveraged this information. All these methods begin with curated pre-miRNA sequences from the miRBase database. Their secondary structures are predicted. Patterns are extracted from the sequence and the secondary structure. They create the positive cleavage patterns by setting the cleavage sites at the middle of the patterns. The follow-up work of [21], which created the cleavage pattern by allowing cleavage sites to appear at any position within the pattern, instead of the middle only [22]. It created a much larger dataset. This increased dataset facilitates the learning of the deep learning method at the cost of increased running time. We utilized the original dataset setting [18, 19, 20, 21]. DiCleave is the current state-of-the-art (SOTA) for this problem with the original dataset setting.

These models suffer several limitations. They rely heavily on complicated feature engineering or opaque deep learning models [20, 21, 22]. It results in a lack of generalizability and a long running time. There is a need to design a simpler model so that it can be easily extended to other prediction tasks on RNA data. One way to analyze sequence data is to transform it into time series data.

---

<sup>4</sup>The 5p strand comes from the 5' arm while the 3p strand comes from the 3' arm. For the directionality, the 5p (3p) strand retains the original 5' (3') end of the pre-miRNA.

In response to this, we proposed a multivariate time series classification-based method. Our contributions are shown as follows.

1. To the best of our knowledge, we are the first to frame the prediction of the cleavage sites as a multivariate time series classification problem.
2. We introduced several encoding methods to convert RNA data to time series.
3. We proposed utilizing the base-pair probabilities in the predicted secondary structure for the prediction. To our surprise, this information has been ignored in the existing studies.
4. For computational efficiency, our method achieves a 3.7X to 28.8X speedup compared to the state-of-the-art (SOTA).
5. We conducted perturbation-based experiments. It shows that regions close to the cleavage sites are important for this problem. It is consistent with the existing study [20].

## 3.2 Methods

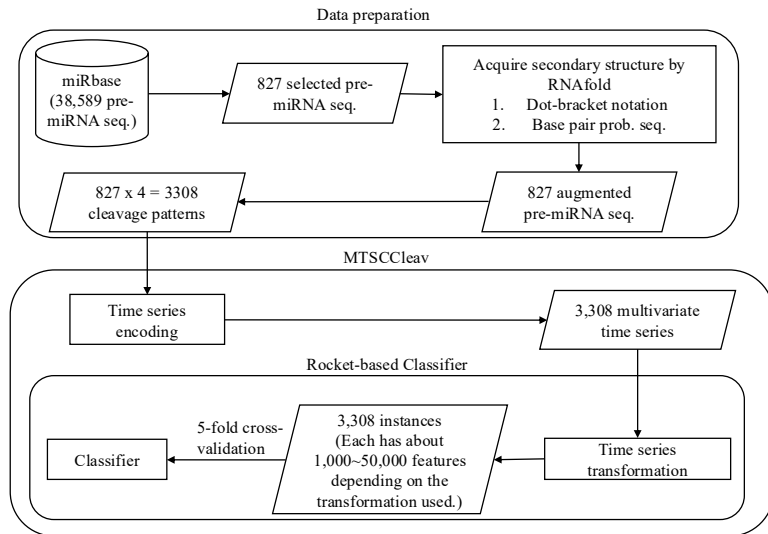


Figure 3.2: The overall pipeline of this study. Symbol notations: Cylinder - Dataset, Rectangle - Process, Parallelogram - Input / Output, Rounded Rectangle - Component.

The overall pipeline of this study is summarized in Figure 3.2.

### 3.2.1 Data Preparation

| Accession        | Name           | Organism               | Sequence                    | Mature miRNA 1                          | Mature miRNA 2                                 |
|------------------|----------------|------------------------|-----------------------------|---|--|
| MI0000001        | cel-let-7      | Caenorhabditis elegans | <i>UACAC</i> … <i>UUCGA</i> | cel-let-7-5p<br>17:38<br>experimental   | cel-let-7-3p<br>60:81<br>experimental          |
| <b>MI0000060</b> | hsa-let-7a-1   | Homo sapiens           | <i>UGGGA</i> … <i>UCCUA</i> | hsa-let-7a-5p<br>6:27<br>experimental   | hsa-let-7a-3p<br>57:77<br>experimental         |
| MI0000114        | hsa-mir-107    | Homo sapiens           | <i>CUCUC</i> … <i>ACAGA</i> | hsa-miR-107<br>50:72<br>experimental    | NA   |
| MI0000238        | hsa-mir-196a-1 | Homo sapiens           | <i>GUGAA</i> … <i>UUCAC</i> | hsa-miR-196a-5p<br>7:28<br>experimental | hsa-miR-196a-1-3p<br>45:65<br>not experimental |

Table 3.1: Selected representative records from miRBase. For the last two columns, the first line shows the name, the second line shows its location in the original sequence, and the third line indicates whether its existence has experimental evidence. The selected one is highlighted in **bold**.

We used miRBase database [23]<sup>5</sup>. The database comprises miRNA data from various organisms [24]. The database contains 38,589 miRNA records. Each record refers to an miRNA sequence, along with other properties such as name, accession, organism, and information on its derivative miRNA products. We are interested in pri-miRNA in humans. The derivative miRNA products are the mature miRNAs. The database also annotates the location of the mature miRNA within the original sequence and indicates whether its existence has experimental evidence.

Table 3.1 shows its four representative records. We first selected the records from humans (*Homo sapiens*). It resulted in 1,917 records. To identify the actual locations of the two cleavage sites in the pri-miRNA sequence supported by experimental evidence, we selected records that have two mature miRNAs resulting from cleavage at the 5p arm and the 3p arm, both of which have experimental support. Hence, only “MI0000060” (“hsa-let-7a-1”) would be selected in the table. It would serve as our running example. Its whole sequence is listed in Table 3.2. After the selection process, we selected 827 experimental validated pre-miRNA sequences, each with its two mature miRNA products. This formed our dataset.

### Augment the Dataset with Secondary Structure Information

We leveraged the predicted secondary structure of these sequences to enhance the accuracy of the classification. Recall that a specific three-dimensional (3D) structure is required for DNA, RNA, and protein to perform functions [25]. However,

---

<sup>5</sup>The website is [www.mirbase.org](http://www.mirbase.org), and the newest version of the database is Release 22.1 (Accessed on 2025-06-22).

| Sequence   | Secondary Structure<br>(In Dot-bracket notation)   |
|--|--|
| 1 UGGGA <b>UGAGGUAGUAGGUUGUAUAGUU</b> 27<br>28 UUAGGGUCACACCCACCACUGGGAGAU 54<br>55 AA <b>CUAUACAAUCUACUGUCUUCCUA</b> 80 | 1 ((((((.(((((((((((( 27<br>28 UUAGGGUCACACCCACCACUGGGAGAU 54<br>55 ))))))))))))))))))))) 80 |
| Base-pair probabilities sequence (the first 10 bases)  |  |
| 1 (0.549, 0.946, 0.987, 0.987, 0.904) 5<br>6 ( <b>0.000</b> , 0.841, 0.974, 0.981, 0.890) 10                             |  |

Table 3.2: The whole sequence of “hsa-let-7a-1” and its predicted secondary structure by RNAfold. The corresponding positions of the two mature miRNAs and the probability of the unpaired “U” are highlighted in **bold**.

finding these 3D structures using experimental methods such as X-ray crystallography or nuclear magnetic resonance (NMR) is costly and time-consuming. Hence, prediction methods for such 3D structures are necessary and helpful for downstream analysis. However, predicting the 3D structures is challenging. One of the reasons is that there are some “nonconventional” base-pair interactions (e.g., noncanonical and rare A-G) that allow an RNA sequence to fold into a 3D structure, in addition to the (G, U) wobble pair, which is common and functionally important in RNA secondary structures. It makes the search space for prediction much larger than, in the 2D case, the secondary structure. The local structures of the 3D structures, the secondary structures, only focus on the conventional base-pair interactions [12]. Hence, predicting secondary structures is easier and faster. We employed RNAfold from the ViennaRNA Package<sup>6</sup> to predict the secondary structure for a given pri-miRNA  $S$  [26]. RNAfold returns the secondary structure in the dot-bracket notation and a matrix of base-pair probabilities. The matrix is a square matrix with the side length  $|S|$ , where each entry  $m_{ij}$  is the probability of base  $s_i$  paired up with base  $s_j$ . Dot-bracket notation is a way of representing the secondary structure of  $S$ . Open parentheses “(“ (Close parentheses “)” ) indicates that the base is paired with a complementary base further (earlier) along in  $S$ . Dot “.” indicates that the base is unpaired. Equipped with the matrix, we can construct the base-pair probability sequence of  $S$ . The predicted secondary structure and the base-pair probability sequence of our running example are shown in Table 3.2.

### Extract Cleavage Patterns

The locations of the two mature miRNAs on the whole sequence indicate the probable locations of the two cleavage sites. The 5p cleavage site must be beyond

---

<sup>6</sup>The latest stable release is Version 2.7.0 (Accessed on 2025-06-22).

and near the ending location of the 5p mature miRNA. We deemed the immediate bond next to the 5p mature miRNA’s ending position the 5p cleavage site, with the knowledge that the actual cleavage site may not be this immediate bond but rather the nearby bonds after it. The same applies to the 3p cleavage site. It is located at the immediate bond before the starting position of the 3p mature miRNA.

For each arm of each whole sequence, we extracted a 14-string<sup>7</sup> with the cleavage site located at the center of the string. The first 7 nt (nucleotide) before the center are highlighted in **bold**. In our running example, it would be “**UAUAGUUUUAGGU**” for the 5p cleavage site and “**GAGAUAA**CUAUACA” for the 3p cleavage site. We refer to these 14-strings as cleavage patterns. We also generate non-cleavage patterns by selecting a 14-string with the center 6 nt away from the corresponding cleavage sites towards the corresponding mature miRNA [19, 20] for each arm of each whole sequence. So, in our running example, the 5p non-cleavage pattern would be “**AGGUUGU**AUAGUUU”. The 3p non-cleavage pattern would be “**ACUAUAC**AAUCUAC”.

In conclusion, for a given pri-miRNA sequence, we can generate two cleavage patterns and two non-cleavage patterns. We call these four patterns simply the “four strings” of a given pri-miRNA. We also call each string a strand. The “four strings” of our running example are listed in Table 3.3.

|                      | 5p cleav             | 5p non-cleav           | 3p cleav               | 3p non-cleav           |
|----------------------|----------------------|------------------------|------------------------|------------------------|
| Input strand         | <b>UAUAGUU</b> UAGGU | <b>AGGUUGU</b> AUAGUUU | <b>GAGAUAA</b> CUAUACA | <b>ACUAUAC</b> AAUCUAC |
| Complementary strand | AUAUCAA_____UA       | UCUAACAUAAUCAA_        | C_CUGUUGAUUAUGU        | UGAUUAUGUUGGAUG        |

Table 3.3: The first row shows the “four strings” of “hsa-let-7a-1”. Their complementary strands are shown in the second row. As a whole, they are referred to as the “eight strings”.

We can construct the complementary strand of each of the strands in the “four strings” by finding the corresponding paired base for each of the bases in the input strand by considering the secondary structure information. We use “\_” to denote the unpaired base in the complementary strand. For example, in Figure 3.1, “UUAGG” in the 5p cleavage pattern is unpaired, while other bases pair with some bases, the resulting complementary strand is “AUAUCAA\_\_\_\_\_UA”. There is a loop/budge there. We refer to the “four strings” and the four complementary strands together as the “eight strings” of the input pre-miRNA. It is also shown in Table 3.3.

---

<sup>7</sup>String with length = 14.

### 3.2.2 Time Series Encoding

A *time series*  $T = t_1, t_2, \dots, t_n$  is a sequence of real-valued numbers<sup>8</sup>. A short contiguous region of  $T$  is called a subsequence. A *subsequence*  $T(i : j) = t_i, t_{i+1}, \dots, t_j$  of a time series  $T$  is a shorter time series that starts from position  $i$  and ends at position  $j$ , where  $i < j$ .

Strings and time series are temporal sequences. The difference between strings and time series lies in their behavioral attributes [27]. For strings, an entry is a letter from a predefined set called the *alphabet*. For example, the alphabet is  $\{A, C, G, T\}$  in the DNA string, while  $\{A, C, G, U\}$  in the RNA string. For time series, an entry is a real number. Unlike real numbers, there is no ordering in the alphabet unless some external domain knowledge is introduced.

The study of applying signal processing techniques to genomic data is called “Genomic Signal Processing” (GSP) [28, 29]. In the field of GSP, the time series representations of DNA strings are referred to as DNA numeric representations (DNR). Many DNRs have been proposed. We noted that DNA strings and RNA strings are equivalent from a computational standpoint. Many transformation methods designed for DNA can be applied to RNA by simply substituting  $T$  with  $U$ . We present nine encoding methods. The relationship among them is shown in Figure 3.3.

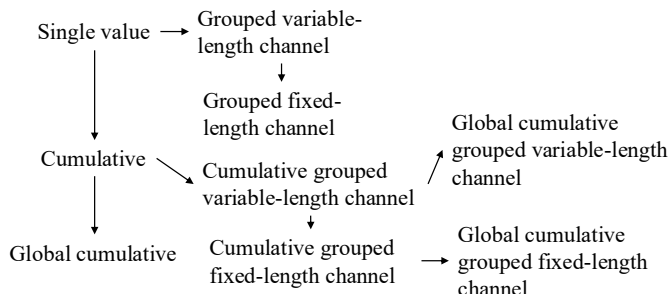


Figure 3.3: Relationship of the proposed encoding methods.

#### Single Value versus Cumulative

One of the simple, if not the simplest, encoding is to map the letters into numbers. Domain knowledge can be utilized. This approach is called the “Single value mapping” [30, 31, 32, 33, 28]. One single value is assigned to each of the letters. [34] employed the atomic number of each nucleotide as the transformed values,

---

<sup>8</sup>Unless otherwise specified, we denote entries of a time series (e.g.,  $T$ ) using the corresponding lowercase letter (e.g.,  $t$ ).

where  $\{G = 78, A = 70, C = 58, T = 66\}$ . [35] used electron-ion interaction potential representation (EIIP) as such value, where  $\{G = 0.0806, A = 0.1260, C = 0.1340, T = 0.1335\}$ . Our goal is to transform the input strand and its complementary strand into time series, aiming to capture the information contained in these sequences and the secondary structure implied by them. We employed the following reasoning to assign the value:

1. We employ the complementary property [36, 32] during encoding. Recall that in the base-pairing rules,  $G$  pairs with  $C$  to form three hydrogen bonds while  $A$  pairs with  $U^9$  to form two hydrogen bonds.  $G-C$  pairs are more stable than  $A-U$  pairs.  $G$  ( $U$ ) can be regarded as the “inverse” of  $C$  ( $A$ ). We can preserve these base-pairing rules in the encoding by assigning  $G$  ( $A$ ) and  $C$  ( $U$ ) opposite values.
2.  $G$  and  $A$  have a two-ring structure. They are purines.  $C$  and  $U$  have a single-ring structure. They are pyrimidines. Hence, we put  $G$  and  $A$  ( $C$  and  $U$ ) on the same side of the number line with zero in the middle.
3. The lower stability of  $A-U$  pairs promotes strand separation, thereby facilitating the unwinding of the miRNA duplex during RISC loading. Regions rich in  $A$  and  $U$  are thus more likely to undergo strand selection and cleavage events. We assigned  $A$  ( $U$ ) with a larger absolute value than  $G$  ( $C$ ) to reflect this functional relevance. It aims to highlight sequence regions with higher cleavage potential.

It results in our baseline transformation method, namely “Single value mapping” as shown in row 1 of Table 3.4.  $S$  is the input strand. When we encode  $S$  without incorporating the corresponding base-pair probability sequence  $P$ , we set  $p_i = 1$  for all the entries of  $P$ . We use the first ten nucleotides of the complementary strand of the 3p cleav of “hsa-let-7a-1”, as shown in Table 3.3 as  $S$  in the examples in Table 3.4.

With the assigned value to each nucleotide defined in single-value mapping, we can compute a cumulative sum of those values over time. It captures the aggregated signal by accumulating past events, allowing us to focus on the trend [37, 38]. We named this method as “Cumulative mapping”, shown in row 4 of Table 3.4.

---

<sup>9</sup>In DNA,  $A$  pairs with  $T$ .

|   | Encoding   | Algorithm   | Example   |
|---|--|---|---|
| 1 | Single value mapping<br>[30, 31, 32, 33, 28]       | <p>for <math>i = 1</math> to <math> S </math>:</p> $t_i = \begin{cases} 2 \cdot p_i & \text{if } s_i = A \\ 1 \cdot p_i & \text{if } s_i = G \\ -1 \cdot p_i & \text{if } s_i = C \\ -2 \cdot p_i & \text{if } s_i = U \\ 0 & \text{otherwise} \end{cases}$ <p>return <math>T</math></p>  | <p><math>S = C, -, C, U, G, U, U, G, A, U</math><br/> <math>P = 0.843, 0.000, 0.807, 0.807, 0.793,</math><br/> <math>0.914, 0.982, 1.000, 0.999, 0.999</math></p> <p>Without base-pair probability sequence:<br/> <math>T = -1, 0, -1, -2, 1, -2, -2, 1, 2, -2</math></p> <p>With base-pair probability sequence:<br/> <math>T = -0.843, 0.000, -0.807, -1.614,</math><br/> <math>0.793, -1.829, -1.963,</math><br/> <math>1.000, 1.999, -1.998</math></p>  |
| 2 | Grouped variable-length channel mapping            | <p><math>j = 1, k = 1</math></p> <p>for <math>i = 1</math> to <math> S </math>:</p> $t_j^1 = \begin{cases} 1 \cdot p_i & \text{if } s_i = A \\ -1 \cdot p_i & \text{if } s_i = U \\ 0 & \text{otherwise} \end{cases}$ $t_k^2 = \begin{cases} 1 \cdot p_i & \text{if } s_i = G \\ -1 \cdot p_i & \text{if } s_i = C \\ \text{if } (s_i = G) \text{ or } (s_i = C): \\ \quad \text{increment } k \text{ by 1} \\ \text{else:} \\ \quad \text{increment } j \text{ by 1} \end{cases}$ <p>return <math>T^1, T^2</math></p>  | <p>Without base-pair probability sequence:<br/> <math>T^1 = 0, -1, -1, -1, 1, -1</math><br/> <math>T^2 = -1, -1, 1, 1</math></p> <p>With base-pair probability sequence:<br/> <math>T^1 = 0.000, -0.807, -0.914, -0.982, 0.999, -0.999</math><br/> <math>T^2 = -0.843, -0.807, 0.793, 1.000</math></p>  |
| 3 | Grouped fixed-length channel mapping               | <p>for <math>i = 1</math> to <math> S </math>:</p> $t_i^1 = \begin{cases} 1 \cdot p_i & \text{if } s_i = A \\ -1 \cdot p_i & \text{if } s_i = U \\ 0 & \text{otherwise} \end{cases}$ $t_i^2 = \begin{cases} 1 \cdot p_i & \text{if } s_i = G \\ -1 \cdot p_i & \text{if } s_i = C \\ 0 & \text{otherwise} \end{cases}$ <p>return <math>T^1, T^2</math></p>  | <p>Without base-pair probability sequence:<br/> <math>T^1 = 0, 0, 0, -1, 0, -1, -1, 0, 1, -1</math><br/> <math>T^2 = -1, 0, -1, 0, 1, 0, 0, 1, 0, 0</math></p> <p>With base-pair probability sequence:<br/> <math>T^1 = 0.000, 0.000, 0.000, -0.807,</math><br/> <math>0.000, -0.914, -0.982,</math><br/> <math>0.000, 0.999, -0.9999</math><br/> <math>T^2 = -0.843, 0.000, -0.807, 0.000,</math><br/> <math>0.793, 0.000, 0.000,</math><br/> <math>1.000, 0.000, 0.000</math></p>                             |
| 4 | Cumulative mapping<br>[37, 38]                     | <p><math>t_1 = 0</math></p> <p>for <math>i = 1</math> to <math> S </math>:</p> $t_{i+1} = \begin{cases} t_i + 2 \cdot p_i & \text{if } s_i = A \\ t_i + 1 \cdot p_i & \text{if } s_i = G \\ t_i - 1 \cdot p_i & \text{if } s_i = C \\ t_i - 2 \cdot p_i & \text{if } s_i = U \\ t_i & \text{otherwise} \end{cases}$ <p>return <math>T //  T  =  S  + 1</math></p>   | <p>Without base-pair probability sequence:<br/> <math>T = 0, -1, -1, -2, -4, -3, -5, -7, -6, -4, -6</math></p> <p>With base-pair probability sequence:<br/> <math>T = 0.000, -0.843, -0.843, -1.650,</math><br/> <math>-3.265, -2.471, -4.300, -6.263,</math><br/> <math>-5.264, -3.265, -5.263</math></p>  |
| 5 | Cumulative grouped variable-length channel mapping | <p><math>t_1^1 = 0, t_1^2 = 0</math></p> <p><math>j = 1, k = 1</math></p> <p>for <math>i = 1</math> to <math> S </math>:</p> $t_{j+1}^1 = \begin{cases} t_j^1 + 1 \cdot p_i & \text{if } s_i = A \\ t_j^1 - 1 \cdot p_i & \text{if } s_i = U \\ t_j^1 & \text{if } s_i = - \end{cases}$ $t_{k+1}^2 = \begin{cases} t_k^2 + 1 \cdot p_i & \text{if } s_i = G \\ t_k^2 - 1 \cdot p_i & \text{if } s_i = C \\ t_k^2 & \text{if } (s_i = G) \text{ or } (s_i = C): \\ \quad \text{increment } k \text{ by 1} \\ \text{else:} \\ \quad \text{increment } j \text{ by 1} \end{cases}$ <p>return <math>T^1, T^2</math></p> | <p>Without base-pair probability sequence:<br/> <math>T^1 = 0, -1, -2, -3, -2, -3</math><br/> <math>T^2 = 0, -1, -2, -1, 0</math></p> <p>With base-pair probability sequence:<br/> <math>T^1 = 0.000, -0.807, -1.722,</math><br/> <math>-2.703, -1.704, -2.703</math><br/> <math>T^2 = 0.000, -0.843, -1.650,</math><br/> <math>-0.857, 0.143</math></p>  |
| 6 | Cumulative grouped fixed-length channel mapping    | <p><math>t_1^1 = 0, t_1^2 = 0</math></p> <p>for <math>i = 1</math> to <math> S </math>:</p> $t_{i+1}^1 = \begin{cases} t_i^1 + 1 \cdot p_i & \text{if } s_i = A \\ t_i^1 - 1 \cdot p_i & \text{if } s_i = U \\ t_i^1 & \text{otherwise} \end{cases}$ $t_{i+1}^2 = \begin{cases} t_i^2 + 1 \cdot p_i & \text{if } s_i = G \\ t_i^2 - 1 \cdot p_i & \text{if } s_i = C \\ t_i^2 & \text{otherwise} \end{cases}$ <p>return <math>T^1, T^2 //  T^1  =  T^2  =  S  + 1</math></p>  | <p>Without base-pair probability sequence:<br/> <math>T^1 = 0, 0, 0, -1, -1, -2, -3, -3, -2, -3</math><br/> <math>T^2 = 0, -1, -1, -2, -2, -1, -1, 0, 0, 0</math></p> <p>With base-pair probability sequence:<br/> <math>T^1 = 0.000, 0.000, 0.000, 0.000,</math><br/> <math>-0.807, -0.807, -1.722, -2.703,</math><br/> <math>-2.703, -1.704, -2.703</math><br/> <math>T^2 = 0.000, -0.843, -0.843, -1.650,</math><br/> <math>-1.650, -0.857, -0.857, -0.857,</math><br/> <math>0.143, 0.143, 0.143</math></p> |

Table 3.4: Time series encoding.  $P$  is the corresponding base-pair probability sequence of  $S$ .  $p_i = 1$  if we encode  $S$  without incorporating base-pair probability sequence.

## Grouped Variable-Length Channel versus Grouped Local-Length Channel

We can transform the input strand into a multivariate time series with two channels using grouped binary encoding, where nucleotides are grouped into  $(A, U)$  and  $(G, C)$ . It releases our third assumption that  $A$  ( $U$ ) has a larger absolute value than  $G$  ( $C$ ). We proposed two variations. The first one allows the output to be variable-length sequences per channel, depending on group-specific occurrences. The second one always returns two resulting sequences of a fixed length. Two variations extended from single value mapping are shown in rows 2 and 3, while those extended from cumulative mapping are shown in rows 5 and 6 in Table 3.4.

## Global Cumulative versus Local Cumulative

In cumulative mapping and its variations, we can choose where to start the accumulation. For a given subsequence  $S'$  of the whole sequence  $S$ , accumulation can start from the beginning of  $S$  even if only  $S'$  is used downstream. It can also begin just at the start of the  $S'$ . The first one preserves the global context. It can be useful when previous nucleotides (those before  $S'$ ) influence later interpretation. The second one focuses solely on local history in  $S'$ , ignoring global history. It is helpful if the previous nucleotides do not affect the chemical property of  $S'$ .

Consider  $T = 0, -1, \dots, -6$  of the input string  $S$  in “Cumulative mapping” in Table 3.4, which accumulates from 0.  $S$  is the suffix with length = 10 of the constructed complementary strand of  $S(1 : 63)$  in Figure 3.1. If we start the accumulation from the first entry of the constructed complementary strand instead, it will yield a different result. Suppose that the last entry of the time series encoded in the cumulative mapping of the constructed complementary strand is -8, the time series encoded in the “Global cumulative mapping” for  $S$  would accumulate from -8 instead of 0. The result is  $T = -8, -9, \dots, -14$ . Note that it has the same trend as the original  $T$ . This “Global cumulative” concept can be applied to every cumulative-based method, as shown in Figure 3.3.

## Incorporating Base-Pair Probabilities

We can incorporate the base-pair probabilities  $P$  in the encoding by thinking of it as the weight or confidence  $p_i$  in the value assignment of each nucleotide  $s_i$ . It is implemented by multiplying the base-pair probability  $p_i$  of the nucleotide  $s_i$  with the assigned value of the kind of nucleotide of  $s_i$  during encoding, as shown in Table 3.4.

## Transforming the Secondary Structure into a Time Series

We can transform the secondary structure in the dot-bracket notation into a time series by “Single value mapping”, where “(” maps to 1, “.” maps to 0, and “)” maps to -1.

### 3.2.3 Time Series Classification

In univariate time series classification, an instance in the dataset consists of a time series  $x = x_1, x_2, \dots, x_m$  with  $m$  observations and a discrete class label  $y$ , which takes  $c$  possible values [39, 40]. If  $c = 2$ , we refer to binary classification. If  $c > 2$ , we refer to multi-class classification. In multivariate time series classification, the time series is not a single sequence but a list of sequences. Each sequence is called a channel. There are many classifiers defined for time series data, including distance-based, feature-based, interval-based, shapelet-based, dictionary-based, convolution-based, and deep learning-based classifiers. Additionally, two or more of the above approaches can be combined, resulting in hybrid approaches [1, 40, 39]. We employed convolution-based classifiers due to their simplicity and accuracy.

#### Convolution-Based Classifiers

Convolution-based classifiers first use randomly parameterized kernels to perform convolutions on the original time series  $T$ . A kernel is referred to as parameterized because its behavior is governed by a set of parameters, which will be discussed in detail later. Convolution is an operation to transform  $T$  to another time series  $M$ , where  $M$  is called the activation map. Its entry  $M_i$  is calculated by applying a kernel  $\omega$  with length  $l$  to  $T$  at position  $i$ , defined as follows:

$$M_i = T(i : i + l - 1) * \omega = \sum_{j=0}^{l-1} t_{i+j} \cdot \omega_{1+j}$$

To note,  $|T(i : i + l - 1)| = |\omega| = l$ . Entries  $M_i$ 's are calculated by sliding  $\omega$  across  $T$  and computing a dot product. Additionally, although the original paper [41] used the term “convolution” to refer to the above operation, “cross-correlation” may be a more suitable term for this operation. Recall  $T$  with length  $m$  has  $(m - l + 1)$  sliding windows of length  $l$ , given that the increment is  $1^{10}$ , which defines the length of  $M$ .

---

<sup>10</sup>One step to the right per time.

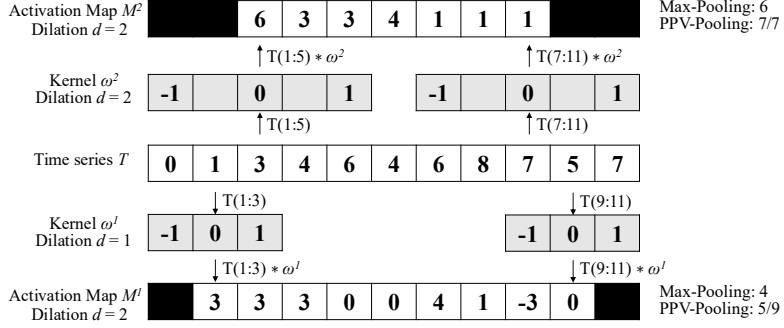


Figure 3.4: Features generation in the transformation

Figure 3.4 shows two kernels  $\omega^1$  and  $\omega^2$  with lengths 3 and 5, respectively. Each of which performs a convolution with  $T$  and returns two activation maps,  $M^1$  and  $M^2$ , respectively. For example,  $M_1^1 = T(1 : 3) * \omega^1 = 3$ . By sliding  $\omega^1$  one time stamp at a time, an activation map  $M^1$  with length  $= (m-l+1) = 11-3+1 = 9$  is obtained. Then, pooling operations, such as the maximum (MAX) and proportion of positive values (PPV), are applied on  $M^1$  to derive the summary features. In Figure 3.4, MAX and PPV are applied on  $M^1$  and  $M^2$ . The summary features of  $M^1$  are 4 and 5/9, which correspond to MAX and PPV, respectively. Dilation refers to a method that enables a kernel to cover a larger portion by creating empty spaces between entries in the kernel. The dilation  $d$  of  $\omega^2$  is 2. It introduces a gap of 1 in every two values of  $\omega^2$ .

The most popular convolution-based approach is the Random Convolutional Kernel Transform (ROCKET) [41]. It generates a large number of randomly parameterized kernels, ranging from thousands to tens of thousands. The kernel's parameters include length, weights (the entries inside the kernel), bias (the value added to the result of the convolution operation), and dilation. Additionally, padding can be applied to  $T$  at the start and end, ensuring  $M$  has the same length as the input. To note,  $T$ ,  $M_1$ , and  $M_2$  in Figure 3.4 have different lengths. The summary statistics of the activation map are obtained through two pooling operations: MAX and PPV. Hence, for  $k$  kernels, the transformed data has  $2k$  features. The default value of  $k$  is 10,000.

There are two extensions of ROCKET. They are MiniROCKET [42] and MultiROCKET [43]. MiniROCKET removes unnecessary operations and many of the random components in the definition of kernels used by ROCKET. It speeds up Rocket by over an order of magnitude with no significant difference in accuracy, making the classifier almost deterministic. For example, the kernel length is fixed, and only two weight values are used. Only PPV is used for the summary statis-

tics. MultiROCKET is extended from MiniROCKET. The main improvement of it is to extract features from first-order differences as defined in Table 3.5 and add three new pooling operations [43]. The three added operations are mean of positive values (MPV), mean of indices of positive values (MIPV) and longest stretch of positive values (LSPV).

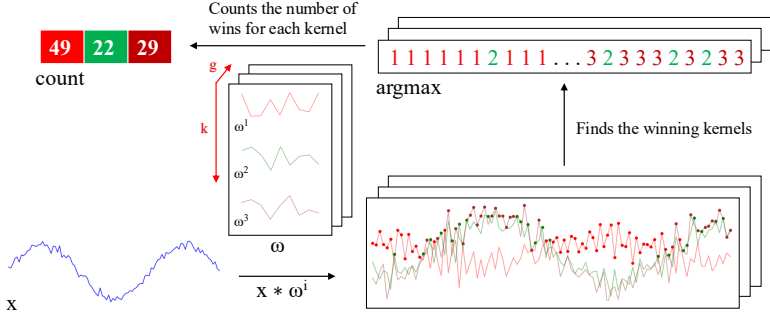


Figure 3.5: Convolutions of HYDRA for each input time series with a set of random kernels  $w$ , organized into  $g$  groups with  $k$  kernels each.

The HYbrid Dictionary-ROCKET Architecture (Hydra) combines dictionary-based and convolution-based models [44]. Similar to ROCKET-based classifiers, it uses random kernels to extract features from the input time series. But it groups the kernels into  $g$  groups of  $k$  kernels each, as shown in Figure 3.5. Each time series is passed through all the groups. For each group of kernels, we slide them across  $T$  and compute the dot product at each timestamp. Recall that the dot product of two input vectors ( $x$  and  $w_i$ ) has the maximum value when the two vectors align in the same direction and the minimum value when they are oriented in opposite directions. We record the kernel that best matches the subsequence of  $T$  at each timestamp in each group (i.e.,  $argmax$ ). We refer to these kernels as the winning kernels. This results in a  $k$ -dimensional count vector for each of the  $g$  groups, where  $k = 3$  in Figure 3.5. This results in a total of  $g \times k$  features, with default values of  $g = 64$  and  $k = 8$ . It uses a total of  $k \times g = 512$  kernels per dilation. In addition to recording the kernel with the maximum response, we can also record the kernel with the minimum response, knowing that this kernel will be the best match with the “inverted” subsequence of  $T$ . Hydra is applied to both the original time series and its first-order differences. Hydra generated approximately 1000 features for each instance in our dataset. [44] found that it can improve the accuracy by concatenating features generated from Hydra with those from MultiRocket. This classifier is called MultiROCKET-Hydra.

These five classifiers share the same simple design pattern. It involves the over-production of features followed by a selection strategy. A large number of features

(1,000 ~ 50,000) are generated for each instance. The features are then fed into a simple linear classifier. It determines which features are most useful and returns the final classification result. A ridge classifier is used in this study. It is a linear classifier that extends ridge regression to classification tasks by applying a threshold to the predicted values. It uses L2 regularization to prevent overfitting. The regularization strength is selected by internal cross-validation. A Ridge classifier is suggested for small datasets, as in our case, while a logistic regression classifier is suggested for large datasets [1].

While these five classifiers are often referred to as classifiers [1], they are technically time series transformation methods for generating features that are then fed to a downstream classifier. The comparison of them is shown in Table 3.5. For MiniROCKET and MultiROCKET, the bias is determined from the convolution output, and the dilation depends on the length of the input time series [42, 43]. The main differences among ROCKET-based classifiers lie in how the summary features are generated. The generation of the summary features depends on:

1. Kernels, which are defined based on the parameters, which consist of kernel length, kernel weights, bias, and dilation.
2. The way that padding applies to  $T$ , which leads to activation maps with different lengths.
3. The pooling operations, which are used in extracting features on the activation map.

|                                  | ROCKET              | MiniROCKET             | MultiROCKET            | Hydra                     |
|----------------------------------|---------------------|------------------------|------------------------|---------------------------|
| kernel length                    | {7, 9, 11}          | 9                      | 9                      | 9                         |
| kernel weights                   | $\mathcal{N}(0, 1)$ | {-1, 2}                | {-1, 2}                | $\mathcal{N}(0, 1)$       |
| bias                             | $\mathcal{U}(0, 1)$ | from output            | from output            | none                      |
| dilation                         | random              | fixed (input-relative) | fixed (input-relative) | random                    |
| padding                          | random              | fixed                  | fixed                  | always                    |
| pooling operations               | MAX, PPV            | PPV                    | PPV, MPV, MIPV, LSPV   | Response per Kernel/Group |
| 1 <sup>st</sup> order difference | no                  | no                     | yes                    | yes                       |
| feature vector size              | 20k                 | 10k                    | 50k                    | relative to input         |

Table 3.5: Comparison of rocket-based classifiers [1].  $\mathcal{N}(0, 1)$ : a standard normal distribution,  $\mathcal{U}(0, 1)$ : a uniform distribution between 0 and 1, 1<sup>st</sup> order difference:  $\Delta T = t_2 - t_1, t_3 - t_2, \dots, t_n - t_{n-1}$ .

### 3.2.4 Evaluation Metrics

To evaluate the performance of our time series-based classification (MTSC) model, we adopted five standard classification metrics. They are Accuracy (Acc), Speci-

ficity (Sp), Sensitivity (Sn), F1 score (F1), and Matthews Correlation Coefficient (MCC) [45].

$$\begin{aligned} Acc &= \frac{TP + TN}{TP + TN + FP + FN} \\ Sp &= \frac{TN}{TN + FP} \\ Sn &= \frac{TP}{TP + FN} \\ F1 &= \frac{2 \times TP}{2 \times TP + FP + FN} \\ MCC &= \frac{TP \times TN - FP \times FN}{\sqrt{(TP + FP)(TP + FN)(TN + FP)(TN + FN)}} \end{aligned}$$

where TP, TN, FP, and FN are the number of true positives, true negatives, false positives, and false negatives, respectively.

To extend a binary metric to multi-class problems, we can treat the data as a collection of binary problems, one for each class. One class is treated as positive while the other classes are treated as negative. Then, the multi-class metrics can be obtained by averaging binary metric calculations across the set of classes. There are different ways of doing the averaging. Here, we adopted a macro-averaging approach. It treats each class equally and calculates the mean of the binary metrics. To use *MCC* in the multiclass case, it can be defined in terms of a confusion matrix  $C$  for  $K$  classes, where  $C_{i,j}$  is the number of observations that are actually in class  $i$  and predicted to be in class  $j$  [46].

$$MCC_{multi} = \frac{c \times s - \sum_k^K p_k \times t_k}{\sqrt{(s^2 - \sum_k^K p_k^2) \times (s^2 - \sum_k^K t_k^2)}}$$

where  $t_k = \sum_i^K C_{i,k}$  (denoting the number of times class  $k$  actually occurred),  $p_k = \sum_i^K C_{k,i}$  (denoting the number of times class  $k$  was predicted),  $c = \sum_k^K C_{k,k}$  (denoting the total number of samples correctly predicted) and  $s = \sum_i^K \sum_j^K C_{i,j}$  (denoting the total number of samples).

### 3.3 Results

The code implementing our method is available at <https://github.com/colemanyu/time-series-classification-cleavage>. The dataset of this study is available at <https://www.mirbase.org>.

In all experiments, the models were trained and tested using 5-fold cross-validation. We retrieved 827 empirically validated sequences of pre-miRNAs. There are 5p arm and 3p arm in each sequence. For each arm, we defined a cleavage pattern and a non-cleavage pattern. Three datasets, namely “5p arm”, “3p arm”, and “multi-class” were constructed by these patterns. We refer to the cleavage patterns as positive instances and the non-cleavage patterns as negative instances. The 5p arm dataset comprises 827 positive instances and an equal number of negative instances. The 5p arm and 3p arm datasets are binary-class datasets. The multi-class dataset comprises all patterns from both the 5p arm and the 3p arm. There are 827 “5p” instances<sup>11</sup>, 827 “3p” instances, and 1,654 negative instances.

For every fold in 5-fold cross-validation, the dataset was divided into a training set and a test set with sizes of 80% and 20% of the whole dataset, respectively. We kept the class distribution approximately the same in each fold, since it is in the original dataset. In each fold derived from the 5p arm and 3p arm datasets, the training set has a size of 1,323, and the test set has a size of 331. In each fold derived from the multi-class dataset, the training set has a size of 2,262, and the test set has a size of 662. We reported the average of the five classification metrics.

The ROCKET-based classifiers require all channels in the multivariate time series to have equal length. We applied padding to the shorter channels using the constant value 100, which does not appear in the original time series. It ensures the padding does not introduce ambiguity or interfere with the semantic meaning of the encoded nucleotide signals.

### 3.3.1 Channel Ablation Study

We utilized three types of data as the input features for each instance. They are (1) the RNA sequence, which consists of the primary strand and its complementary strand, (2) the secondary structure information, and (3) the base-pair probability sequence. To input the data into our time series-based classifiers, we converted them into multivariate time series. The primary strand and its complementary strand are each encoded into one or two channels, using the encoding methods in Table 3.4. For example, single value mapping encodes a strand in one channel, while grouped variable-length channel mapping encodes in two channels. The secondary structure information is converted into a univariate time

---

<sup>11</sup>Cleavage patterns from the 5p arm.

series. The base-pair probability sequence is already in numerical form and does not require further transformation. It can be used either as a standalone channel or incorporated into the encoding of the complementary strand. We performed a channel ablation study to determine the most informative combination of the above channels.

We referred to the multivariate time series that consists of the channels from the RNA sequence only as the baseline setting. We added the other channels to this baseline. It leads to the following configurations (cfgs):

1. (cfg 1) Baseline: Time series derived only from the RNA sequence.
2. (cfg 2) Baseline + Secondary structure: Baseline + time series representation of the secondary structure.
3. (cfg 3) Baseline + Base-pair probability (Standalone): Baseline + the base-pair probability sequence as a standalone channel.
4. (cfg 4) Baseline + Base-Pair probability (Incorporated): Baseline with the base-pair probability sequence incorporated into the encoding of the complementary strand.

| Classifier  | 5p arm            |              |              |              |              | 3p arm       |              |              |              |              | multi-class  |              |              |              |              |              |
|---|-------------------|--------------|--------------|--------------|--------------|--------------|--------------|--------------|--------------|--------------|--------------|--------------|--------------|--------------|--------------|--------------|
|   | Acc               | Sp           | Sn           | F1           | MCC          | Acc          | Sp           | Sn           | F1           | MCC          | Acc          | Sp           | Sn           | F1           | MCC          |              |
| Baseline<br>(cfg 1)   | ROCKET            | 0.781        | 0.743        | 0.819        | 0.789        | 0.563        | 0.790        | 0.773        | 0.807        | 0.793        | 0.580        | 0.717        | 0.838        | 0.685        | 0.700        | 0.538        |
|   | MiniROCKET        | 0.755        | 0.728        | 0.782        | 0.762        | 0.512        | 0.788        | 0.781        | 0.794        | 0.789        | 0.576        | 0.685        | 0.823        | 0.653        | 0.662        | 0.486        |
|   | MultiROCKET       | 0.784        | 0.767        | 0.801        | 0.787        | 0.569        | 0.803        | 0.792        | 0.814        | 0.805        | 0.606        | 0.691        | 0.830        | 0.667        | 0.672        | 0.501        |
|   | Hydra             | 0.830        | 0.800        | 0.860        | 0.835        | 0.663        | 0.808        | 0.797        | 0.820        | 0.810        | 0.617        | 0.731        | 0.844        | 0.696        | 0.712        | 0.560        |
|   | MultiROCKET-Hydra | 0.796        | 0.778        | 0.815        | 0.800        | 0.594        | 0.807        | 0.767        | 0.816        | 0.808        | 0.614        | 0.701        | 0.836        | 0.681        | 0.686        | 0.520        |
| Baseline +<br>Secondary<br>Structure<br>(cfg 2)                     | ROCKET            | <b>0.847</b> | <b>0.832</b> | 0.862        | <b>0.849</b> | <b>0.695</b> | <b>0.855</b> | 0.842        | 0.868        | <b>0.857</b> | <b>0.711</b> | <b>0.836</b> | <b>0.907</b> | <b>0.828</b> | <b>0.833</b> | 0.736        |
|   | MiniROCKET        | 0.825        | 0.807        | 0.843        | 0.827        | 0.652        | 0.822        | 0.802        | 0.843        | 0.826        | 0.646        | 0.823        | 0.900        | 0.812        | 0.818        | 0.715        |
|   | MultiROCKET       | 0.812        | 0.803        | 0.822        | 0.814        | 0.626        | 0.824        | 0.809        | 0.839        | 0.826        | 0.649        | 0.796        | 0.888        | 0.791        | 0.792        | 0.673        |
|   | Hydra             | 0.845        | 0.816        | <b>0.873</b> | <b>0.849</b> | 0.691        | 0.846        | 0.817        | <b>0.874</b> | 0.850        | 0.693        | 0.830        | 0.901        | 0.814        | 0.826        | 0.724        |
|   | MultiROCKET-Hydra | 0.817        | 0.809        | 0.826        | 0.819        | 0.635        | 0.825        | 0.816        | 0.834        | 0.826        | 0.652        | 0.803        | 0.891        | 0.798        | 0.800        | 0.684        |
| Baseline +<br>Base-pair<br>probability<br>(Standalone)<br>(cfg 3)   | ROCKET            | 0.842        | 0.828        | 0.855        | 0.844        | 0.684        | <b>0.855</b> | <b>0.856</b> | 0.854        | 0.855        | 0.710        | 0.795        | 0.885        | 0.783        | 0.789        | 0.670        |
|   | MiniROCKET        | 0.817        | 0.820        | 0.814        | 0.816        | 0.634        | 0.836        | 0.834        | 0.838        | 0.836        | 0.673        | 0.772        | 0.872        | 0.757        | 0.764        | 0.632        |
|   | MultiROCKET       | 0.822        | 0.813        | 0.832        | 0.824        | 0.645        | 0.825        | 0.831        | 0.820        | 0.824        | 0.651        | 0.758        | 0.866        | 0.747        | 0.750        | 0.612        |
|   | Hydra             | 0.846        | 0.827        | 0.865        | <b>0.849</b> | 0.693        | 0.851        | 0.840        | 0.861        | 0.852        | 0.702        | 0.789        | 0.879        | 0.769        | 0.780        | 0.658        |
|   | MultiROCKET-Hydra | 0.822        | 0.809        | 0.834        | 0.824        | 0.644        | 0.835        | 0.840        | 0.830        | 0.834        | 0.670        | 0.759        | 0.866        | 0.746        | 0.750        | 0.611        |
| Baseline +<br>Base-pair<br>probability<br>(Incorporated)<br>(cfg 4) | ROCKET            | 0.799        | 0.771        | 0.827        | 0.805        | 0.600        | 0.809        | 0.786        | 0.832        | 0.813        | 0.619        | 0.737        | 0.850        | 0.712        | 0.724        | 0.573        |
|   | MiniROCKET        | 0.776        | 0.756        | 0.797        | 0.781        | 0.554        | 0.801        | 0.808        | 0.794        | 0.799        | 0.603        | 0.705        | 0.835        | 0.675        | 0.684        | 0.521        |
|   | MultiROCKET       | 0.814        | 0.801        | 0.828        | 0.817        | 0.630        | 0.816        | 0.812        | 0.820        | 0.816        | 0.634        | 0.726        | 0.848        | 0.706        | 0.712        | 0.556        |
|   | Hydra             | 0.822        | 0.787        | 0.857        | 0.828        | 0.647        | 0.834        | 0.828        | 0.840        | 0.835        | 0.669        | 0.759        | 0.862        | 0.734        | 0.746        | 0.608        |
|   | MultiROCKET-Hydra | 0.814        | 0.802        | 0.820        | 0.817        | 0.629        | 0.820        | 0.825        | 0.816        | 0.819        | 0.642        | 0.736        | 0.853        | 0.717        | 0.723        | <b>0.874</b> |

Table 3.6: Channel ablation study. The best results are highlighted in **bold**.

We used single value mapping as the encoding method. Table 3.6 shows the result. From the table, we can see that the addition of secondary structure, base-pair probability as a standalone channel, and base-pair probability incorporated in the encoding of the complementary strand can improve the performance. We plotted the critical difference (CD) diagram as shown in Figure 3.6 to visualize Table 3.6 to make the performances of different combinations more obvious. In

CD diagrams, lower-ranked methods (toward the right) are better. A horizontal bar connecting combinations indicates no statistically significant difference.

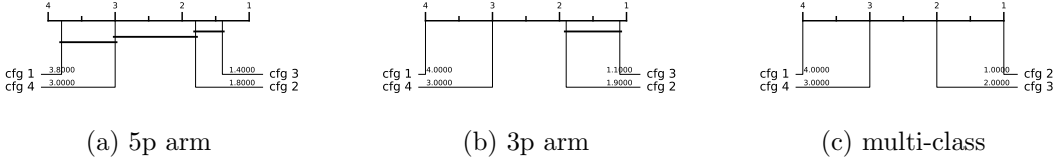


Figure 3.6: CD diagrams of channel ablation study.

From Figure 3.6, we can see that including time series derived from secondary structure information and base-pair probability as a separate channel can significantly improve the performance of the classifiers. Incorporating the base-pair probability sequence in the time series encoding of the complementary strand can also improve the classifier, but to a minor degree compared to serving as a standalone channel. In our downstream analysis, we adopted the combination of RNA sequence time series, secondary structure time series, and base-pair probability time series as our multivariate time series input, with 4 to 6 channels, depending on the encoding used.

### 3.3.2 Predictive Performance

The experiment was conducted on three datasets: the 5p arm, the 3p arm, and the multi-class datasets. Recall that we have nine encoding methods and five ROCKET-based classifiers. It results in 45 combinations of encoding methods and classifiers.

The result is shown in Table 3.7. The best combination of encoding method and classifier is shown in Table 3.8. For the 5p arm dataset, the best combination is “Global Cumulative grouped fixed-length channel mapping + ROCKET”. For all five classification metrics, it outperforms the state-of-the-art (SOTA) method, DiCleave. For the 3p arm dataset, the best combination is “Global Cumulative grouped fixed-length channel mapping + ROCKET”. Out of the five classification metrics, it outperforms DiCleave, except in specificity. For the multi-class dataset, the best combination is “Global Cumulative grouped fixed-length channel mapping + ROCKET”. For all five classification metrics, it outperforms DiCleave. Note that for the 3p arm and the multi-class datasets, the combination of “Cumulative grouped fixed-length channel mapping + ROKCET” also attains the best result.

To summarize Table 3.7, we plot the CD diagrams for finding the best classifier, as shown in Figure 3.7, and the best encoding method, as shown in Figure 3.8.

|   | Classifier        | 5p arm       |              |              |              |              | 3p arm       |              |              |              |              | multi-class  |              |              |              |              |
|---|-------------------|--------------|--------------|--------------|--------------|--------------|--------------|--------------|--------------|--------------|--------------|--------------|--------------|--------------|--------------|--------------|
|   |                   | Acc          | Sp           | Sn           | F1           | MCC          | Acc          | Sp           | Sn           | F1           | MCC          | Acc          | Sp           | Sn           | F1           | MCC          |
| Single value mapping<br>(enc 1)   | ROCKET            | 0.849        | 0.842        | 0.857        | 0.851        | 0.699        | 0.863        | 0.854        | 0.873        | 0.865        | 0.727        | 0.853        | 0.917        | 0.847        | 0.851        | 0.764        |
|   | MiniROCKET        | 0.823        | 0.809        | 0.837        | 0.825        | 0.647        | 0.823        | 0.828        | 0.817        | 0.822        | 0.647        | 0.835        | 0.906        | 0.828        | 0.833        | 0.735        |
|   | MultiROCKET       | 0.821        | 0.802        | 0.840        | 0.824        | 0.643        | 0.839        | 0.826        | 0.852        | 0.841        | 0.679        | 0.811        | 0.894        | 0.806        | 0.809        | 0.697        |
|   | Hydra             | 0.843        | 0.820        | 0.867        | 0.847        | 0.688        | 0.838        | 0.819        | 0.857        | 0.841        | 0.677        | 0.831        | 0.901        | 0.815        | 0.827        | 0.727        |
|   | MultiROCKET-Hydra | 0.820        | 0.803        | 0.837        | 0.823        | 0.640        | 0.840        | 0.830        | 0.850        | 0.841        | 0.680        | 0.816        | 0.896        | 0.810        | 0.814        | 0.704        |
| Grouped<br>variable-length<br>channel mapping<br>(enc 2)                      | ROCKET            | 0.835        | 0.826        | 0.844        | 0.836        | 0.670        | 0.855        | 0.849        | 0.861        | 0.856        | 0.710        | 0.846        | 0.913        | 0.839        | 0.844        | 0.752        |
|   | MiniROCKET        | 0.843        | 0.833        | 0.853        | 0.844        | 0.686        | 0.831        | 0.821        | 0.842        | 0.833        | 0.663        | 0.837        | 0.907        | 0.828        | 0.834        | 0.737        |
|   | MultiROCKET       | 0.819        | 0.809        | 0.828        | 0.820        | 0.638        | 0.817        | 0.814        | 0.820        | 0.818        | 0.634        | <b>0.890</b> | 0.894        | 0.806        | 0.808        | 0.695        |
|   | Hydra             | 0.825        | 0.780        | 0.869        | 0.832        | 0.653        | 0.811        | 0.769        | 0.854        | 0.819        | 0.626        | 0.818        | 0.892        | 0.765        | 0.812        | 0.705        |
|   | MultiROCKET-Hydra | 0.818        | 0.814        | 0.822        | 0.819        | 0.636        | 0.831        | 0.825        | 0.837        | 0.832        | 0.662        | 0.820        | 0.900        | 0.815        | 0.818        | 0.710        |
| Grouped<br>fixed-length<br>channel mapping<br>(enc 3)                         | ROCKET            | 0.851        | 0.843        | 0.859        | 0.852        | 0.702        | 0.863        | 0.850        | 0.875        | 0.864        | 0.726        | 0.849        | 0.915        | 0.843        | 0.847        | 0.757        |
|   | MiniROCKET        | 0.844        | 0.836        | 0.853        | 0.845        | 0.689        | 0.840        | 0.826        | 0.855        | 0.843        | 0.682        | 0.851        | 0.915        | 0.844        | 0.849        | 0.760        |
|   | MultiROCKET       | 0.831        | 0.815        | 0.848        | 0.834        | 0.663        | 0.824        | 0.813        | 0.836        | 0.826        | 0.649        | 0.811        | 0.896        | 0.808        | 0.808        | 0.698        |
|   | Hydra             | 0.848        | 0.816        | 0.880        | 0.853        | 0.699        | 0.862        | 0.829        | <b>0.884</b> | 0.864        | 0.724        | 0.843        | 0.908        | 0.837        | 0.839        | 0.746        |
|   | MultiROCKET-Hydra | 0.836        | 0.813        | 0.859        | 0.839        | 0.672        | 0.833        | 0.820        | 0.845        | 0.835        | 0.665        | 0.828        | 0.905        | 0.824        | 0.826        | 0.725        |
| Cumulative mapping<br>(enc 4)   | ROCKET            | 0.850        | 0.834        | 0.866        | 0.852        | 0.701        | 0.863        | 0.855        | 0.871        | 0.864        | 0.726        | 0.852        | 0.915        | 0.842        | 0.850        | 0.762        |
|   | MiniROCKET        | 0.840        | 0.821        | 0.860        | 0.843        | 0.682        | 0.840        | 0.837        | 0.844        | 0.841        | 0.682        | 0.843        | 0.911        | 0.835        | 0.840        | 0.747        |
|   | MultiROCKET       | 0.822        | 0.809        | 0.834        | 0.824        | 0.644        | 0.832        | 0.830        | 0.834        | 0.832        | 0.665        | 0.820        | 0.898        | 0.810        | 0.816        | 0.709        |
|   | Hydra             | 0.848        | 0.819        | 0.878        | 0.853        | 0.698        | 0.853        | 0.856        | 0.869        | 0.855        | 0.705        | 0.845        | 0.910        | 0.830        | 0.841        | 0.749        |
|   | MultiROCKET-Hydra | 0.824        | 0.811        | 0.856        | 0.825        | 0.647        | 0.838        | 0.833        | 0.843        | 0.839        | 0.677        | 0.821        | 0.898        | 0.810        | 0.817        | 0.711        |
| Cumulative grouped<br>variable-length<br>channel mapping<br>(enc 5)           | ROCKET            | 0.843        | 0.821        | 0.866        | 0.847        | 0.688        | 0.856        | 0.840        | 0.871        | 0.857        | 0.712        | 0.855        | 0.916        | 0.843        | 0.851        | 0.766        |
|   | MiniROCKET        | 0.845        | 0.826        | 0.865        | 0.848        | 0.691        | 0.836        | 0.833        | 0.838        | 0.836        | 0.672        | 0.840        | 0.909        | 0.833        | 0.838        | 0.742        |
|   | MultiROCKET       | 0.826        | 0.814        | 0.838        | 0.828        | 0.653        | 0.815        | 0.820        | 0.810        | 0.814        | 0.631        | 0.826        | 0.902        | 0.820        | 0.824        | 0.721        |
|   | Hydra             | 0.850        | 0.819        | 0.880        | 0.854        | 0.701        | 0.834        | 0.807        | 0.861        | 0.838        | 0.669        | 0.833        | 0.903        | 0.818        | 0.829        | 0.731        |
|   | MultiROCKET-Hydra | 0.824        | 0.810        | 0.838        | 0.826        | 0.649        | 0.833        | 0.833        | 0.833        | 0.833        | 0.666        | 0.830        | 0.903        | 0.821        | 0.827        | 0.726        |
| Cumulative grouped<br>fixed-length<br>channel mapping<br>(enc 6)              | ROCKET            | 0.856        | 0.836        | 0.876        | 0.858        | 0.712        | <b>0.870</b> | <b>0.861</b> | 0.879        | <b>0.871</b> | <b>0.741</b> | 0.863        | <b>0.921</b> | 0.852        | <b>0.860</b> | <b>0.780</b> |
|   | MiniROCKET        | 0.856        | 0.837        | 0.874        | 0.858        | 0.712        | 0.842        | 0.839        | 0.845        | 0.843        | 0.685        | 0.845        | 0.912        | 0.837        | 0.843        | 0.751        |
|   | MultiROCKET       | 0.820        | 0.802        | 0.839        | 0.824        | 0.642        | 0.798        | 0.798        | 0.798        | 0.798        | 0.597        | 0.809        | 0.894        | 0.806        | 0.807        | 0.694        |
|   | Hydra             | 0.850        | 0.814        | 0.885        | 0.855        | 0.701        | 0.855        | 0.840        | 0.869        | 0.857        | 0.711        | 0.847        | 0.910        | 0.831        | 0.843        | 0.752        |
|   | MultiROCKET-Hydra | 0.820        | 0.801        | 0.839        | 0.823        | 0.641        | 0.807        | 0.813        | 0.802        | 0.806        | 0.615        | 0.821        | 0.900        | 0.817        | 0.819        | 0.713        |
| Global<br>Cumulative mapping<br>(enc 7)                                       | ROCKET            | 0.850        | 0.834        | 0.866        | 0.852        | 0.701        | 0.863        | 0.855        | 0.871        | 0.864        | 0.726        | 0.852        | 0.915        | 0.842        | 0.850        | 0.762        |
|   | MiniROCKET        | 0.847        | 0.832        | 0.862        | 0.849        | 0.695        | 0.848        | 0.839        | 0.857        | 0.850        | 0.697        | 0.845        | 0.911        | 0.836        | 0.843        | 0.750        |
|   | MultiROCKET       | 0.827        | 0.819        | 0.834        | 0.828        | 0.653        | 0.847        | 0.842        | 0.853        | 0.848        | 0.695        | 0.825        | 0.901        | 0.817        | 0.822        | 0.718        |
|   | Hydra             | 0.851        | 0.821        | 0.880        | 0.855        | 0.703        | 0.861        | 0.848        | 0.874        | 0.863        | 0.722        | 0.847        | 0.911        | 0.834        | 0.844        | 0.753        |
|   | MultiROCKET-Hydra | 0.829        | 0.823        | 0.834        | 0.830        | 0.658        | 0.843        | 0.838        | 0.849        | 0.844        | 0.688        | 0.832        | 0.905        | 0.823        | 0.829        | 0.730        |
| Global<br>Cumulative grouped<br>variable-length<br>channel mapping<br>(enc 8) | ROCKET            | 0.840        | 0.814        | 0.867        | 0.844        | 0.682        | 0.853        | 0.838        | 0.867        | 0.854        | 0.706        | 0.856        | 0.917        | 0.845        | 0.853        | 0.768        |
|   | MiniROCKET        | 0.848        | 0.834        | 0.862        | 0.850        | 0.697        | 0.841        | 0.824        | 0.859        | 0.844        | 0.683        | 0.844        | 0.911        | <b>0.856</b> | 0.842        | 0.748        |
|   | MultiROCKET       | 0.834        | 0.826        | 0.839        | 0.834        | 0.668        | 0.831        | 0.821        | 0.842        | 0.833        | 0.663        | 0.828        | 0.904        | 0.823        | 0.826        | 0.724        |
|   | Hydra             | <b>0.857</b> | 0.821        | <b>0.894</b> | <b>0.862</b> | <b>0.717</b> | 0.822        | 0.786        | 0.857        | 0.828        | 0.645        | 0.826        | 0.898        | 0.806        | 0.820        | 0.717        |
|   | MultiROCKET-Hydra | 0.837        | 0.834        | 0.839        | 0.837        | 0.674        | 0.834        | 0.827        | 0.840        | 0.835        | 0.668        | 0.835        | 0.907        | 0.828        | 0.832        | 0.734        |
| Global<br>Cumulative grouped<br>fixed-length<br>channel mapping<br>(enc 9)    | ROCKET            | 0.856        | 0.836        | 0.876        | 0.858        | 0.712        | <b>0.870</b> | <b>0.861</b> | 0.879        | <b>0.871</b> | <b>0.741</b> | 0.863        | <b>0.921</b> | 0.852        | <b>0.860</b> | <b>0.780</b> |
|   | MiniROCKET        | <b>0.857</b> | <b>0.845</b> | 0.870        | 0.859        | 0.715        | 0.840        | 0.821        | 0.859        | 0.843        | 0.681        | 0.844        | 0.911        | 0.837        | 0.842        | 0.749        |
|   | MultiROCKET       | 0.829        | 0.825        | 0.833        | 0.830        | 0.658        | 0.820        | 0.816        | 0.823        | 0.820        | 0.640        | 0.819        | 0.900        | 0.816        | 0.817        | 0.710        |
|   | Hydra             | 0.856        | 0.817        | <b>0.894</b> | 0.861        | 0.713        | 0.859        | 0.838        | 0.880        | 0.862        | 0.719        | 0.846        | 0.911        | 0.832        | 0.843        | 0.752        |
|   | MultiROCKET-Hydra | 0.829        | 0.824        | 0.834        | 0.830        | 0.658        | 0.822        | 0.825        | 0.819        | 0.821        | 0.644        | 0.827        | 0.904        | 0.823        | 0.824        | 0.722        |

Table 3.7: Performance on the 45 combinations between encoding methods and the ROCKET-based classifiers. The best results are highlighted in **bold**.

| Dataset     | Methods            | Acc          | Sp           | Sn           | F1           | MCC          | Time (s)     |
|-------------|--------------------|--------------|--------------|--------------|--------------|--------------|--------------|
| 5p arm      | enc 9 + MiniROCKET | <b>0.857</b> | <b>0.845</b> | <b>0.870</b> | <b>0.859</b> | <b>0.715</b> | <b>0.787</b> |
|             | DiCleave           | 0.818        | 0.790        | 0.846        | 0.822        | 0.653        | 21.249       |
| 3p arm      | enc 9 + ROCKET     | <b>0.870</b> | 0.861        | <b>0.879</b> | <b>0.871</b> | <b>0.741</b> | 4.311        |
|             | enc 7 + MiniROCKET | 0.848        | 0.839        | 0.857        | 0.850        | 0.697        | <b>0.989</b> |
|             | DiCleave           | 0.854        | <b>0.891</b> | 0.817        | 0.847        | 0.715        | 15.919       |
| multi-class | enc 9 + ROCKET     | <b>0.863</b> | <b>0.921</b> | <b>0.852</b> | <b>0.860</b> | <b>0.780</b> | 12.208       |
|             | enc 3 + MiniROCKET | 0.851        | 0.915        | 0.844        | 0.849        | 0.760        | <b>4.550</b> |
|             | DiCleave           | 0.820        | 0.895        | 0.804        | 0.815        | 0.710        | 131.151      |

Table 3.8: Comparative analysis between MTSCCleav with the best combination of the encoding method and classifier, with the SOTA, DiCleave, on the three datasets. The best results of using MiniROCKET have also been shown to compare the computational efficiency. The best results are highlighted in **bold**.

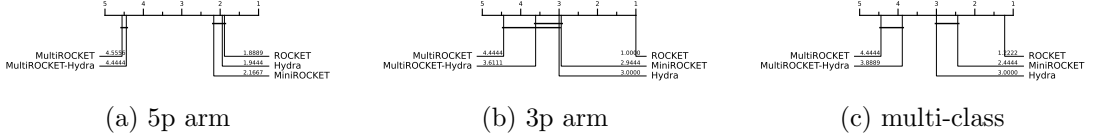


Figure 3.7: CD diagrams to compare different classifiers.

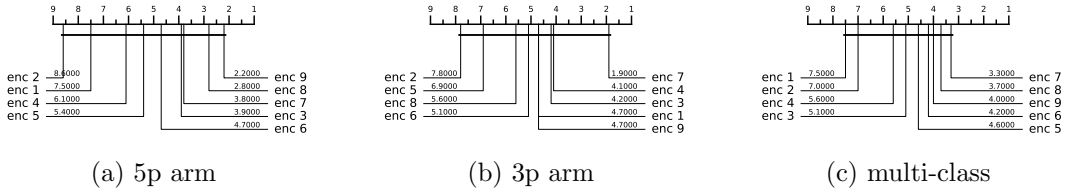


Figure 3.8: CD diagrams to compare different encoding methods.

### 3.3.3 Running Time Analysis

To compare the computational efficiency of MTSCCleav and DiCleave, we conducted a comparative analysis of their running times. For DiCleave, we employed the code from its supporting website<sup>12</sup>, without any modifications. All experiments were conducted on the same machine (a personal laptop equipped with an Apple M1 Pro chip and 16 GB of memory) and using the same splits of the training and test datasets under 5-fold cross-validation to ensure fairness. The reported running times are the averages of the five runs. The timing results were measured from the training phase to the return of the five classification metrics. The result is shown in Table 3.8. MiniROCKET is the most computationally efficient of the five rocket-based classifiers. We also included its best result, along with the corresponding encoding method, even though this combination may not be the best overall.

MTSCCleav demonstrated a significant advantage in computational efficiency, achieving an average 27.0X, 3.7X, and 10.7X speedup over DiCleave, for the 5p arm, 3p arm, and multi-class datasets, respectively. If we consider using the MiniROCKET in the case of 3p arm and multi-class datasets, it achieves 16.1X and 28.8X speedup. To note, in the case of the 3p arm dataset, the performance of MiniROCKET is only slightly worse than DiCleave. In the case of the multi-class dataset, even the performance of MiniROCKET is better than DiCleave. DiCleave is a deep learning-based method that requires substantial time for model inference, while MTSCCleav leverages efficient ROCKET-based classifiers. This significant

<sup>12</sup>

<https://github.com/MGuard0303/DiCleave> (Accessed on: 2025-07-13).

reduction in runtime makes MTSCCleav more suitable for large-scale data and real-time applications.

### 3.3.4 Subsequence Importance

To evaluate the sensitivity of MTSCCleav to subsequences of the input, we conducted a perturbation experiment to evaluate the importance of subsequences based on masking windows. The goal of this experiment is to identify which subsequences of the entire time series are critical for classification. We examine how various modifications to the original input impact model performance. It suggests which features are essential for classification.

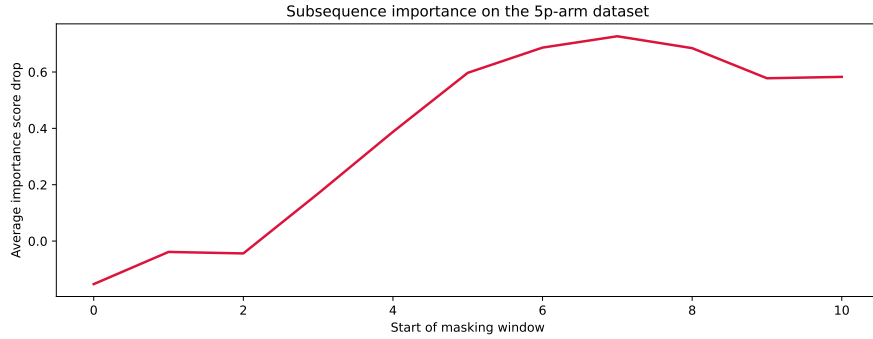
The model was trained on the original training dataset. For each instance in the test dataset, we measure its original score and the masked score. We slid a masking window  $w$  with a fixed length over the input time series  $T$ .  $|w|$  was set to 4. For each window position  $i \in \{1, 2, \dots, |T| - |w| + 1\}$ , we masked all entries across all the channels of  $T$  within the window. Hence, we removed or hid that portion of information from the model during inference. The changes in classification performance in terms of accuracy relative to the unmasked original score of each  $i$  are recorded. Intuitively, if the information of a subsequence is critical for the classification, the masking of this subsequence would lead to a great drop in classification performance. We aggregated the importance score across the test dataset.

The result is shown in Figure 3.9. For the encoding methods, we cannot use the methods derived from the cumulative mapping because the accumulation would leak information from the masked region. We adopted “Grouped fixed-length channel mapping” as the encoding method and ROCKET as the classifier. “Grouped fixed-length channel mapping” is the best encoding, other than the methods derived from the cumulative mapping, in all datasets, as shown in Figure 3.8. ROCKET is the best classifier, as shown in Figure 3.7..

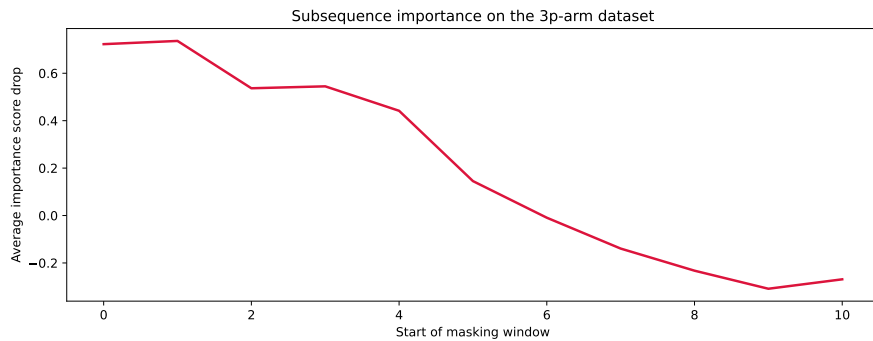
In the 5p arm dataset, we found that masking subsequences at the tailing part caused a significant drop in the importance score, as shown in Figure 3.9 (a). In the 3p arm dataset, we found that masking subsequences at the leading part caused a significant drop in the importance score, as shown in Figure 3.9 (b).

### 3.3.5 Summary

Our method achieves better or comparable predictive results and a 3.7X to 28.8X speedup compared to the state-of-the-art (SOTA).



(a) 5p arm



(b) 3p arm

Figure 3.9: Results of the perturbation experiment.

### 3.4 Discussion

The channel ablation study reveals that the involvement of the time series derived from the secondary structure can improve accuracy. It suggests the importance of RNA folding in dicer processing. Furthermore, we found that the base-pair probability sequence of the secondary structure can also enhance accuracy. To the best of our knowledge, it is a novel application of the base-pair probability sequence. Experiments show that using the probability sequence as an additional channel can enhance accuracy more than incorporating it in the encoding. It is likely because keeping it as an additional channel can preserve more information, of both the probability sequence itself and the complementary strand.

Out of the three datasets, the best classifier is ROCKET. The ranking of the five classifiers by performance, starting from the best, is as follows: ROCKET, Hydra, MiniROCKET, MultiROCKET-Hydra, and MultiROCKET. It indicates that the features created from the pooling operations that are only in MultiROCKET but not in MiniROCKET, confuse the final classifier. They are mean of positive values (MPV), mean of indices of positive values (MIPV) and longest stretch of

positive values (LSPV) [43]. In contrast, the pooling operator that is only present in ROCKET but not in MiniROCKET, enhances the classification performance. It is maximum (MAX).

For the encoding methods, we have the following observations. Fixed-length grouped channel mappings outperform variable-length counterparts with one exception in the multi-class dataset, likely because fixed-length schemes better preserve the original positional information of nucleotides within the sequence. Global cumulative methods consistently yield better performance than local cumulative methods. It suggests that the upstream information of the cleavage pattern plays a critical role in identifying cleavage sites. Cumulative-based encodings perform better than single-value mappings, with one exception in the 3p dataset, suggesting that the accumulated nucleotide signal is more informative for cleavage site prediction than the local or isolated presence of nucleotides. In the 5p arm dataset, encoding RNA sequence in two channels appears to worsen the result. This suggests that the 5p arm dataset and the 3p arm dataset need different nucleotide grouping methods for the encoding.

One limitation of DiCleave is overfitting during training because of the relatively small size of the dataset [21]. DiCleave is a deep learning-based method. Deep learning models typically require a large amount of training data to generalize effectively. They are data-hungry. In contrast, MTSCCleav leverages ROCKET-based methods for the classification. They rely on random convolutional feature extraction followed by a simple linear classifier. The Ridge classifier used in this study is less data-hungry compared to deep learning methods due to its use of L2 regularization and the simplicity of its linear model nature. It allows ROCKET-based classifiers, and hence MTSCCleav, to maintain strong predictive performance even in settings with a relatively small dataset size.

The subsequence importance reveals some connections between RNA secondary structure and human dicer cleavage site prediction. The perturbation experiment shows that the leading part of 5p arm and the tailing part of 3p arm are important for the classification. These parts are close to the center of the RNA secondary structure of pre-miRNA. It indicates that the center region is more crucial for human dicer cleavage site prediction. It is consistent with the previous study [20].

### 3.5 Concluding Remarks

We proposed an accurate, fast, and simple multivariate time series classification (MTSC)-based method, termed MTSCCleav, for predicting human dicer cleavage

sites. Base-pair probability sequences of the secondary structures have also been leveraged in the classification. MTSCCleav consists of three parts: time series encoding, time series transformation, and classification. ROCKET-based methods were used for time series transformation. Ridge Classifier was used for classification. For the computational experiments, we evaluated nine time series encoding methods in conjunction with five time series transformation methods. MTSCCleav outperformed the SOTA method in all five evaluation metrics for the 5p-arm and multi-class datasets, and four of the metrics for the 3p-arm dataset. In terms of computational efficiency, MTSCCleav with the optimal setting achieved an average 3.7X to 27.0X speedup over the SOTA method on the three datasets. With the use of a less accurate but faster time series classification method, MTSCCleav achieved an average speedup of 16.1X to 28.8X, respectively. We analyzed the subsequence importance of the input multivariate time series. The results show that subsequences near the center of the pre-miRNA sequences are more important. This aligns with the findings from previous work. This study demonstrates that time series analysis provides a powerful alternative to conventional modeling in the context of RNA processing. This framework may be extended to other RNA-processing tasks. Notably, the encoding of RNA sequence into time series enables us to utilize any well-established tools from the time series community.

# Chapter 4

## Scaling with Multiple Scaling Factors in Time Series Searching

Time series data are ubiquitous across many different fields. Many data mining tasks, such as classification, clustering, and motif finding, have been defined for time series data. They utilize similarity search as a core subroutine, making it crucial to design similarity measures that align with our intuitions. To facilitate efficient computation, speedup techniques are essential. Dynamic Time Warping (DTW) is arguably the most prevailing distance measure for time series data. However, studies have shown that for certain data, another distance measure, namely Uniform Scaling (US), is equally crucial as DTW. DTW handles the local distortion, while US handles the global scaling. In addition, studies have demonstrated that combining DTW and US is necessary to obtain meaningful results in some cases. Surprisingly, all existing studies employ only a single scaling factor for the entire time series. A time series could consist of phases. Since each phase of a time series expresses at its own rate, using a single scaling factor is insufficient when comparing two time series that share similar phases but differ in their expression rates. We introduce the first framework that accounts for multiple scaling factors, Piecewise Scaling Distance (PSD). PSD employs other existing distance measures as subroutines. Because the naive implementation of PSD is slow, we propose a constrained version of PSD that enforces constraints based on the allowed segment lengths derived from the given scaling factor bound. It also prevents pathological results. In addition, two other speedup techniques have been proposed, which achieve 10.10X to 191.46X speedup. We also demonstrate the usage of a lower bound when DTW is used as the subroutine of PSD. More-

over, we show that the segmentation results returned by PSD can improve the accuracy of other distance measures.

## 4.1 Background

To study the mechanism of a process, we take measurements. Measurements are usually taken continuously by the sensors. Measurements of processes always yield continuous values at discrete timestamps. They are time series data. For example, smartphones collect users' GPS data. ECG monitors measure patients' heart rate. The continuous measurements compose a time series. It is not hard to see why time series data are ubiquitous across many different fields. In GPS data, each time series data point consists of the user's latitude and longitude information. They are multivariate time series. In ECG data, each data point represents the amplitude of the patient's cardiac electrical activity. They are univariate time series. In this study, we focus on univariate time series.

Many data mining tasks can be defined on time series data. For example, given a time series database, we can perform clustering based on the pairwise similarity of the time series instances. A classifier can be trained when categorical labels are available. Alternatively, given a long time series, for motif finding, we identify recurring patterns. In contrast, for anomaly detection, we identify abnormal subsequences. Almost all time series data mining tasks can be reduced to arguing the similarity between two time series. A good distance measure, also known as a similarity measure, can determine the success or failure of the algorithms built on it. The choice of an appropriate distance measure is particularly evident in classification. Studies show that simple nearest-neighbor classification (1-NN) is difficult to beat and can compete with more complex methods [39].

A time series is treated as a whole rather than as a collection of individual values. The relationships between values are important. They constitute trends and shapes. Hence, similarity search in time series data is approximate-based rather than exact match-based [47]. Besides, different invariances should be allowed during the comparison.

Dynamic Time Warping (DTW) is one of, if not the most common, similarity measures. DTW provides invariance to time distortion by aligning and measuring the similarity between two series that may be misaligned in time. However, it assumes that the time series are expressed on a similar global expression rate. This assumption limits its performance when comparing two time series expressed at different global expression rates. We often see this behavior in domains such as

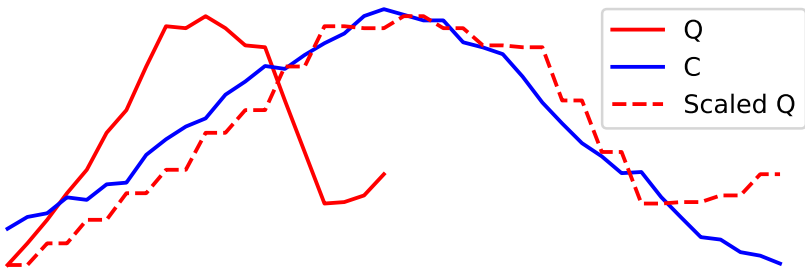


Figure 4.1: Applying nearest neighbor interpolation on  $Q$ , which result in Scaled  $Q$ , that can better reflect its similarity with  $C$ .

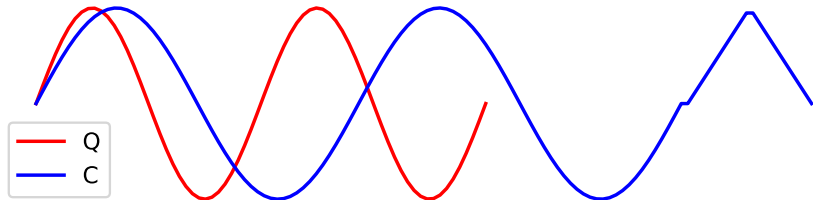


Figure 4.2:  $Q$  and  $C$  are in different rates. A stretching version of  $Q$  is similar to a prefix of  $C$ , but not the whole  $C$ .

speech recognition, motion analysis, patient biomedical signals, and sensor data in the manufacturing industry.

Uniform Scaling (US) can achieve global scaling invariance by scaling the two time series to the same length via interpolation, such as nearest-neighbor interpolation, before comparison, as shown in Figures 4.1. It is reported that in some domains, such as gestures [48, 49] and music performance [50], the scaling is about 10-15% (i.e., scaling factors: 1.1 to 1.15). The scaling factors are relatively small, since the nature of the music and the gait will change with significant scaling factors. However, in some other domains, we may encounter larger scaling factors. In bioinformatics, gene expression time series data could differ by a factor of 1.41 [51, 52]. In Figure 4.2,  $Q$  and a prefix of  $C$  are similar, but at different rates. In searching, we typically have a query  $Q$  and a longer candidate  $C$ . We seek a prefix of  $C$  that is close to  $Q$ . For better comparison, we need to eliminate the scaling effect. These observations demonstrate the necessity of uniform scaling.

DTW and US are used to achieve different kinds of invariance. DTW handles local distortion, while US handles global scaling. Furthermore, some studies show that the combination of US and DTW, namely USDTW, better reflects similarity [53, 54, 55]. US is first applied to transform the two time series into the same length to eliminate the effect resulting from the different rates. Then, DTW,

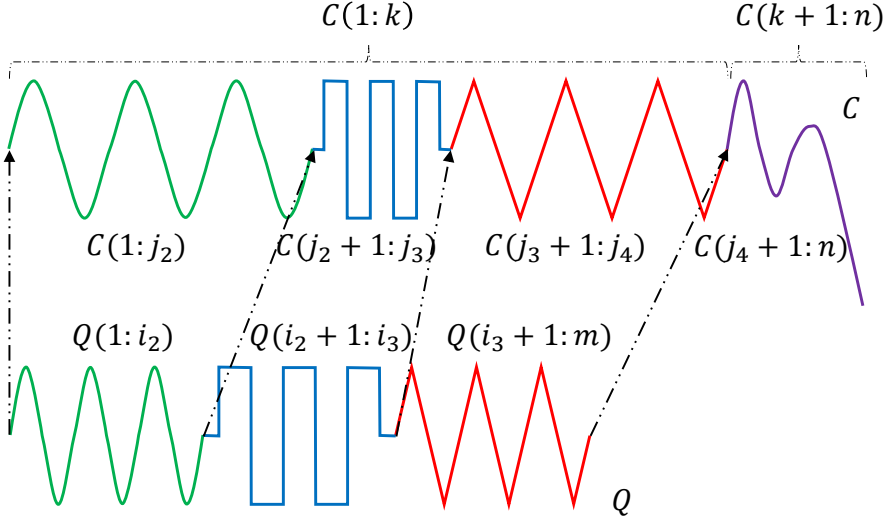


Figure 4.3: Intuition of piecewise scaling (PS).

rather than ED, is applied to address local misalignment. USDTW is computationally more expensive than DTW because it involves the calculation of the DTW between  $Q$  and different lengths of each prefix of  $C$ . The different lengths of the prefixes correspond to different scaling factors.

It is not uncommon for the data sampling strategy to change over time [56]. There are different phases, each with its own rate. To achieve invariance for this kind of scaling effect resulting from multiple rates, rather than using a single scaling factor, it is beneficial to identify these different phases and use the appropriate scaling factors for these segments, also known as pieces. We refer to this as piecewise scaling (PS). Figure 4.3 shows the intuition of PS. The prefix of  $C$  (i.e.,  $C(1 : k)$ ) and  $Q$  share the same set of segments, but each has a different scaling. Multiple scaling factors must be used. It motivates us to design a new distance measure or framework that considers applying a scaling factor on each of the phases as defined by dashed lines in Figure 4.3, during the comparison of two time series.

Our contributions are as follows:

- We propose the first framework to achieve piecewise scaling (PS) invariance. In particular, we focus on two instantiations of PSD, namely PSED (i.e., ED with PS invariance) and PSDTW (i.e., DTW with PS invariance).
- We design a dynamic programming method to compute PSD.
- We propose a constrained version of PSD (cPSD) based on the allowed segment lengths. Besides, two other speedup techniques have been proposed.

For a particular instantiation of PSD, PDTW, we demonstrate the usage of a lower bound to further speed it up.

- We demonstrate that the segmentation results returned by PSD can improve the accuracy of other distance measures.

The rest of this study is structured as follows. We present related work in Section 5.2 and preliminaries in Section 4.3. Section 5.3 introduces our new distance measure framework, its constrained version, and speedup techniques. It is experimentally demonstrated in Section 4.5 for the problem of querying. In Section 5.5, we conclude this study with some future work.

## 4.2 Related Work

This study focuses on distance measures of time series. For the overall review of time series, we direct the readers to [47, 57] for a more comprehensive understanding of this field.

For many tasks, having appropriate distance measures that align with our intuition for the domains we work with is essential. One well-known distance measure is Dynamic Time Warping (DTW). It is initially designed for speech analysis [3]. However, DTW is computationally expensive. Lower bounds are used to speed up time series similarity search by admissibly pruning the unpromising candidates. One of the popular exact lower bounds of DTW is  $\text{LB}_{\text{Keogh}}$ . [58] improves the scalability of DTW by introducing a subsequence search suite of their four novel ideas, namely the UCR suite. For an overall review of lower bounds, we refer readers to [59, 60]. There is an approximate algorithm that approximates DTW with high accuracy while drastically cutting down the time and space requirements [61].

While ED is sensitive to distortions in the time axis, uniform scaling (US) has been shown to be a critical invariance in domains such as motion capture. [62] demonstrated that DTW is insufficient for handling global scaling effects, and that identifying DTW is not the solution to achieve this kind of invariance. There is a need for US. [63] extends the importance of uniform scaling to motif discovery. The authors show that meaningful motifs often suffer from a global scaling effect, causing standard motif finding algorithms to miss them completely.

To the best of our knowledge, three studies analyze the combination of US and DTW, namely USDTW. It was first proposed by [53]. It extended  $\text{LB}_{\text{Keogh}}$  to bound the USDTW. However, the extended  $\text{LB}_{\text{Keogh}}$  is still too loose with

invariance to large amounts of uniform scaling. [54] and its follow-up study [55] proposed a new lower bound <sup>1</sup>, namely  $\text{LB}_{\text{Shen}}$ , which has been shown to be tighter than  $\text{LB}_{\text{Keogh}}$  on USDTW.

To our surprise, despite a fruitful discussion of DTW, US, and USDTW, no study has proposed a distance measure capable of handling scaling effects across multiple scaling factors. This is precisely what we will address in this study.

### 4.3 Preliminaries

We refer to time as the contextual attribute because it provides the context for the measurements to be made. We refer to the measurements as the behavioral attributes. Time series are multivariate when more than one behavioral attribute is present. Otherwise, it is called univariate. We focus on the univariate case.

**Definition 1** (Time Series). A time series  $T = t_1, t_2, \dots, t_n$  is a sequence of real-valued numbers with length  $= n$ .

When two time series are involved in the discussion, we denote them as  $Q$  (Query) and  $C$  (Candidate), with lengths  $m$  and  $n$ , respectively. Since  $Q$  is the query sequence, it is not longer than  $C$  (i.e.,  $m \leq n$ ). The requirement of “ $m \leq n$ ” is a natural setting. In “Query by Content”, a user is going to search for a candidate in the database from a user-input query in which the query may only contain partial information of the target candidate. For example, a user often wants to find a song or tune that is lingering in their head by humming a part but not whole of the tune [64]. We are also interested in a segment or subsequence of a time series.

**Definition 2** (Subsequence). A subsequence  $T(i : j)$  of a time series  $T$  is a shorter time series that starts from position  $i$  and ends at position  $j$  with length  $= j - i + 1$ . Both ends are inclusive. Formally,  $T(i : j) = t_i, t_{i+1}, \dots, t_j$ ,  $1 \leq i \leq j \leq n$ .

We call  $T(1 : j)$  the prefix of  $T$  of length  $j$ .

Before comparison, we need to standardize or normalize them. A common way is Z-Normalization, which is  $T = (T - \text{mean}(T)) / \text{std}(T)$ , as shown in Figure 4.4. The most fundamental distance measure is the Euclidean Distance (ED).

---

<sup>1</sup>It is denoted as  $\text{LB}_{\text{New}}$  in the original study. We rename it to prevent any confusion.

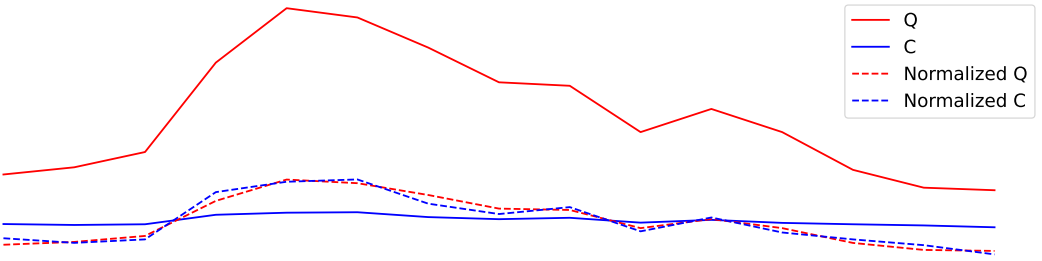


Figure 4.4: Z-normalization. Resulting time series have mean = 0 and std = 1.

### 4.3.1 Euclidean Distance (ED)

Given two points on a plane, it is intuitive to define the distance between them as the length of the line segment between them. This idea extends to the case of  $n$ -dimensions in time series with length  $n$ .

**Definition 3** (Euclidean Distance (ED)). Given two series  $Q$  and  $C$  both with length  $n$ , the Euclidean Distance between them is defined as:

$$\text{ED}(Q, C) = \sqrt{\sum_{i=1}^n (q_i - c_i)^2} \quad (4.1)$$

A square root is usually involved in the computation of distance measures. It is a monotonic function. Since it does not change the relative ranking of the results, we can omit the square root operation for simplicity and optimization. ED aligns the entries between two series in a one-to-one manner. Two similar series will have a large distance under ED if they are not aligned well in the time dimension. ED cannot handle local distortion along the time axis because warping in the alignment is not allowed. A standard distance measure that provides warping invariance is called Dynamic Time Warping (DTW).

### 4.3.2 Dynamic Time Warping (DTW)

Dynamic Time Warping (DTW) is an algorithm that measures similarity between two time series while accounting for local distortions. DTW aligns the two series by nonlinearly warping the time axis to minimize the final cumulative distance.

Given two time series,  $Q$  and  $C$ , we first construct an  $m$  by  $n$  distance matrix  $M$ . The origin  $(1, 1)$  is set at the bottom-left element of  $M$ . The  $(i, j)$  element of  $M$  contains the distance  $d(q_i, c_j)$  between points  $q_i$  and  $c_j$ . This local distance

$d(\cdot, \cdot)$  is usually calculated by  $(q_i - c_j)^2$ . Each  $(i, j)$  element refers to an alignment or mapping of the two points. A contiguous set of such elements forms a warping path  $W$ .  $W$  represents the non-linear alignment of  $Q$  and  $C$ .  $W = w_1, w_2, \dots, w_K$  in which  $w_k = (i, j)_k$  represents the mapping between  $q_i$  in  $Q$  and  $c_j$  in  $C$ , where  $\max(m, n) \leq K \leq m+n-1$ . “ $\max(m, n) \leq K$ ” because the alignment of two series must include every point in both  $Q$  and  $C$ . “ $K \leq m+n-1$ ” because the longest warping path is either the “concatenation of the bottom row and the rightmost column” (with the bottom-right cell being overlapped) or the “concatenation of the leftmost column and the top row” (with the top-left cell being overlapped).

The warping path  $W$  is typically subject to the following three constraints.

- Boundary conditions:  $w_1 = (1, 1)$  and  $w_K = (m, n)$ . The first (last) point of  $Q$  must map to that of  $C$ .
- Continuity: Given  $w_k = (i, j)$  and  $w_{k-1} = (i', j')$ ,  $i - i' \leq 1$  and  $j - j' \leq 1$ . An entry in the warping path  $W$  is adjacent to its one-step previous entry.
- Monotonicity: Given  $w_k = (i, j)$  and  $w_{k-1} = (i', j')$ ,  $i - i' \geq 0$  and  $j - j' \geq 0$ . The warping path  $W$  does not go back.

We denote  $W^*$  as a set of all allowed possible paths.

**Definition 4** (Dynamic Time Warping (DTW) [3]). DTW returns the minimum warping cost:

$$\text{DTW}(Q, C) = \min_{W \in W^*} \sum_{k=1}^{|W|} w_k \quad (4.2)$$

To find the minimum warping cost and its corresponding warping path, we can use dynamic programming (DP) to evaluate the following recurrence.

$$D(i, j) = d(q_i, c_j) + \min \begin{cases} D(i-1, j-1), \\ D(i-1, j), \\ D(i, j-1) \end{cases} \quad (4.3)$$

It can be solved by building the accumulated cost matrix  $D$ , where the y-axis refers to  $Q$ , and the x-axis refers to  $C$ . The base cases, which are the first row and the first column, are defined as  $D(1, j) = \sum_{k=1}^j d(q_1, c_k), j \in [1, n]$  and  $D(i, 1) = \sum_{k=1}^i d(q_k, c_1), i \in [1, m]$ . After we have initialized the base cases, we

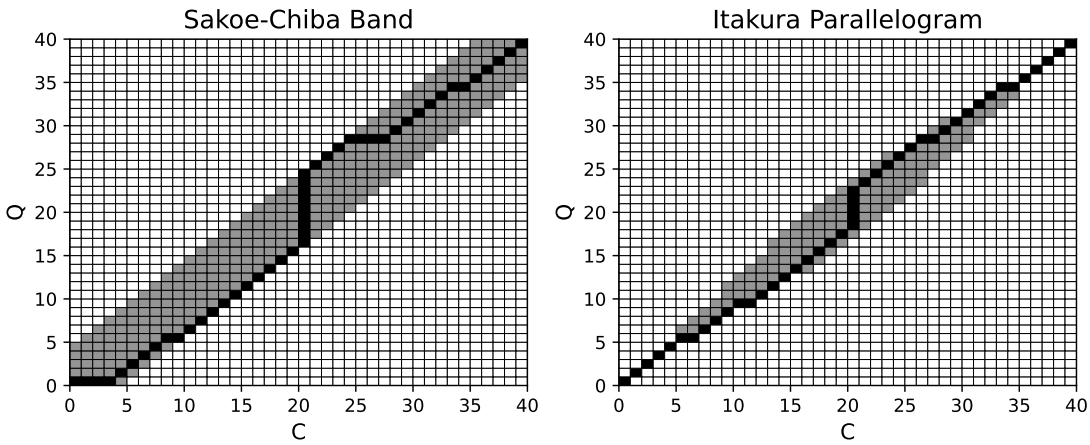


Figure 4.5: Visualization of  $D$  with local constraints. The black cells form the warping path.

can fill up  $D$  starting from the bottom up. There are  $m \times n$  entries in  $D$ . It takes  $\mathcal{O}(mn)$  to fill it up. Once  $D$  is built, we can find the path corresponding to this minimum cost by simple backtracking from the end cell  $D(m, n)$  to the origin cell  $D(1, 1)$ .

Some constraints have been proposed to prevent pathological warping paths with the aim of accuracy and efficiency. Two of the most popular are Sakoe-Chiba Band [3] and Itakura Parallelogram [65]. They only allow the warping paths to pass through the allowed region, as shown in Figure 4.5, by setting the cells outside this region in  $D$  to have  $\infty$  accumulated distance cost. [66] suggested that these constraints can be viewed as constraints on the warping path entry  $w_k = (i, j)_k$ . It represents these constraints as inequalities applying to the indices  $i$  and  $j$  locally, without depending on the main diagonal in  $D$ . In the Sakoe-Chiba Band, the constraints can be represented as  $j - r \leq i \leq j + r$ , where  $r$  is an integer. It is sometimes specified as a fraction (or percentage) of the longer time series length to ensure length invariance. For clarity, we assume  $r$  is an integer unless specified otherwise. This means that  $q_i$  can only align with  $c_j$  if their indices differ by at most  $r$ . Since  $r$  defines the maximum allowed difference between the mapping indices,  $|n - m| \leq r$ , to ensure that the end points of  $Q$  and  $C$  can map. In the Itakura Parallelogram,  $r$  is a function of  $i$  rather than a constant value. ED can be seen as a special case of DTW where the warping path is fixed to be diagonal.  $q_i$  aligns to  $c_i$  for every  $i$  (i.e.,  $r = 0$ ). DTW minimizes over all possible warping paths, and the warping path of ED is one of them. Because of the band, we only need to fill up the cells within the band. The complexity is  $\mathcal{O}(\# \text{of\_cells\_inside})$ .

In the case of the Sakoe-Chiba Band, the band has a constant width  $w = 2r + 1$ . The complexity becomes  $\mathcal{O}(w \times \text{length\_of\_diagonal}) = \mathcal{O}(rn)$ . The constrained DTW is denoted as  $\text{DTW}_r$ .

### 4.3.3 Uniform Scaling (US)

In US, we compare the whole sequence of  $Q$  to a prefix of  $C$ , as shown in Figure 4.2. The two compared sequences are scaled to the same length via interpolation before ED is applied. A common interpolation method is nearest neighbor interpolation.

**Definition 5** (Nearest Neighbor Interpolation). Given a time series  $T$  of length  $n$  and an integer  $L$ , Nearest Neighbor Interpolation scales  $T$  into  $T^L$  as follows:

$$T_j^L = T_{\lceil n(j/L) \rceil} \quad \text{where } 1 \leq j \leq L \quad (4.4)$$

We can scale up or down a given series using Equation 4.4, as shown in Example 1.

**Example 1.** Given a series  $T = 1, 2, \dots, 6$  with length  $n = 6$ . Let  $T(1 : 4)$  be the prefix of  $T$  of length  $k = 4$  (i.e.,  $T(1 : 4) = 1, 2, 3, 4$ ). Given an integer  $L = 8$ , we compute  $T(1 : 4)^8$  as follows.

$$\begin{aligned} T(1 : 4)^8 &= T_{\lceil 4(1/8) \rceil}, T_{\lceil 4(2/8) \rceil}, T_{\lceil 4(3/8) \rceil}, \dots, T_{\lceil 4(8/8) \rceil} \\ &= T_1, T_1, T_2, \dots, T_4 \\ &= 1, 1, 2, \dots, 4. \end{aligned}$$

When  $L > k$ ,  $T$  is said to be stretched. When  $L < k$ ,  $T$  is said to be shrunk.

**Definition 6** (Uniform Scaling (US) [62]). Given two series  $Q$  and  $C$ , of length  $m$  and  $n$  respectively, and a scaling factor bound  $l$ , where  $l \geq 1$ . Let  $C(1 : k)$  be the prefix of  $C$ , where  $\lceil m/l \rceil \leq k \leq \min(\lfloor lm \rfloor, n)$ , and  $C(1 : k)^L$  be a rescaled version of  $C(1 : k)$  with length  $L$ , where  $L = \min(\lfloor lm \rfloor, n)$ .  $L$  is called the alignment factor.  $\min(\lfloor lm \rfloor, n)$  is the largest alignment factor.

$$\text{US}(Q, C, l, L) = \min_{k=\lceil m/l \rceil}^{\min(\lfloor lm \rfloor, n)} \text{ED}(Q^L, C(1 : k)^L) \quad (4.5)$$

$L$  is set as the largest alignment factor [55] to ensure all the points in  $Q$  and  $C(1 : k)$  are preserved during interpolation because of up-sampling, and the scaled version of all the prefixes is going to have the same length (i.e.,  $L$ ), for fair

comparison, since comparison between two longer time series generally results in a larger distance measure. Through Equation 4.5, we find the minimum value and the corresponding argument (i.e.,  $k$ ) by checking the minimum value of the ED function from  $\lceil m/l \rceil$  to  $\min(\lfloor lm \rfloor, n)$ . The scaling factor is defined by the argument minimum value of  $k$ . The smaller  $k$  is, the more we need to “stretch”  $C$  for  $Q$  to compare with  $C(1:k)$ , which is  $m/k$  times.

Consider a time series database  $D$  comprising a set of candidate instances, and a single query series  $Q$ . The search task aims to retrieve the most similar instance (or top- $k$  instances) from  $D$  to  $Q$ . We maintain  $Q$  as a fixed reference and extract only the prefixes from each instance in  $D$  for comparison. Furthermore, to simplify notation, we apply scaling exclusively to the instances in  $D$ , leaving  $Q$  unscaled.

#### 4.3.4 Uniform Scaling & Dynamic Time Warping (US-DTW)

Uniform Scaling & Dynamic Time Warping (USDTW) measures the similarity by applying scaling with an appropriate scaling factor on  $C$  and then applying DTW. The tail part of  $C$  can be ignored, as shown in Figure 4.2.

**Definition 7** (Uniform Scaling & Dynamic Time Warping (USDTW) [55]). With the same notations defined in Definition 6,

$$\text{USDTW}_r(Q, C, l, L) = \min_{k=\lceil m/l \rceil}^{\min(\lfloor lm \rfloor, n)} \text{DTW}_r(Q^L, C(1:k)^L) \quad (4.6)$$

where  $r$  is the DTW constraint parameter.

We replace the ED function in Equation 4.5 by DTW function to form Equation 4.6.

As mentioned in Section 5.1, there may exist more than one scaling factor. Hence, both the existing distance measures, US and USDTW, which are designed to handle only one scaling factor, are insufficient. This motivates us to design a new framework of distance measures.

#### 4.3.5 Lower Bounds for DTW and USDTW

We first introduce the concept of lower bounds and explain how they can benefit search. DTW is computationally more expensive than ED. They compute an

accumulated cost matrix of size  $m \times n$ , where  $m$  and  $n$  denote the lengths of the two time series. It results in quadratic complexity. This complexity poses a challenge for similarity search. The most common approach is to compute a lower bound of the real value, which is computationally cheap and tight. We can use this lower bound to filter out unpromising candidates and perform the expensive distance computation only on the small set of promising candidates. In searching, we would keep track of the best\_so\_far distance  $\text{bsf}$  between the query  $Q$  and the testing candidates. When testing a new candidate  $C$ , we first compute the  $\text{LB}(Q, C)$ . We only compute the actual DTW when  $\text{LB}(Q, C) \leq \text{bsf}$ .

We then introduce some common lower bounds.

**Kim Lower Bound [67]:**  $\text{LB}_{\text{Kim}}$  is a simple and fast lower bound of DTW. The complexity is  $O(1)$ . It uses the four features in  $Q$  and  $C$ . We denote  $t_{-1}$  as the last point and  $t_{\max}$  ( $t_{\min}$ ) as the maximum (minimum) point in time series  $T$ .

$$\text{LB}_{\text{Kim}} = \max \begin{cases} d(q_1, c_1) \\ d(q_{-1}, c_{-1}) \\ d(q_{\max}, c_{\max}) \\ d(q_{\min}, c_{\min}) \end{cases} \quad (4.7)$$

$d(\cdot, \cdot)$  refers to the local distance used in the point alignment. The first two lines come from the boundary condition in DTW. The alignment between the first pair of points and the last pair of points must contribute to the accumulated sum of DTW. Each point in  $Q$  must align with some point in  $C$ , and vice versa. Each alignment contributes a local distance to the final sum. The minimum possible local distance for the alignment of  $q_{\max}$  would be the one aligned with  $c_{\max}$ . The same applies to the last line in the equation.

There is a simplification of  $\text{LB}_{\text{Kim}}$ . Only the first and last pair are used in the lower bound computation. In the normalized time series, the third and fourth rows in Equation 4.7 should have small values [58]. Ignoring them can improve the complexity from  $\mathcal{O}(n)$  to  $\mathcal{O}(1)$ . The simplified lower bound is  $\text{LB}_{\text{KimFL}} = d(q_1, c_1) + d(q_{-1}, c_{-1})$ .

**Keogh Lower Bound [66]:**  $\text{LB}_{\text{Keogh}}$  builds the upper  $U$  and lower envelopes  $L$  of one of the time series out of the two compared sequences. Usually, the envelopes are constructed for  $Q$  instead of  $C$  as we will compare one  $Q$  against many  $C$ 's. Otherwise, we need to build the envelopes for each candidate instead [58].

To the best of our knowledge, they are the first to interpret the constraint as a restriction on the indices of the warping path  $w_k = (i, j)_k$  such that  $j - r \leq i \leq$

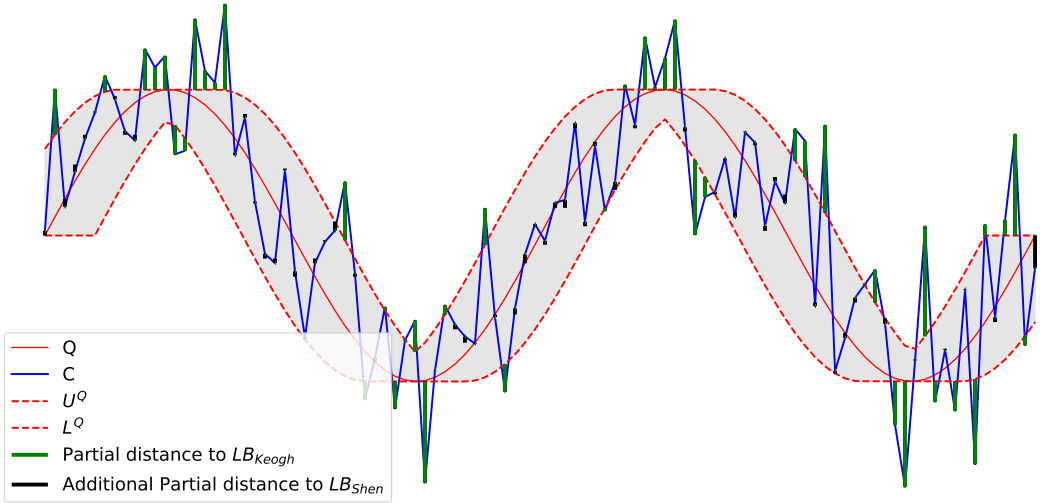


Figure 4.6: Visualization of  $\text{LB}_{\text{Keogh}}$  and  $\text{LB}_{\text{Shen}}$

$j + r$ , where  $r$  defines the allowable deviation of alignment between  $q_i$  and  $c_j$ . For ease of exposition, we focus on the most used constraint in the literature, which is the Sakoe-Chiba Band [68]. Two sequences are constructed for  $Q$ , namely the upper  $U^Q$  and lower envelopes  $L^Q$  of  $Q$  as shown in Figure 4.6. For each  $q_i$ , we would assign a window of  $q_i$  based on its index  $i$  as follows.

$$\begin{aligned} U_i^Q &= \max(q_{\max(1,i-r)} : q_{\min(i+r,m)}) \\ L_i^Q &= \min(q_{\max(1,i-r)} : q_{\min(i+r,m)}) \end{aligned} \quad (4.8)$$

$\max(1, \cdot)$  and  $\min(\cdot, m)$  are used for handling the boundary cases.  $U^Q$  and  $L^Q$  together form a bounding envelope that encloses the original  $Q$ , it is the grey region in the figure. For each  $c_j$ , either  $(c_j, U_j^Q)$  or  $(c_j, L_j^Q)$  corresponds to the possible alignment that contributes the minimum distances if  $c_j$  falls outside the envelope. Herein, the lower bound is the sum of these distances, as shown in the following equation.

$$\text{LB}_{\text{Keogh}}(Q, C) = \sum_{j=1}^n \begin{cases} d(c_j, U_j^Q) & \text{if } c_j > U_j^Q \\ d(c_j, L_j^Q) & \text{if } c_j < L_j^Q \\ 0 & \text{otherwise} \end{cases} \quad (4.9)$$

Visually, these distances are the distances between  $c_j$  outside the envelope and the vertically corresponding points on the envelope. The distances are the green bars in the figure. Equation 4.9 returns the sum of the green bars.

**Shen Lower Bound [54, 55]:** It leverages the boundary and continuity conditions to create a lower bound of DTW. It can be used to lower-bound the USDTW with slight modification. The intuition is to find the minimum possible alignment of each  $c_j$  with points in  $Q$ , subject to the local constraint  $r$  from DTW and the global constraint  $l$  from US.

We will first introduce  $\text{LB}_{\text{Shen}}$  for DTW. Given the candidate sequence  $C$  with length  $n$ , for each  $c_j$ , we create its possible reach  $q_j$  in  $Q$  under DTW as in Equation 4.10. The elements  $q_j$  form an indexed collection  $\mathbb{Q} = (q_1, q_2, \dots, q_{\min(\lfloor lm \rfloor, n)})$ .

$$q_j = (q_{\max(1, j-r)}, \dots, q_{\min(j+r, m)}) \quad (4.10)$$

We define  $\delta(x, Y) = \min_{y \in Y} d(x, y)$ . The possible minimum cost contributed by the alignment of  $c_j$  and some point in  $Q$  to the accumulated sum would be  $\delta(c_j, q_j)$ . The lower bound  $\text{LB}_{\text{Shen}}$  is defined as:

$$\text{LB}_{\text{Shen}}(Q, C) = d(c_1, q_1) + \sum_{j=2}^{n-1} \delta(c_j, q_j) + d(c_n, q_m) \quad (4.11)$$

We direct the reader to [54] for the formal proof, while an intuition of the proof is presented here. There are three items on the right-hand side of Equation 4.11. The continuity requirement ensures that each  $c_i$  is involved in at least one alignment. The first and the last items are from the boundary condition. The middle item returns the possible minimum distances contributed by each  $c_j$ 's, where  $2 \leq j \leq n-1$ . It is obvious that  $\text{LB}_{\text{Shen}}$  in Equation 4.11 is tighter when we use the first pair of points and the last pair of points instead of doing the middle summation all from  $j = 1$  to  $n$ . It is because the distance contributed by the first pair (last pair) must be greater than  $\delta(c_1, q_1)$  ( $\delta(c_n, q_n)$ ).

It is proven that it is tighter than  $\text{LB}_{\text{Keogh}}$  [54]. It is shown in Figure 4.6 visually. The black bars refer to the additional lower bound distance sum on top of  $\text{LB}_{\text{Keogh}}$ . We will give an intuitive proof here. Both  $\text{LB}_{\text{Keogh}}$  and  $\text{LB}_{\text{Shen}}$  compute the lower bounds by summing the local distance resulting from the alignment of each  $c_j$  with some points in  $Q$ , which is guaranteed to be not greater than the partial distance contributed by the real alignment, which we only know until we compute the exact distance measure. In  $\text{LB}_{\text{Keogh}}$ , if this  $c_j$  falls outside the envelope, this local distance is the vertical distance between  $c_j$  and the envelope. If  $c_j$  falls inside, this local distance would be 0. For those points outside the envelope, the local distances for  $c_j$  of  $\text{LB}_{\text{Keogh}}$  and  $\text{LB}_{\text{Shen}}$  are the same. But  $\text{LB}_{\text{Shen}}$  aims to return the

minimum possible partial distance for each  $c_j$ , even within the envelope. Hence,  $\text{LB}_{\text{Keogh}} \leq \text{LB}_{\text{Shen}}$ .

In order to compute Equation 4.11 efficiently, we first sort sequences  $q_j$  and the resulting sorted sequences are denoted as  $\tilde{q}_j$ . The sorted sequences allow us to do a binary search when we are calculating  $\delta(c_j, \tilde{q}_j)$  in contrast to  $\delta(c_j, q_j)$ . The sorting only needs to be done once because we are testing the same  $Q$  with different candidates.

It can be extended to the USDTW case [54, 55]. The possible reach now is not only defined by  $r$ , but also by the scaling factor bound  $l$ .

$$q_j = (q_{\max(1, \lceil j/l \rceil - r)}, \dots, q_{\min(\lfloor jl \rfloor + r, m)}) \quad (4.12)$$

[54] proves the following theorem to allow us to consider the lower bound between each prefix of  $C$  and  $Q$  without the scaling up of each prefix of  $C$  (i.e.,  $C(1 : k)^L$ ) and the scaling up of  $Q$  (i.e.,  $Q^L$ ).

**Theorem 8.** *For any  $\lceil m/l \rceil \leq k \leq \min(\lfloor lm \rfloor, n)$ ,  $\text{DTW}_r(Q^{\min(\lfloor lm \rfloor, n)}, C(1 : k)^{\min(\lfloor lm \rfloor, n)})$  is always lower bounded by  $\sum_{j=1}^k \delta(c_j, q_j)$ .*

Recall that USDTW calculates DTW distances between each rescaled prefix of  $C$  to the rescaled  $Q$ , and outputs the minimum DTW distance, as in Equation 4.6. The incremental nature of the lower bound frees us to calculate the lower bound of each DTW distance from scratch. This theorem allows us to first calculate the lower bound of the shortest prefix  $C(1 : \lceil m/l \rceil)$  of  $C$  and  $Q$ , and then incrementally calculate the lower bound of the longer prefix with length from  $\lceil m/l \rceil + 1$  to  $\min(\lfloor lm \rfloor, n)$  by adding on each  $\delta(c_j, q_j)$ . To note, it also means that if  $\text{LB}_{\text{Shen}}(Q, C(1 : k))$  is larger than a value, namely  $\text{bsf}$ ,  $\text{LB}_{\text{Shen}}(Q, C(1 : k'))$ , where  $k' > k$ , would also be larger than  $\text{bsf}$ . To note, we can tighten  $\text{LB}_{\text{Shen}}$  by using  $d(c_1, q_1)$  instead of  $\delta(c_1, q_1)$ .

The above analysis can also apply to the case of US distance. We only need to define the corresponding reaches as follows:

$$q_j = (q_{\max(1, \lceil j/l \rceil)}, \dots, q_{\min(\lfloor jl \rfloor, m)}) \quad (4.13)$$

## 4.4 Piecewise Scaling Distance

The motivation stems from the limitations of US and USDTW. They assume that the relationship between  $Q$  and  $C$  is governed by only a single, global scaling

factor. This assumption fails when applied to multi-rate data, where different phases of the time series express at different rates.

Note that existing studies [62, 58] can find all scaling factors, defined by the chosen prefix of  $C$ , ranging from  $\lceil m/l \rceil$  to  $\min(\lfloor lm \rfloor, n)$ . However, they can use only one of them in the scaling. Consider the following illustrative example in ASCII text [58], where character repetition represents the duration of spoken phonemes, and space indicates a pause:

- “time series 20 25” and “time series 20 25”. Here, the Hamming distance (the discrete analogue of ED) fails due to misalignment in the underlined locations, but the string edit distance (the discrete analogue of DTW) can resolve it.
- “time sseerriiss 222000222555”. This sequence exhibits three distinct phases with scaling factors of 1, 2, and 3, respectively. The corresponding invariance cannot be achieved by DTW or US (which is restricted to a single global scalar). US would enforce a single compromised global scale instead.

In Query-by-Content scenarios, such as query-by-humming or gesture retrieval, the query is generated by a human. Humans do not maintain a consistent rate for each phase. For example, humans rush through a familiar sequence but slow down for a new or complex sequence. It is commonly observed in a piece of music performed by a beginner. The piece’s tempo is not uniform.

We introduce a novel distance measure framework, termed Piecewise Scaling Distance (PSD). It addresses the local scaling effect within each phase by employing a scaling factor to each phase, instead of using a single scaling factor for the whole time series. It releases the basic constraint or assumption made in US and USDTW. PSD employs an existing distance metric, such as ED or DTW, to quantify the similarity of aligned segment pairs. While the PSD framework is agnostic to the underlying metric, this study focuses on its two fundamental instantiations:

- PSED, which employs ED to compute the similarity of aligned segment pairs.
- PSDTW, which employs DTW to compute the similarity of aligned segment pairs.

In the formulation that follows, we utilize PSDTW as the running example. PSDTW generalizes PSED. The PSED formulation can be trivially derived from it.

### 4.4.1 Piecewise Scaling & Dynamic Time Warping (PS-DTW)

**Problem formulation:** To simplify the discussion, we focus on the comparison between  $Q$  and the entire sequence  $C$ , rather than a prefix of  $C$ . Note that this formulation can be generalized to prefix matching as in Definition 6 and Definition 7.

Given two sequences  $Q$  and  $C$ , where  $Q$  is not longer than  $C$ ,  $|Q| = m \leq |C| = n$ , and the number of segments or pieces  $P$  allowed, our goal is to segmentalize both  $Q$  and  $C$  into  $P$  contiguous segments automatically in a way that minimize the total sum of DTW distance of aligned segment pairs with interpolation.

**Definition 9** (Piecewise Scaling & Dynamic Time Warping (PSDTW)). With the same notations defined in Definition 7,

$$\begin{aligned} \text{PSDTW}_r(Q, C, l, L, P) = \\ \min_{\substack{i_1 < i_2 < \dots < i_{P+1} \\ j_1 < j_2 < \dots < j_{P+1}}} \sum_{p=1}^P \text{DTW}_r(Q(i_p + 1 : i_{p+1})^L, \\ C(j_p + 1 : j_{p+1})^L) \end{aligned} \quad (4.14)$$

, where  $i_1 = 0$ ,  $i_{P+1} = m$ ,  $j_1 = 0$ ,  $j_{P+1} = n$  and the setting of  $L$  will be discussed later.

Essentially,  $L$  needs to be at least the length of all segments to preserve all the points by up-sampling.

We refer to Figure 4.3 to clarify Equation 4.14. Given two sequences  $Q$  and  $C$ , with the aid of different colors and the dashed lines, we observe that  $Q$  consists of three segments while  $C$  consists of four segments, with the first three segments of  $C$  similar to those of  $Q$ . They form three segment pairs. The scaling factor used in each segment pair is determined from the length of the two subsequences involved, i.e.,  $(i_{p+1} - i_p)/(j_{p+1} - j_p)$ . These three parts have different scaling factors. For example, the first part in  $C$  is the stretched version of that in  $Q$ . The second part in  $C$  is the compressed version of that in  $Q$ .

Equation 4.14 can be formulated in a recurrence relation as follows. Let  $D[i, j, p]$  be the minimum cost to align the first  $i$  points in  $Q$  (i.e,  $Q(1 : i)$ ) with the first  $j$  points in  $C$  (i.e.,  $C(1 : j)$ ) using exactly  $p$  segments:

---

**Algorithm 1** Naive PSDTW

---

**Input:** Query series  $Q$ , Candidate series  $C$ , DTW constraint parameter  $r$  (in fraction), Number of pieces  $P$ , Scaling parameter  $L$

**Output:** Distance Matrix  $D$  of size  $(m + 1) \times (n + 1) \times (P + 1)$

```

1: Initialize  $D$  with  $\infty$ 
2:  $D[0, 0, 0] \leftarrow 0$ 
3: for  $p \leftarrow 1$  to  $P$  do
4:   for  $i \leftarrow 1$  to  $m$  do
5:     for  $j \leftarrow 1$  to  $n$  do
6:        $D[i, j, p] \leftarrow \min_{i' < i, j' < j} \{ D[i', j', p - 1]$ 
           $+ \text{DTW}_r(Q(i' + 1 : i)^L, C(j' + 1 : j)^L) \}$ 
7: return  $D[m, n, P]$ 

```

---

**Algorithm 2** Line 6 in Algorithm 1

---

```

1: for  $i' \leftarrow 0$  to  $i - 1$  do
2:   for  $j' \leftarrow 0$  to  $j - 1$  do
3:      $dist_{\text{prev}} \leftarrow D[i', j', p - 1]$ 
4:      $dist_{\text{seg}} \leftarrow \text{DTW}_r(Q(i' + 1 : i)^L, C(j' + 1 : j)^L)$ 
5:      $D[i, j, p] \leftarrow \min(D[i, j, p], dist_{\text{prev}} + dist_{\text{seg}})$ 

```

---

$$D[i, j, p] = \min_{\substack{i' < i \\ j' < j}} \left\{ D[i', j', p - 1] + \text{DTW}_r(Q(i' + 1 : i)^L, C(j' + 1 : j)^L) \right\} \quad (4.15)$$

**Naive PSDTW:**

Our goal is  $D[m, n, P]$ . Equation 4.15 can be solved exactly by dynamic programming (DP). The base case is  $D[0, 0, 0] = 0$ . It refers to the zero cost to align the first 0 point (i.e., the empty prefix) of  $Q$  with that of  $C$ . Other cells in  $D$  are first initialized with  $\infty$ . They are calculated using a bottom-up approach via Equation 4.15. A straightforward implementation in DP is shown in Algorithm 1. Line 6 is achieved by looping all the previous indices of the current  $i$  and  $j$  as in Algorithm 2.

We explain the lines in Algorithm 2. Line 3 retrieves the accumulated distance cost from the beginning up to the endpoints  $(i', j')$ , and saves it as  $dist_{\text{prev}}$ . Line 4 considers the current aligned segment pair, which consists of  $Q(i' + 1 : i)$  and  $C(j' + 1, j)$ , and they are interpolated to the length  $L$ . The DTW distance of this pair is calculated and saved as  $dist_{\text{seg}}$ .

---

**Algorithm 3** Initialization of PSDTW

---

- 1:  $L_{\text{gmin}}^Q \leftarrow \lceil (m/P)/\sqrt{l} \rceil, L_{\text{gmax}}^Q \leftarrow \lfloor (m/P)\sqrt{l} \rfloor$  ▷ “g” refers to “global”.
  - 2:  $L_{\text{gmin}}^C \leftarrow \lceil (n/P)/\sqrt{l} \rceil, L_{\text{gmin}}^C \leftarrow \lfloor (n/P)\sqrt{l} \rfloor$
  - 3:  $L = \max(L_{\text{gmax}}^Q, L_{\text{gmin}}^C)$
  - 4: Initialize  $D$  of size  $(m+1) \times (n+1) \times (P+1)$  with  $\infty$
  - 5:  $D[0, 0, 0] \leftarrow 0$
- 

We now analyze the time complexity of Algorithm 1. There are  $Pmn$  entries in  $D$ . The  $\min$  operator in line 6 takes  $\mathcal{O}(mn)$ . Hence, the time complexity of Algorithm 1 is  $\mathcal{O}(Pm^2n^2) = \mathcal{O}(Pn^4)$ , multiplied by the running time of the DTW. It is slow, which prevents us from using it in practice. To note, we use  $r$  in a fraction instead of a fixed integer here. This allows the deviation tolerance to scale adaptively with pieces of varying lengths.

#### 4.4.2 Speedup Techniques

**Length constraints of the segment:** A way to reduce complexity and to prevent pathological segment pairs is to limit the possible segment lengths that are considered by constraining the minimum and maximum lengths of segments. It is similar to constrained DTW, in which we limit the search space of the warping path as in Figure 4.5. The version of PSDTW that considers the segment constraint is termed constrained PSDTW (cPSDTW). It is shown in Algorithm 4. The uncolored part shows the main logic, while the colored part shows the speedup techniques, which will be explained later.

We initialize in Algorithm 3. For a given number of segments  $P$ , the expected length of each segment in  $Q$  and  $C$  would be  $m/P$  and  $n/P$ , respectively. For  $Q$ , we set the minimum possible segment length  $L_{\text{gmin}}^Q$  to be  $\lceil (m/P)/\sqrt{l} \rceil$  and the maximum possible length  $L_{\text{gmax}}^Q$  to be  $\lfloor (m/P)\sqrt{l} \rfloor$  in line 1 such that the scaling ratio of any two segments in  $Q$  would be bounded by  $l$ . It allows some deviation in the length of the segments from their expected length. Similarly, we compute the segment constraints for  $C$  in line 2. We set the maximum segment length be the alignment factor  $L$  in line 3. We set the base case in line 5.

We fill the table  $D$  in Algorithm 4. In line 3, given  $p$  pieces in  $Q$ , the ending index of the last piece (i.e., the  $p^{\text{th}}$  piece) will range from  $(p \cdot L_{\text{gmin}}^Q)$ , given all the  $p$  pieces are in minimum length  $L_{\text{gmin}}^Q$ , to  $\min(p \cdot L_{\text{gmax}}^Q, m)$ , given all the  $p$  pieces are in maximum length  $L_{\text{gmax}}^Q$ .

In line 4, we enumerate for all the allowed lengths  $L^Q$ . For the segment with length  $L^Q$  in  $Q$ , the length  $L^C$  of the corresponding aligned segment in  $C$  will

**Algorithm 4** Constrained PSDTW (cPSDTW) with early abandoning and lower bounding

**Input:** Query series  $Q$ , Candidate series  $C$ , DTW constraint parameter  $r$  (in fraction), Number of pieces  $P$ , best\_so\_far bsf

**Output:** The final distance  $D[m, n, P]$  if  $D[m, n, P] \leq \text{bsf}$ , otherwise  $\infty$

- ```

1: Execute Algorithm 3 for initialization
2: for  $p \leftarrow 1$  to  $P$  do
3:   for  $i \leftarrow (p \cdot L_{\text{gmin}}^Q)$  to  $\min(p \cdot L_{\text{gmax}}^Q, m)$  do            $\triangleright$  The iterations can be parallelized.
4:     for  $L^Q \leftarrow L_{\text{gmin}}^Q$  to  $L_{\text{gmax}}^Q$  do
5:        $i' \leftarrow i - L^Q$                                  $\triangleright i'$ : End point of previous segment on  $Q$ .
6:        $Q' \leftarrow \text{rev}(Q(i'+1 : i))$                    $\triangleright \text{rev}(T)$ : Reverse the input series  $T$ .
7:        $L_{\text{min}}^C \leftarrow \max(L_{\text{gmin}}^C, \lceil L^Q/l \rceil)$ 
8:        $L_{\text{max}}^C \leftarrow \min(\lfloor L^Q/l \rfloor, L_{\text{gmax}}^C)$ 
9:        $r' \leftarrow r \times \max(L^Q, L_{\text{max}}^C)$            $\triangleright$  Compute the integer value of  $r$ .
10:      for  $k \leftarrow 1$  to  $L_{\text{max}}^C$  do
11:         $\mathbb{Q}_k \leftarrow (q'_{\max(1, \lceil k/l \rceil - r')}, \dots, q'_{\min(\lfloor k/l \rfloor + r', L^Q)})$   $\triangleright$  Construct indexed collection  $\mathbb{Q}$ .
12:         $\tilde{\mathbb{Q}}_k \leftarrow \text{sort}(\mathbb{Q}_k)$ 
13:        for  $j \leftarrow (p \cdot L_{\text{gmin}}^C)$  to  $\min(p \cdot L_{\text{gmax}}^C, n)$  do
14:          for  $L^C \leftarrow L_{\text{min}}^C$  to  $L_{\text{max}}^C$  do
15:             $j' \leftarrow j - L^Q$ 
16:             $C' \leftarrow \text{rev}(C(j'+1 : j))$ 
17:             $dist_{\text{prev}} \leftarrow D[i', j', p-1]$ 
18:            if  $dist_{\text{prev}} = \infty$  then
19:              continue
20:            if  $dist_{\text{prev}} > \text{bsf}$  then
21:              continue
22:            if  $dist_{\text{prev}} > D[i, j, p]$  then            $\triangleright D[i, j, p]$  stores the best so far.
23:              continue
24:            if  $L^C = L_{\text{min}}^C$  then            $\triangleright$  Compute the lower bound from sketch.
25:               $lb = (c'_1 - q'_1)^2$   $\triangleright$  Partial distance contributed by the first alignment.
26:              for  $k \leftarrow 2$  to  $L^C$  do
27:                 $lb = lb + \delta(c'_k, \tilde{\mathbb{Q}}_k)$ 
28:              else
29:                 $lb = lb + \delta(c'_{L^C}, \tilde{\mathbb{Q}}_{L^C})$      $\triangleright$  Compute the lower bound incrementally.
30:                 $lb_{\text{check}} = lb - \delta(c'_{L^C}, \tilde{\mathbb{Q}}_{L^C}) + (c'_{-1} - q'_{-1})^2$      $\triangleright$  Tighten the lower bound
by using the last alignment.
31:                if  $dist_{\text{prev}} + lb_{\text{check}} > D[i, j, p]$  then
32:                  continue
33:                   $dist_{\text{seg}} \leftarrow \text{DTW}_r(Q'^L, C'^L)$ 
34:                  if  $dist_{\text{prev}} + dist_{\text{seg}} < D[i, j, p]$  then
35:                     $D[i, j, p] \leftarrow dist_{\text{prev}} + dist_{\text{seg}}$   $\triangleright$  Also save pointer  $(i', j')$  for the cut.
36: return  $D[m, n, P]$ 

```

have a range from  $L_{\min}^C$  to  $L_{\max}^C$ , as defined in lines 7–8, such that the ratio of  $L^Q$  and  $L^C$  would be bounded by  $l$ . Because  $L^Q$  and  $L^C$  increase in line 4 and line 14, and the  $i$  and  $j$  are fixed by the outer loop, in line 3 and line 13, respectively, the  $i'$  and  $j'$  decrease correspondingly. It is visualized in Figure 4.7. A segment in  $Q$  with ending index  $i$  and starting index  $i' + 1$  would be compared to a set of segments in  $C$ , all of which have a fixed end at  $j$  and a decreasing starting index,

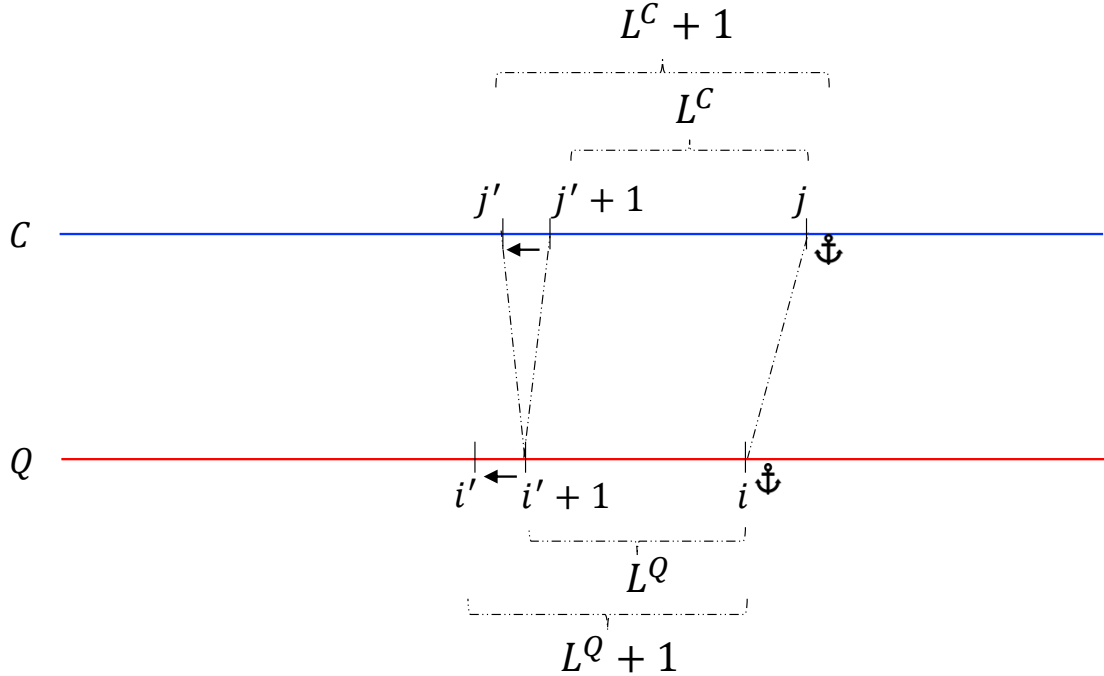


Figure 4.7: Relationship of  $L_Q$  and  $L_C$ .

starting at  $j' + 1$ . For example, the starting index of the first segment with being compared is  $j' + 1$ , which has length  $L^C$ , and that of the second segment is  $j'$ , which has length  $L^C + 1$ , as in Figure 4.7.

In line 18, we terminate the current iteration if there are no previously valid segment pairs (i.e.,  $dist_{prev} = \infty$ ).

In line 22, if the accumulated cost  $dist_{prev}$  exceeds the current best so far, we stop the current iteration as the resulting  $(dist_{prev} + dist_{seg})$  is guaranteed to be greater than the current best so far, which is stored in  $D[i, j, p]$ .

To be consistent with the result of using the lower bound speedup technique, which will be introduced later, we compute the DTW in the reverse manner in line 33. Due to the nearest neighbor interpolation,  $DTW_r(Q^L, C^L)$  may not equal to  $DTW_r(\text{rev}(Q')^L, \text{rev}(C')^L)$ .

In line 35, we also save the pairs  $(i', j')$  that serve as cutting points between segments to obtain the segmentation result.

**Parallel computing:** We observe that the recurrence relation for the state  $D[i, j, p]$  at stage  $p$  depends exclusively on the states computed at stage  $p - 1$ , as shown in Equation 4.15. There are no stage dependencies over indices  $i$  and  $j$ . It allows us to parallelize the loops over indices  $i$  and  $j$  on lines 3 and 13. In the following experimental section, we distribute the i-loop iterations (i.e., line 3 in

Algorithm 4, which is colored in blue) across available threads only because there are already sufficient iterations from the i-loop to fill the available threads. There are  $\left(\min(p \cdot L_{\text{gmax}}^Q, m) - (p \cdot L_{\text{gmin}}^Q) + 1\right)$  iterations from the i-loop. The parallel execution of the *i*-loop is implemented by `prange` in Numba in Python.

**Early Abandoning in nearest neighbor search:** To accelerate the nearest neighbor search (or top- $k$  search) for a query  $Q$  on a candidate set, we employ an early abandoning strategy. It prunes the search branch within the PSD computation of a specific candidate  $C$  as soon as the result corresponding to this search branch is determined to be suboptimal. We maintain a variable,  $\text{bsf}$  (best-so-far), which represents the minimum final distance among the candidates processed with  $Q$  so far.  $\text{bsf}$  serves as an upper-bound threshold. During the evaluation of a new candidate  $C$ , we monitor the accumulated partial distance,  $\text{dist}_{\text{prev}}$ . If  $\text{dist}_{\text{prev}}$  exceeds  $\text{bsf}$ , the corresponding final distance is guaranteed to exceed  $\text{bsf}$ . In such cases, the current search branch is immediately terminated. The implementation of this pruning mechanism is detailed in lines 20–21 in Algorithm 4, which are colored in orange. In the case of top- $k$  search, we must maintain the top- $k$  final distances and use the  $k$ -th distance as the threshold.

#### Lower bound:

When we use DTW as a routine in PSD, the computation of the DTW of the interpolated segment can be sped up by computing  $\text{LB}_{\text{Shen}}$  for the lower bound. From Figure 4.7, we observe that a segment of  $Q$ , with length  $L^Q$ , is compared to a set of growing segments of  $C$ , with a fixed end at  $j$ . The length of these segments is from  $L_{\text{min}}^C$  to  $L_{\text{max}}^C$ , as indicated in line 14 in Algorithm 4. They share the same suffix with length  $L_{\text{min}}^C$ . It encourages us to view both  $Q$  and  $C$  reversely. The reversed segments are denoted as  $Q'$  and  $C'$ , as in lines 6 and 16 in Algorithm 4. In this reversed view, they share the same prefix with length  $L_{\text{min}}^C$ . Hence, we construct an indexed collection  $\tilde{\mathbb{Q}}$  for  $Q'$  with the maximum length of the segments being compared in  $C$ , which is  $L_{\text{max}}^C$ , as in lines 10–12.

In lines 24–27, we first compute the lower bound between  $Q'$  and the shortest segment of  $C$ . We add the minimum possible contribution of each  $c'$  to the distance contributed by the first alignment, which is  $lb = (c'_1 - q'_1)$ . For the lower bound of the subsequent segments, we compute them incrementally in line 29. Because the last point of segment  $C'$  must map to the last point of  $Q'$ , we further tighten the lower bound by using the last alignment in line 30 instead.

Furthermore, we can reduce the computational overhead of constructing the sorted reaches  $\tilde{q}_k$  (lines 9–12). As illustrated in Figure 4.7, the segment of  $Q$  involved in the comparison grows incrementally. Since the reversed versions of these

---

**Algorithm 5** Replace lines 3 to 9 in Algorithm 5 to reuse the computed sorted reaches  $\tilde{q}_k$ .

---

```

1:  $r'_{\text{cache}} \leftarrow -1$ 
2: for  $i \leftarrow (p \cdot L_{\text{gmin}}^Q)$  to  $\min(p \cdot L_{\text{gmax}}^Q, m)$  do
3:   for  $L^Q \leftarrow L_{\text{gmin}}^Q$  to  $L_{\text{gmax}}^Q$  do
4:      $i' \leftarrow i - L^Q$ 
5:      $Q' \leftarrow \text{rev}(Q(i' + 1 : i))$ 
6:      $L_{\text{min}}^C \leftarrow \max(L_{\text{gmin}}^C, \lceil L^Q/l \rceil)$ 
7:      $L_{\text{max}}^C \leftarrow \min(\lfloor L^Q/l \rfloor, L_{\text{gmax}}^C)$ 
8:      $r' \leftarrow r \times \max(L^Q, L_{\text{max}}^C)$ 
9:     if  $r'_{\text{cache}} = r'$  then
10:    for  $k \leftarrow 1$  to  $L_{\text{max}}^C$  do
11:      if  $k \leq |Q'|$  then
12:         $e_{\text{prev}} \leftarrow \min(\lfloor kl \rfloor + r', L^Q - 1)$ 
13:         $e_{\text{new}} \leftarrow \min(\lfloor kl \rfloor + r', L^Q)$ 
14:        if  $e_{\text{new}} > e_{\text{prev}}$  then
15:           $\tilde{q}_k \leftarrow \tilde{q}_k \cup q'_{e_{\text{new}}}$ 
16:        else
17:           $q_k \leftarrow (q'_{\max(1, \lceil k/l \rceil - r')}, \dots, q'_{\min(\lfloor kl \rfloor + r', L^Q)})$   $\triangleright L^Q$  equals to  $|Q'|$ .
18:           $\tilde{q}_k \leftarrow \text{sort}(q_k)$ 
19:        else
20:          for  $k \leftarrow 1$  to  $L_{\text{max}}^C$  do
21:             $q_k \leftarrow (q'_{\max(1, \lceil k/l \rceil - r')}, \dots, q'_{\min(\lfloor kl \rfloor + r', L^Q)})$ 
22:             $\tilde{q}_k \leftarrow \text{sort}(q_k)$ 
23:           $r_{\text{cache}} \leftarrow r'$ 

```

---

segments share a common prefix, the sorted reaches  $\tilde{q}_k$  computed for a segment  $Q'$  of length  $L^Q$  can be reused to compute those for the subsequent segments. This optimization is detailed in Algorithm 5, with the new components highlighted in blue. It is important to note that because  $r'$  is a function of  $L^Q$ , and the construction of  $\tilde{q}_k$  depends on  $r$ , reuse is limited to cases where  $r'$  remains constant. We construct reaches  $q_k$  from the sketch in lines 20–22 and keep track of the  $r'$  used for construction in line 23. If  $r'$  remains constant, we can use previously computed reaches  $\tilde{q}_k$  to compute the new set of reaches  $\tilde{q}_k$ . Since the ending index of reaches depends on  $\min(\lfloor kl \rfloor + r', L^Q)$ , we need to check whether we have a new ending index when  $L^Q$  increases. If the ending index has been changed, we need to add the new data points  $q'_{e_{\text{new}}}$  to the sorted sequence  $\tilde{q}_k$ , as in line 15.

$L_{\text{max}}^C$  depends of  $L^Q$ . If  $L_{\text{max}}^C$  increase because  $L^Q$  increase, we construct the new reach  $\tilde{q}_k$  and sort it in lines 16–18.

### 4.4.3 Guided Distance

For faster computation, one would want to use a distance measure with linear complexity, such as ED, as the base measure for PSD. While PSED is effective for identifying phase-scaling changes, certain applications require capturing complex properties within those segments that ED cannot handle. There are two ways to address it. One approach is to use an alternative distance measure that captures these complex properties as the base distance for computing the PSD, such as DTW. But PSDTW is slower than PSED. The other approach is to use the segmentation result returned by PSED. To address this, we propose a two-stage framework in which PSED-derived segmentation guides the application of advanced distance metrics  $M$ . Let  $\mathcal{P}^* = \{(i_1, j_1), (i_2, j_2), \dots, (i_{P+1}, j_{P+1})\}$  be the set of optimal cut points on  $Q$  and  $C$  obtained by minimizing the PSED. We utilize  $\mathcal{P}^*$  to partition both series into  $P$  aligned pairs of segments. The final distance, denoted as  $M^{\text{PSED}}$ , is calculated by summing the distances of these pairs using a target metric  $M$ :

$$M^{\text{PSED}}(Q, C) = \sum_{p=1}^P M(Q_p^L, C_p^L) \quad (4.16)$$

, where  $Q_p = Q(i_p + 1 : i_{p+1})$  and  $C_p = C(j_p + 1 : j_{p+1})$ .

## 4.5 Experiments

We evaluate the performance of our proposed distance measure framework, PSD, via its two instantiations: PSED and PSDTW. Specifically, we focus on a query retrieval task in which the query exhibits piecewise-scaled distortion, that is, distinct phases of the query exhibit different expression rates relative to the target in the candidate dataset. Our objective is to verify whether PSD achieves invariance to these multiple scaling distortions, thereby allowing it to correctly retrieve the most similar candidate. We detail the experimental setup in Section 4.5.1 and present the results in Section 4.5.2. The code and data are available at <https://github.com/colemanyu/k-scaling-factor-dtw>.

### 4.5.1 Experimental Setup

We utilize the GunPoint dataset, originally released in 2003 [69], as the running example. Widely regarded as the “iris” dataset of the time series community [70],

it has appeared in over one thousand publications. Beyond its ubiquity, the dataset addresses a critical distinction: misinterpreting the act of aiming a gun as merely pointing a finger could have life-threatening consequences.

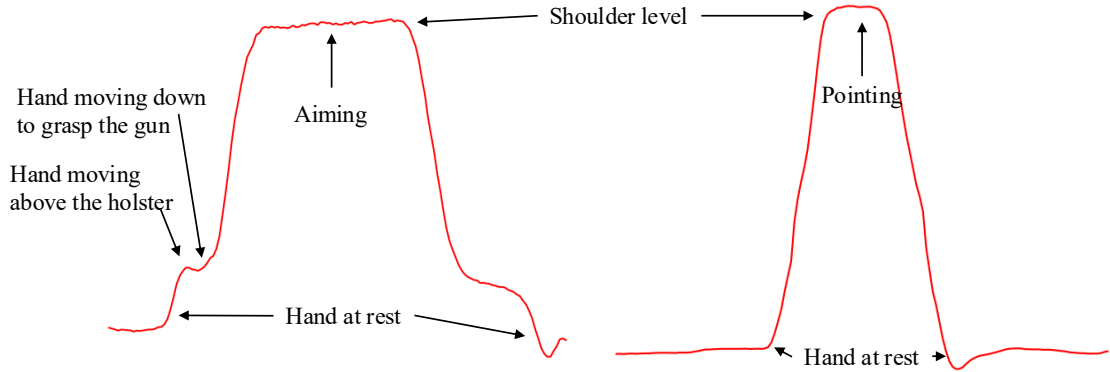


Figure 4.8: Visualization of the GunPoint dataset. Left (Right): A time series of the “Gun” (“Point”) scenario. Critical periods, such as “Aiming”, are annotated.

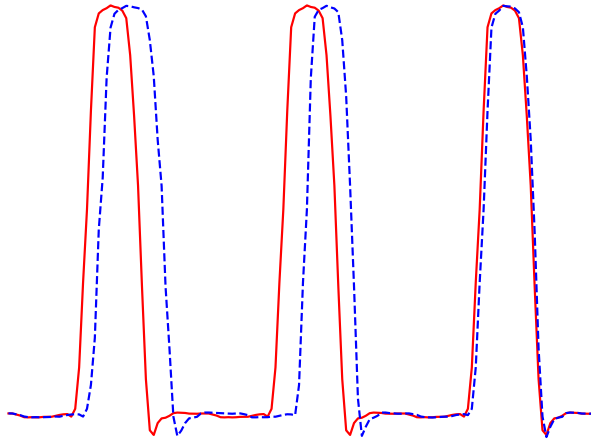


Figure 4.9: The red solid time series shows an instant in the target set. The blue dashed time series shows an instant in the query set.

The dataset contains two classes: “Gun” and Point”. Actors aim at an eye-level target using either a replica gun or their index finger, as illustrated in Figure 4.8. The resulting time series represent the X-axis centroid of the actor’s right hand. Each action lasts for 5 seconds, with the pointing/aiming phase occurring for approximately one second. Recorded at 30 fps, each sample consists of 150 data points. The dataset comprises 50 training and 150 test series, all of length 150.

A key limitation of the original dataset is the assumption that every action lasts exactly 5 seconds. In reality, actors perform actions at varying speeds. If an

actor is asked to perform the action three times continuously in a row, we are likely to observe a time series containing three phases, each with a unique rate. The first phase should take longer than subsequent phases because it is the first time the action is performed. This phenomenon is depicted in Figure 4.9, where the red curve represents an ideal case that consists of three identical phases (i.e., identical rate), while the blue curve represents a realistic scenario with varying rates. The first action is slower than the second action. Consequently, retrieving such patterns requires assigning different scaling factors to each phase to accommodate the phase-specific rates.

We now describe the procedure for generating the target and query sets for the retrieval task. To construct the target set, we concatenate  $P$  repetitions of each time series instance from the source dataset. To ensure a fair comparison, we constrain the resulting time series to match the original length  $n$ . This is achieved by rescaling each phase to a length of  $n/P$  prior to concatenation. Note that we must handle remainders to ensure that the final time series length is exactly  $n$ . An example of such a target (where  $P = 3$ ) is depicted by the red solid line in Figure 4.9.

To construct the query set, we first determine the specific lengths for the  $P$  segments. Starting with an expected mean length of  $n/P$ , we define the minimum segment length as  $L_{\min} = (n/P)\sqrt{l}$  and the maximum as  $L_{\max} = (n/P)\sqrt{l}$ . This formulation ensures that the ratio of the lengths of any two segments is bounded by  $l$ . We then generate  $P$  random integers within  $[L_{\min}, L_{\max}]$  subject to the constraint that their sum is exactly  $n$ . Finally, we construct the query by rescaling  $P$  copies of the source time series to these generated random lengths and concatenating them. The resulting time series maintains the original length  $n$ . An example of such a query (where  $P = 3$ ) is depicted by the blue dashed line in Figure 4.9.

Both the query and target sets are derived from the same source dataset. Consequently, the ground truth target for a given query is defined as the instance in the target set that is generated from the same underlying source time series.

Table 4.1 details the additional datasets used in this study. The column labeled “Train/Test?” specifies which split was employed as the source dataset.

In our experiments, we set the warping window parameter  $r = 0.1$ , as suggested in the literature. The algorithms were implemented in Python. We utilized the `aeon` [71] library to obtain the baseline distance measures. All experiments were conducted on a workstation equipped with an Intel Xeon Gold 6326 CPU and 256GB of RAM.

Table 4.1: Details of the ten datasets for the experiments

| Name                  | Type      | Train/Test? | Size | Class | Length |
|-----------------------|-----------|-------------|------|-------|--------|
| SonyAIBORobotSurface1 | Sensor    | Test        | 601  | 2     | 70     |
| ECG200                | ECG       | Train       | 100  | 2     | 96     |
| MedicalImages         | Image     | Train       | 381  | 10    | 99     |
| CBF                   | Simulated | Train       | 30   | 3     | 128    |
| SwedishLeaf           | HAR       | Train       | 500  | 15    | 128    |
| Plane                 | Sensor    | Train       | 105  | 7     | 144    |
| PowerCons             | Device    | Train       | 180  | 2     | 144    |
| GunPoint              | HAR       | Train       | 50   | 2     | 150    |
| Adiac                 | Image     | Train       | 390  | 37    | 176    |
| Epilepsy              | HAR       | Train       | 137  | 4     | 207    |

### 4.5.2 Experimental Results

We employ Top- $k$  Accuracy (often referred to as Precision@ $k$  [72]) as the primary evaluation metric. For a single query  $Q$ , this metric indicates whether the correct match is successfully retrieved within the top  $k$  candidates:

$$P@k(Q) = \begin{cases} 1 & \text{if the ground truth is in the top-}k \text{ results} \\ 0 & \text{otherwise} \end{cases} \quad (4.17)$$

To determine the top- $k$  results, we compute the distance between  $Q$  and every time series in the target set, generating a distance profile of length equal to the dataset size. The top- $k$  results correspond to the  $k$  instances with the smallest distances in this profile. Finally, we evaluate the overall performance by computing the mean Top- $k$  Accuracy across the entire query set  $\mathcal{D}$ :

$$\overline{P@k} = \frac{\sum_{Q \in \mathcal{D}} P@k(Q)}{|\mathcal{D}|} \quad (4.18)$$

We choose  $k \in \{1, 3\}$ .  $k = 1$  refers to the exact retrieval.  $k = 3$  give some tolerance for the retrieval.

**Results of GunPoint dataset:** We utilize the GunPoint dataset to evaluate how the parameters  $P$  and  $l$  affect the ability of PSD to achieve invariance under piecewise scaling. The results are presented in Table 4.2, where the best performance of  $\overline{P@1}$  is highlighted in bold, and the second-best is underlined. We benchmark our method against several state-of-the-art distance measures, including ADTW [10], DDTW [4], shapeDTW [6], WDDTW [5], and WDTW [5]., PSED

Table 4.2: The accuracy comparison for eight distance measures of the GunPoint dataset

| $P$ | $l$  | ED    |       | DTW [3]     |       | ADTW [10] |       | DDTW [4] |       | shapeDTW [6] |       | WDDTW [5] |       | WDTW [5]    |       | PSED        |       | PSDTW       |       |
|-----|------|-------|-------|-------------|-------|-----------|-------|----------|-------|--------------|-------|-----------|-------|-------------|-------|-------------|-------|-------------|-------|
|     |      | $P@1$ | $P@3$ | $P@1$       | $P@3$ | $P@1$     | $P@3$ | $P@1$    | $P@3$ | $P@1$        | $P@3$ | $P@1$     | $P@3$ | $P@1$       | $P@3$ | $P@1$       | $P@3$ | $P@1$       | $P@3$ |
| 2   | 1.25 | 0.30  | 0.56  | 0.82        | 1.00  | 0.54      | 0.84  | 0.84     | 0.92  | <u>0.96</u>  | 1.00  | 0.88      | 0.96  | 0.82        | 0.98  | <b>0.98</b> | 1.00  | 0.86        | 1.00  |
|     | 1.50 | 0.14  | 0.36  | 0.88        | 1.00  | 0.38      | 0.64  | 0.78     | 0.94  | <b>1.00</b>  | 1.00  | 0.80      | 0.92  | 0.88        | 0.96  | <b>1.00</b> | 1.00  | <u>0.96</u> | 1.00  |
|     | 1.75 | 0.16  | 0.34  | 0.82        | 1.00  | 0.38      | 0.66  | 0.64     | 0.80  | 0.90         | 1.00  | 0.66      | 0.80  | 0.82        | 0.96  | <b>1.00</b> | 1.00  | <u>0.94</u> | 1.00  |
|     | 2.00 | 0.12  | 0.24  | 0.84        | 0.98  | 0.34      | 0.66  | 0.72     | 0.88  | <u>0.96</u>  | 1.00  | 0.68      | 0.86  | 0.82        | 0.98  | <b>1.00</b> | 1.00  | <u>0.96</u> | 1.00  |
| 3   | 1.25 | 0.30  | 0.50  | 0.84        | 0.92  | 0.70      | 0.88  | 0.80     | 0.92  | <b>0.96</b>  | 0.98  | 0.84      | 0.94  | 0.86        | 0.98  | <u>0.94</u> | 1.00  | 0.88        | 0.96  |
|     | 1.50 | 0.10  | 0.28  | 0.84        | 0.96  | 0.60      | 0.78  | 0.66     | 0.86  | <u>0.90</u>  | 1.00  | 0.72      | 0.86  | 0.84        | 0.98  | <b>0.96</b> | 1.00  | 0.86        | 0.96  |
|     | 1.75 | 0.10  | 0.28  | <u>0.88</u> | 1.00  | 0.42      | 0.78  | 0.72     | 0.88  | 0.76         | 0.94  | 0.74      | 0.88  | <u>0.88</u> | 1.00  | <b>1.00</b> | 1.00  | <u>0.88</u> | 0.98  |
|     | 2.00 | 0.02  | 0.12  | <u>0.86</u> | 0.94  | 0.38      | 0.52  | 0.60     | 0.78  | 0.70         | 0.94  | 0.60      | 0.80  | 0.82        | 0.92  | <b>0.98</b> | 1.00  | <u>0.86</u> | 0.98  |
| 4   | 1.25 | 0.34  | 0.50  | 0.70        | 0.86  | 0.68      | 0.88  | 0.60     | 0.78  | 0.70         | 0.90  | 0.64      | 0.80  | 0.70        | 0.86  | <b>0.86</b> | 0.94  | <u>0.72</u> | 0.88  |
|     | 1.50 | 0.22  | 0.38  | 0.64        | 0.80  | 0.60      | 0.92  | 0.52     | 0.64  | 0.68         | 0.90  | 0.52      | 0.66  | 0.64        | 0.82  | <b>0.86</b> | 0.98  | <u>0.72</u> | 0.82  |
|     | 1.75 | 0.16  | 0.30  | 0.72        | 0.92  | 0.56      | 0.80  | 0.60     | 0.78  | 0.56         | 0.80  | 0.56      | 0.80  | 0.70        | 0.88  | <b>0.92</b> | 1.00  | <u>0.80</u> | 0.94  |
|     | 2.00 | 0.06  | 0.12  | 0.58        | 0.78  | 0.50      | 0.72  | 0.46     | 0.64  | 0.50         | 0.82  | 0.50      | 0.64  | 0.56        | 0.82  | <b>0.88</b> | 0.98  | <u>0.64</u> | 0.88  |

achieves the highest accuracy, followed closely by PSDTW. We attribute PSED’s superior performance over PSDTW to the specific nature of the distortions in the query set, that is, the “pure” piecewise scaling distortions. Since the query set exhibits only piecewise scaling distortions, the corresponding segments of the query and target time series differ solely in length (scale). Consequently, the additional flexibility provided by DTW in PSDTW is unnecessary and may inadvertently increase the similarity of incorrect matches, thereby reducing discriminative power relative to the stricter PSED measure. However, PSDTW remains theoretically essential for handling local distortions within the phase. PSDTW applies DTW within the scaled segment, enabling robust alignment across local nonlinearities.

Table 4.3: The accuracy comparison for six PSED-guided distance measures of the GunPoint dataset

| $P$ | $l$  | DTW <sup>PSED</sup> |       | ADTW <sup>PSED</sup> |       | DDTW <sup>PSED</sup> |       | shapeDTW <sup>PSED</sup> |       | WDDTW <sup>PSED</sup> |       | WDTW <sup>PSED</sup> |       |
|-----|------|---------------------|-------|----------------------|-------|----------------------|-------|--------------------------|-------|-----------------------|-------|----------------------|-------|
|     |      | $P@1$               | $P@3$ | $P@1$                | $P@3$ | $P@1$                | $P@3$ | $P@1$                    | $P@3$ | $P@1$                 | $P@3$ | $P@1$                | $P@3$ |
| 2   | 1.25 | 0.86                | 1.00  | 0.98                 | 1.00  | <b>0.72</b>          | 0.92  | 0.98                     | 1.00  | <b>0.74</b>           | 0.96  | 0.86                 | 1.00  |
|     | 1.50 | 0.88                | 1.00  | 1.00                 | 1.00  | <b>0.60</b>          | 0.90  | <b>0.98</b>              | 1.00  | <b>0.64</b>           | 0.90  | 0.92                 | 1.00  |
|     | 1.75 | 0.94                | 1.00  | 1.00                 | 1.00  | 0.84                 | 0.94  | 1.00                     | 1.00  | 0.86                  | 0.96  | 0.94                 | 1.00  |
|     | 2.00 | 0.98                | 1.00  | 1.00                 | 1.00  | <b>0.60</b>          | 0.78  | 0.98                     | 1.00  | <b>0.66</b>           | 0.80  | 0.98                 | 1.00  |
| 3   | 1.25 | <b>0.82</b>         | 0.96  | 0.94                 | 1.00  | <b>0.74</b>          | 0.90  | <b>0.92</b>              | 0.98  | <b>0.76</b>           | 0.90  | <b>0.82</b>          | 0.96  |
|     | 1.50 | 0.86                | 1.00  | 0.96                 | 1.00  | 0.72                 | 0.90  | 0.94                     | 1.00  | 0.80                  | 0.90  | 0.88                 | 1.00  |
|     | 1.75 | 0.88                | 1.00  | 1.00                 | 1.00  | <b>0.68</b>          | 0.90  | 1.00                     | 1.00  | <b>0.70</b>           | 0.94  | 0.90                 | 1.00  |
|     | 2.00 | 0.86                | 0.96  | 0.98                 | 1.00  | <b>0.54</b>          | 0.86  | 0.96                     | 1.00  | 0.62                  | 0.86  | 0.88                 | 0.96  |
| 4   | 1.25 | 0.74                | 0.88  | 0.86                 | 0.94  | 0.78                 | 0.80  | 0.80                     | 0.92  | 0.78                  | 0.82  | 0.74                 | 0.88  |
|     | 1.50 | 0.72                | 0.84  | 0.86                 | 0.98  | 0.68                 | 0.84  | 0.84                     | 0.96  | 0.66                  | 0.84  | 0.72                 | 0.86  |
|     | 1.75 | 0.74                | 0.96  | 0.92                 | 1.00  | <b>0.54</b>          | 0.90  | 0.90                     | 1.00  | 0.56                  | 0.88  | 0.74                 | 0.96  |
|     | 2.00 | 0.66                | 0.90  | 0.88                 | 0.98  | 0.58                 | 0.82  | 0.88                     | 0.98  | 0.62                  | 0.80  | 0.66                 | 0.90  |

We further investigate whether the segmentation results returned by PSED can serve as a guide to enhance other distance measures. As shown in Table 4.3, this approach generally improves accuracy. The exceptions are highlighted in bold,

indicating cases where the segmentation led to worse performance. Notably, in most cases, only DDTW and WDDTW failed to benefit from PSED-guided segmentation. We argue that the performance degradation of DDTW and WDDTW stems from their derivative-based nature. They rely on matching slope or shape features. Consequently, they are highly sensitive to segmentation boundaries. A non-perfect cut that falls within a shape feature segmentize it, and these features are then destroyed. When the algorithm subsequently attempts to map these features, it fails to find correct correspondences, resulting in high distances.

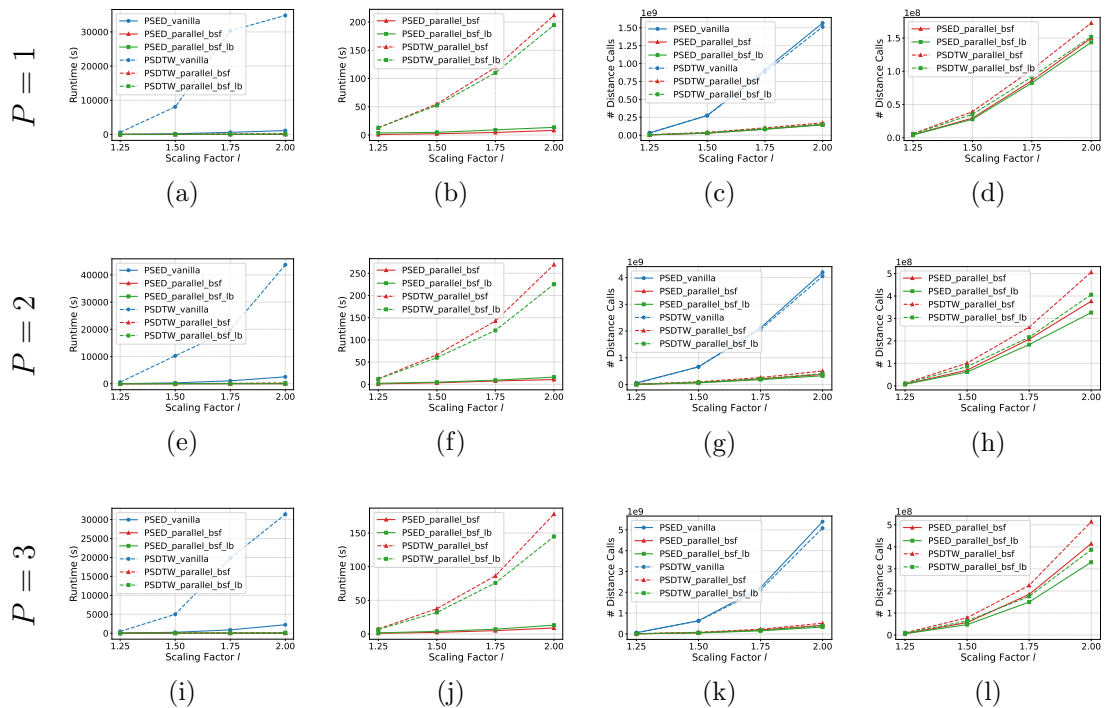


Figure 4.10: Runtime and number of distance calls comparison of GunPoint dataset. (a)-(d)  $P = 1$ , (e)-(h)  $P = 2$ , (i)-(l)  $P = 3$ .

Figure 4.10 illustrates the runtime performance across varying parameters  $P$  and  $l$ . We evaluate two variants of PSD, PSED and PSDTW, each implemented with three levels of

1. **vanilla** (i.e., Basic implementation)
2. **parallel\_bsf** (i.e., With parallelization with Best-So-Far early abandoning)
3. **parallel\_bsf\_lb** (i.e., Incorporating lower bound pruning)

This yields a total of six methods. The figure is organized into four columns plotted against the scaling factor  $l$ . The rows refer to the number of pieces  $P$ .

The first and third columns display the running time and the number of distance calculations, respectively, for all six methods. To better visualize the performance differences among the efficient implementations, the second and fourth columns omit the `vanilla` baselines and focus exclusively on the four optimized variants.

The results indicate that `vanilla_PSDTW` is orders of magnitude slower than the other approaches, whereas the optimized methods operate within a similar performance range. As anticipated, the computation time for all methods increases with the scaling factor  $l$ . The fourth column confirms that the lower bounding strategy effectively reduces the number of distance calculations (pruning power). However, the second column reveals a critical trade-off in actual runtime. While the lower bound successfully accelerates PSDTW, it actually slows down PSED. This suggests that for the computationally lighter ED, the overhead of calculating the lower bound outweighs the time saved by pruning. Overall, the results demonstrate that PSED is significantly faster than PSDTW.

### Results of the ten datasets:

Table 4.4: The accuracy comparison for eight distance measures of the ten datasets

| Dataset               | ED    |       | DTW         |       | ADTW        |       | DDTW  |       | shapeDTW |       | WDDTW |       | WDTW        |       | PSED        |       |
|-----------------------|-------|-------|-------------|-------|-------------|-------|-------|-------|----------|-------|-------|-------|-------------|-------|-------------|-------|
|                       | $P@1$ | $P@3$ | $P@1$       | $P@3$ | $P@1$       | $P@3$ | $P@1$ | $P@3$ | $P@1$    | $P@3$ | $P@1$ | $P@3$ | $P@1$       | $P@3$ | $P@1$       | $P@3$ |
| SonyAIBORobotSurface1 | 0.04  | 0.08  | 0.51        | 0.63  | 0.60        | 0.74  | 0.45  | 0.57  | 0.20     | 0.29  | 0.45  | 0.58  | 0.51        | 0.64  | <b>0.67</b> | 0.77  |
| ECG200                | 0.12  | 0.20  | 0.70        | 0.81  | 0.78        | 0.83  | 0.60  | 0.74  | 0.59     | 0.76  | 0.59  | 0.73  | 0.70        | 0.80  | <b>0.81</b> | 0.88  |
| MedicalImages         | 0.08  | 0.19  | 0.63        | 0.78  | 0.69        | 0.85  | 0.52  | 0.68  | 0.57     | 0.75  | 0.51  | 0.68  | 0.62        | 0.78  | <b>0.76</b> | 0.88  |
| CBF                   | 0.53  | 0.67  | 0.83        | 1.00  | 0.90        | 1.00  | 0.73  | 0.87  | 0.73     | 0.90  | 0.77  | 0.90  | 0.90        | 1.00  | <b>1.00</b> | 1.00  |
| SwedishLeaf           | 0.07  | 0.12  | 0.82        | 0.92  | 0.84        | 0.93  | 0.70  | 0.83  | 0.78     | 0.91  | 0.69  | 0.83  | 0.83        | 0.92  | <b>0.97</b> | 0.99  |
| Plane                 | 0.09  | 0.14  | 0.50        | 0.74  | 0.59        | 0.78  | 0.38  | 0.64  | 0.53     | 0.79  | 0.37  | 0.61  | 0.49        | 0.75  | <b>0.75</b> | 0.93  |
| PowerCons             | 0.26  | 0.43  | 0.77        | 0.98  | <b>0.80</b> | 1.00  | 0.77  | 0.98  | 0.77     | 0.99  | 0.77  | 0.99  | 0.77        | 0.99  | <b>0.80</b> | 1.00  |
| GunPoint              | 0.10  | 0.28  | <b>0.84</b> | 0.96  | 0.60        | 0.78  | 0.66  | 0.86  | 0.90     | 1.00  | 0.72  | 0.86  | <b>0.84</b> | 0.98  | <b>0.96</b> | 1.00  |
| Adiac                 | 0.01  | 0.02  | <b>0.37</b> | 0.50  | 0.12        | 0.21  | 0.32  | 0.42  | 0.27     | 0.41  | 0.31  | 0.41  | 0.36        | 0.50  | <b>0.57</b> | 0.71  |
| Epilepsy              | 0.18  | 0.26  | 0.74        | 0.88  | <b>0.80</b> | 0.91  | 0.65  | 0.82  | 0.38     | 0.47  | 0.58  | 0.79  | 0.70        | 0.83  | <b>0.83</b> | 0.91  |

Table 4.5: The accuracy comparison for six PSED-guided distance measures of the ten datasets

| Dataset               | DTW <sup>PSED</sup> |       |             |       | ADTW <sup>PSED</sup> |       |       |       | DDTW <sup>PSED</sup> |             |             |       | shapeDTW <sup>PSED</sup> |       | WDDTW <sup>PSED</sup> |       | WDTW <sup>PSED</sup> |       |
|-----------------------|---------------------|-------|-------------|-------|----------------------|-------|-------|-------|----------------------|-------------|-------------|-------|--------------------------|-------|-----------------------|-------|----------------------|-------|
|                       | $P@1$               | $P@3$ | $P@1$       | $P@3$ | $P@1$                | $P@3$ | $P@1$ | $P@3$ | $P@1$                | $P@3$       | $P@1$       | $P@3$ | $P@1$                    | $P@3$ | $P@1$                 | $P@3$ | $P@1$                | $P@3$ |
| SonyAIBORobotSurface1 | 0.53                | 0.64  | 0.64        | 0.76  | <b>0.37</b>          | 0.53  | 0.65  | 0.76  | <b>0.38</b>          | 0.53        | 0.53        | 0.65  |                          |       |                       |       |                      |       |
| ECG200                | 0.73                | 0.84  | 0.80        | 0.88  | <b>0.54</b>          | 0.68  | 0.81  | 0.88  | <b>0.53</b>          | 0.69        | 0.73        | 0.84  |                          |       |                       |       |                      |       |
| MedicalImages         | 0.66                | 0.78  | 0.76        | 0.88  | 0.51                 | 0.69  | 0.74  | 0.88  | 0.51                 | 0.70        | 0.66        | 0.79  |                          |       |                       |       |                      |       |
| CBF                   | 0.90                | 1.00  | 0.93        | 1.00  | 0.73                 | 0.93  | 0.93  | 0.97  | 0.97                 | <b>0.70</b> | 0.93        | 0.90  | 1.00                     |       |                       |       |                      |       |
| SwedishLeaf           | 0.82                | 0.92  | 0.97        | 0.99  | 0.72                 | 0.87  | 0.97  | 0.99  | 0.73                 | 0.88        | 0.82        | 0.92  |                          |       |                       |       |                      |       |
| Plane                 | 0.60                | 0.80  | 0.75        | 0.94  | 0.50                 | 0.67  | 0.74  | 0.90  | 0.50                 | 0.69        | 0.59        | 0.80  |                          |       |                       |       |                      |       |
| GunPoint              | 0.86                | 1.00  | 0.96        | 1.00  | 0.72                 | 0.90  | 0.94  | 1.00  | 0.80                 | 0.90        | 0.88        | 1.00  |                          |       |                       |       |                      |       |
| PowerCons             | 0.78                | 0.99  | 0.79        | 1.00  | 0.79                 | 1.00  | 0.79  | 1.00  | 0.79                 | 1.00        | 0.79        | 1.00  |                          |       |                       |       |                      |       |
| Adiac                 | <b>0.33</b>         | 0.45  | 0.57        | 0.71  | <b>0.21</b>          | 0.34  | 0.53  | 0.70  | <b>0.20</b>          | 0.33        | <b>0.34</b> | 0.45  |                          |       |                       |       |                      |       |
| Epilepsy              | 0.77                | 0.88  | <b>0.78</b> | 0.88  | 0.66                 | 0.79  | 0.74  | 0.89  | 0.66                 | 0.82        | 0.80        | 0.89  |                          |       |                       |       |                      |       |

For the remaining nine datasets, we fix the parameters at  $P = 3$  and  $l = 1.5$ . We have the following findings from the previous experiment:

Table 4.6: The number of distance calls and runtime on PSED\_vanilla and PSED\_parallel\_bsf of the ten datasets

| Name                  | Size | Length | PSED_vanilla | PSED_parallel_bsf | % distance calls pruned | Speed Up |
|-----------------------|------|--------|--------------|-------------------|-------------------------|----------|
|                       |      |        | Time (s)     | Time (s)          |                         |          |
| SonyAIBORobotSurface1 | 601  | 70     | 697          | 69                | 90.40%                  | 10.10X   |
| ECG200                | 100  | 96     | 91           | 3                 | 91.08%                  | 30.33X   |
| MedicalImages         | 381  | 99     | 2082         | 40                | 96.03%                  | 52.05X   |
| CBF                   | 30   | 128    | 43           | 2                 | 75.31%                  | 21.50X   |
| SwedishLeaf           | 500  | 128    | 16601        | 107               | 96.24%                  | 155.15X  |
| Plane                 | 105  | 144    | 621          | 6                 | 96.05%                  | 103.50X  |
| PowerCons             | 180  | 144    | 3629         | 49                | 82.32%                  | 74.06X   |
| GunPoint              | 50   | 150    | 159          | 3                 | 89.42%                  | 53.00X   |
| Adiac                 | 390  | 175    | 23550        | 123               | 96.71%                  | 191.46X  |
| Epilepsy              | 137  | 206    | 13131        | 336               | 39.88%                  | 39.08X   |

1. From Table 4.3, PSED outperformed PSDTW in handling piecewise scaling distortions.
2. From Figure 4.10, the lower bound offered no efficiency gain for PSED.

Hence, we select PSED\_parallel\_bsf as the representative method for this evaluation. The accuracy results are presented in Table 4.4, while the results for the PSED-guided distance measures are detailed in Table 4.5. Finally, the runtime efficiency for all datasets is summarized in Table 4.6. It shows a significant speedup, ranging from 10.10X to 191.46X.

## 4.6 Concluding Remarks

In this study, we proposed a novel distance measure framework, Piecewise Scaling Distance (PSD), which relaxes the strict assumption of a single uniform scaling factor across the entire time series. We presented an exact dynamic programming (DP) algorithm to solve this problem. To enhance efficiency and prevent pathological segment alignments, we introduced a constraint version, which limits the search space of segment lengths based on given scaling factors. To enhance computational efficiency, we integrated two optimization techniques for the general PSD framework. In addition, we propose incorporating a lower-bounding strategy to accelerate PSDTW. Our experimental results demonstrate the necessity and effectiveness of PSD when identifying matches between a query  $Q$  and a candidate  $C$  under piecewise scaling distortions.

We outline several directions for future research. First, we aim to develop a lower bound specifically optimized for PSED that can improve actual runtime. Second, while the current PSDTW algorithm requires the number of segments  $P$

to be specified as a hyperparameter, it is preferable for the algorithm to determine this value adaptively. A simple heuristic is to test a range of  $P$  values and select the configuration that yields the minimum distance. Finally, we plan to investigate efficiency improvements for PSDTW. Currently, PSDTW computes dynamic time warping on two growing subsequences after scaling. While techniques for Incremental DTW [73] allow for the reuse of the accumulating cost matrix  $D$  to avoid redundant calculations, applying this to PSDTW is non-trivial. The interpolation performed before DTW fundamentally alters the subsequence structure, preventing the straightforward extension of  $D$  (e.g., by appending rows or columns) to reuse the computed  $D$  that is possible in standard DTW.

# Chapter 5

## Leveraging Nearest Neighbors for Time Series Forecasting with Matrix Profile

### 5.1 Background

Humans have made predictions since ancient times. In ancient societies, accurate predictions were important to the success of subsistence activities such as hunting, planting, and harvesting. There was a need to predict weather dynamics, such as rainfall and temperature. For example, it is crucial to plant during the period with sufficient rainfall and appropriate temperatures. Our ancestors used divination tools such as turtle shells, wooden blocks (moon blocks), or bones to make predictions. Without doubt, the accuracy was not guaranteed. Even in modern societies, prediction is still essential. Predicting traffic-jam patterns only a few hours ahead can save time by enabling the selection of an alternative route [74]. A wealth could be created by forecasting stock market trends. Predicting the future, also known as time series forecasting, is crucial.

With advances in hardware technologies, we collect enormous amounts of data from diverse sources, such as smart sensors and social media platforms, continuously in the form of time series data. A time series is an ordered sequence of measures, represented in real-valued numbers, at discrete equal-interval timestamps [75]. The vast data collections have created the era of “Big Data”, which provides a wealth of datasets for developing and deploying reliable, robust, data-driven forecasting techniques to discover patterns and extract valuable information [76]. Applications can be found in the financial sector, such as predicting

business cycles and stock market movements [77, 74, 78, 79] and the medical field, such as the status of critical patients according to their vital signs [80, 81] and the propagation of diseases such as influenza [79, 82] and COVID-19 [80, 83].

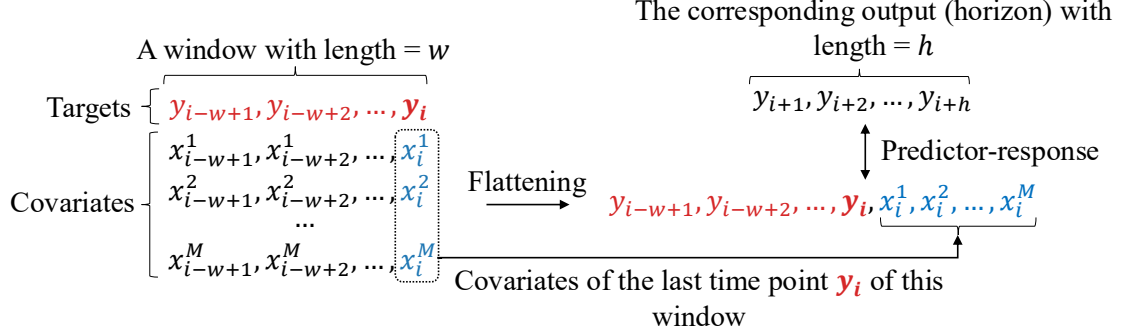


Figure 5.1: Flattening a 2D window of size  $(1 + M) \times w$  to a 1D vector of length  $w + M$ . The resulting vector serves as the *predictor* for the regressor. Its expected *response* is the vector of length  $h$ . The regressor learns from this predictor-response pair. We also call the regressor a forecaster because it aims to forecast.

A recent study [1] shows that, in time series classification, a non-parametric, instance-based method, namely nearest-neighbor classifiers (1-NN) and its generalized form  $k$ -NN, with appropriate distance measures, such as Dynamic Time Warping (DTW), despite their simplicity, perform well and are therefore commonly used as benchmarks. In detail, when a new instance is to be classified,  $k$ -NN finds its  $k$  nearest neighbors in the training set and returns their majority label among them.  $k$ -NN is considered a lazy learner because the training steps involve only memorizing all the instances verbatim; no higher-level concepts have been learned. In addition, in time series forecasting, a recent study demonstrates that a well-known machine learning baseline, Gradient Boosting Regression Tree (GBRT), such as XGBoost, equipped with an appropriate data engineering of the data, can achieve competitive or even superior performance than the deep learning method. In detail, they transform the time series forecasting task into a window-based regression problem, as shown in Figure 5.1. For each training window of length  $w$  with the last time point  $\mathbf{y}_i$ , and its lagged values  $\mathbf{y}_{i-1}, \mathbf{y}_{i-2}, \dots, \mathbf{y}_{i-w+1}$  are concatenated with covariates  $x_i^1, x_i^2, \dots, x_i^M$  of  $\mathbf{y}_i$  to form a *predictor* for a multi-output GBRT. This transformation is called flattening. Note that the standard GBRT returns only a single output. We employ a variant, multi-output GBRT, in this study. The corresponding *response* is the following  $h$  points of  $\mathbf{y}_i$ . It provides a simple, more efficient yet accurate method for time series forecasting.

Moreover,  $k$ -NN has also shown to be a promising method for time series forecasting [84]. The  $k$ -NN uses the  $w - 1$  lagged values of the last time point to form a

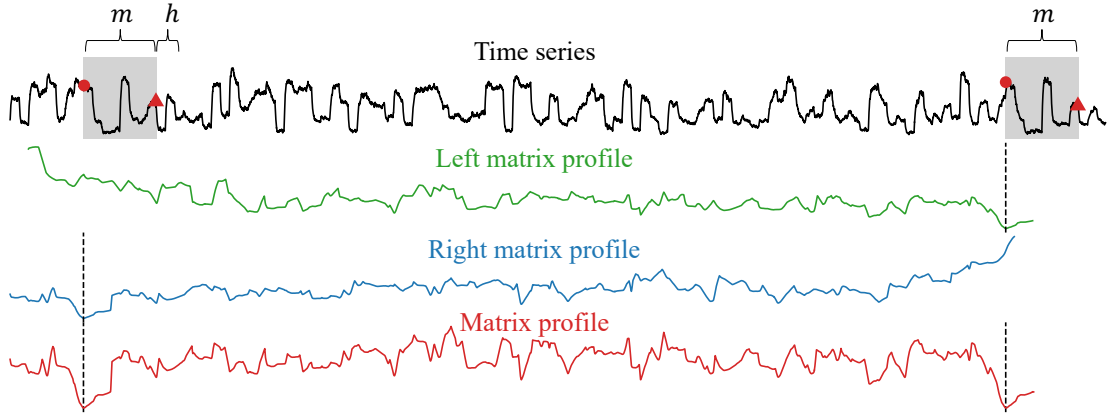


Figure 5.2: The **left** (**right**) matrix profile and the **matrix profile** of a time series. The **matrix profile** shows the distances between each  $m$ -subsequence and its nearest neighbor, where  $m$  is a user-given value. The **left** (**right**) matrix profile shows the same information but is limited to its left (right) nearest neighbor. For a particular  $m$ -subsequence shown by the right gray box, its nearest neighbor is the left gray box, as indicated by the dashed line in the **left matrix profile** and the **matrix profile**. Similarly, the nearest neighbor of the left gray box is the right gray box, as indicated by the dashed line in the **right matrix profile** and the **matrix profile**. The first (last) point in each box is denoted by a red circle (triangle).  $h$  denotes the length of the immediate subsequence of the nearest neighbor. Intuitively, this subsequence should be similar to the immediate subsequence (i.e., future) of the right gray box. To note, the **left** (**right**) matrix profile starts (ends) at a later (earlier) index because the corresponding nearest neighbor with length  $m$  does not exist.

---

**Algorithm 6** The brute force approach to compute Matrix Profile

---

- 1: **for**  $i \leftarrow 1$  **to**  $n - m + 1$  **do**
- 2:   **for**  $j \leftarrow 1$  **to**  $n - m + 1$  **do**
- 3:     Compute the z-normalized Euclidean distance between  $t_{i,m}$  and  $t_{j,m}$ .

---

query  $Q$  with length  $w$ . It identifies the  $k$  previous similar subsequences to  $Q$  and uses their immediate subsequences to predict the immediate subsequence, which is the forecasting window of length  $h$ , of  $Q$ . The intuition is that history repeats itself. The previous (historical) subsequences that are similar to  $Q$  can provide a hint about the future of  $Q$ . They are similar, and so are their immediate subsequences. Figure 5.2 depicts this idea. Observe that the immediate subsequence of the right gray box is similar to that of the left gray box. The left gray box is the nearest neighbor of the right gray in the “past”. We also refer to the left gray box as the left nearest neighbor of the right gray box.

Based on these findings, this study proposes a method to improve the performance of existing forecasters by leveraging information from the nearest neighbors

of each subsequence in the target variable  $Y$ . For each time point  $y_i$  of the target variable  $Y$ , a window of length  $w$  is constructed with  $y_i$  as the last point, then we retrieve the window’s left nearest neighbors and use their information to create new covariates for the window. The information includes the similarities between the window and its nearest neighbors, as well as the immediate subsequences of those neighbors. The similarity can be interpreted as a measure of confidence or weight in using the information from the corresponding nearest neighbor. The intuition is that, if the similarity of the window and a neighbor is high, then the future (i.e., immediate subsequence) of the neighbor should also be similar to the future of the window. The fundamental difference between this study and previous approaches [85, 84, 86] is that they directly use the subsequent points for prediction, whereas we use the nearest neighbor information for each subsequence as covariates, which are used as primitives for other forecasters. We explain this subtle difference by Figure 5.2. The previous approaches simply use the information of the nearest neighbors of the last look-back window, which consisted of the last time point and its lagged values (i.e., the right gray box), for prediction. In contrast, we use the information of the nearest neighbors of **all** of the windows.

We use the Matrix Profile [87, 88] to annotate the left nearest neighbor for each  $m$ -subsequence of a time series  $T$  of length  $n$ . The distance is the z-normalized Euclidean distance, which calculates the Euclidean distance between the two time series after they have been z-normalized to have a mean of zero and a standard deviation of one. For a time series  $T$ , the resulting z-normalized  $T'$  would have entries  $t'_i = (t_i - \mu(T)) / \sigma(T)$ , where  $\mu(T)$  and  $\sigma(T)$  are the mean and the standard deviation, of  $T$  respectively. It may seem computationally expensive to perform this annotation at first glance. Algorithm 6 shows the brute force approach to compute the matrix profile. The two for-loops and the computation of z-normalized Euclidean distance, which takes  $\mathcal{O}(m)$ , indicate that the computational complexity is  $\mathcal{O}(n^2m)$ . The space complexity is  $\mathcal{O}(n^2)$  because of the pairwise distance of each subsequence with the other subsequence. However, the matrix profile can be computed in  $\mathcal{O}(n^2)$  using an exact method, namely STOMP [87] or its community-open-sourced version, STUMP [89]. Besides, the running time can be further sped up by parallelization for a single machine with multiple computation units, such as CPUs or GPUs. The tool also allows us to compute the matrix profile to find the nearest neighbor of each window in an efficient way. Recall that we are interested in the “left” version of the matrix profile. To note, the matrix profile annotates a time series with information about the nearest neighbor of each subsequence,

including the similarity with its nearest neighbor and its location, as shown in Figure 5.2.

In this study, we make the following contributions:

- We are the first to propose leveraging the matrix profile to create meaningful covariates that improve forecaster performance.
- We have proposed two methods namely, GBRT-NN, which uses the immediate subsequence as the covariates, and GBRT-NN-S, which also involves the similarity on top of GBRT-NN, as the covariates.
- Experimental results show that our approach can improve the GBRT forecaster in most cases, with a very small cost to compute the matrix profile.

The rest of this study is organized as follows. Section 5.2 presents the related-work. In Section 5.3, we introduce the necessary background knowledge, then introduce our method. Section 5.4 contains an empirical evaluation. Finally, we conclude this study and provide future work in Section 5.5.

## 5.2 Related Work

Many methods have been developed for time series forecasting. Traditional methods include rolling averages (RA), vector auto-regression (VAR) [74, 90], and auto-regressive integrated moving averages (ARIMA) [2, 91, 90]. Because of their rigorous statistical properties, they have long been the standard. The shortcomings of ARIMA and its variants include their high computational cost [74]. In contrast, VAR is arguably the most widely used method, particularly in multivariate time series analysis, owing to its simplicity. However, most of these traditional approaches have certain limitations. They perform well when the data meet specific statistical assumptions, such as stationarity [92], which means that the mean and variance of the time series remain constant over time. It motivates the community to develop machine learning methods, particularly deep learning methods for time series forecasting. Many deep learning models have been proposed, including RNN-based models, CNN-based models, GNN-based models, Transformer-based models, and compound models that incorporate different base models mentioned before [79]. The compound models are promising. For example, RNNs are well suited to capturing long-term dependencies, whereas CNNs are well suited to capturing short-term dependencies. A good way to improve performance is to

compound them. For example, LSTnet [74] integrates CNN, RNN, and autoregressive [93] techniques to extract both short-term and long-term patterns. Using the occupancy rate of a freeway as an example [74] to explain these two patterns, the “short-term” patterns refer to the morning peaks against evening peaks, while the “long-term” patterns refer to the workday patterns against weekend patterns. Clearly, a good forecaster needs to capture and distinguish both kinds of patterns. Despite the superior performance deep learning methods have achieved, they tend to be overly complex, opaque, and incur high computational costs compared to traditional techniques.

### 5.3 Method

In this section, we first formulate the time series forecasting problem, followed by the evaluation method. We then explain how to use a Gradient Boosting Regression Tree (GBRT) for forecasting. Subsequently, we discuss how to leverage the nearest neighbors’ information of each subsequence to improve GBRT’s performance. Finally, we discuss how to compute those nearest neighbors using the Matrix Profile.

To begin, we define the data type of interest: time series.

**Definition 10** (Time series). A *time series*  $T = t_1, t_2, \dots, t_n$  is a sequence of real-valued numbers with length  $= n$ .

In Definition 10,  $T$  is a univariate time series where each entry is a scalar number. If each entry is a vector consisting of scalar numbers with size  $> 1$ ,  $T$  is a multivariate time series. A multivariate time series can be regarded as a sequence of vectors. It can also be represented as a vector of univariate time series, where each univariate time series is referred to as a channel. In a dataset with more than one time series, we use  $T_i$  to denote a time series in a dataset with  $N$  time series, where  $1 \leq i \leq N$ .

The local properties of  $T$  can be analyzed through its subsequences.

**Definition 11** (Subsequence). A *subsequence*  $T_{i,m} = T(i : i + m - 1)$  of a  $T$  is a sequence  $= t_i, t_{i+1}, \dots, t_{i+m-1} = t_{i:i+m-1}$  that consists of a continuous subset of the entries from  $T$  of length  $m$  starting from  $i$ .

### 5.3.1 Problem Formulation

Time series forecasting is the task of predicting  $h$ -future values  $y_{t+1}, y_{t+2}, \dots, y_{t+h}$  of a target  $Y$  at the current time point  $t$ . In this study, there is only one target variable  $Y$ .  $h$  is the number of steps we want to predict in the future. The simplest case is one-step-ahead forecasting, where  $h = 1$ . The predicted value is denoted as  $\hat{y}_{t+1}$  where the actual value is  $y_{t+1}$ . It is preferable to predict multiple points in the future. It is called multi-horizon (multi-step) forecasting, where  $h > 1$ . The task of forecasting is encoded in Equation 5.1.

$$\hat{y}_{t+\tau} = f(y_{t-w+1:t}, x_{t-w+1:t}, u_{t-w+1:t+\tau}, \tau) \quad (5.1)$$

where

- $\hat{y}_{t+\tau}$  is a prediction of the target value at  $t + \tau$ , where  $\tau \in \{1, 2, \dots, h\}$ .
- $y_{t-w+1:t}$  are the actual values consisting of the current value  $y_t$  and the  $w - 1$  lag values before it.  $y_{t-i}$  is called the lag of  $i$  or  $i$ -lag.
- $x_t$  are inputs that can only be known historically at time  $t$ .  $x_{t+1}$  is not known at  $t$ .
- $u_t$  are known inputs for all time. For example, the date information such as the day of the week or month [92]. Even at  $t$ ,  $u_{t+i}$  where  $1 \leq i \leq \infty$  are known. For example, given the timepoint date (2026-02-01, 14:38), we can deduce the minute (38), hour (14), day (1), month (2), and year (2026). Besides, by reading the calendar, the day of the week (Sunday), the day of the year ( $31+1=32$ ), the week of the year (the fifth week in 2026) can also be obtained.

$x_t$  and  $u_t$  are called covariates of  $y_t$ . The input of Equation 5.1, except  $\tau$ , is a look-back window  $w$ .

We explain the task of forecasting in terms of Equation 5.1. The forecasting process estimates the value of  $y_{t+\tau}$ , denoted by  $\hat{y}_{t+\tau}$  with the aim to minimize the error function, typically represented as a function of  $y_{t+\tau} - \hat{y}_{t+\tau}$  for each  $\tau$ . It is obvious that date information is useful when the target variable depends on when the measurement is taken. For example, if the target variable is the electricity consumption rate, there is a clear pattern by month: consumption is higher during the winter and summer months, when air conditioners and heaters are used.  $x_t$  provides additional information about the state of  $y_t$ . For example,

if the target variable is the body temperature, and  $x_t$  tells us the severity of the sore throat, we may guess the body temperature will raise tomorrow.

### 5.3.2 Evaluation Method

Given a dataset  $D$  of  $N$  time series  $T_i$ , where  $1 \leq i \leq N$ , we explain how to evaluate the performance of a forecaster on  $T_i$ . The error made by the forecaster on  $D$  is simply the summation of errors made by the forecaster on each  $T_i$ . We now focus on a single time series; hence, we drop the index  $i$ .  $T$  is divided into two subsequences, namely training subsequence  $T_{\text{train}}$  and test subsequence  $T_{\text{test}}$ .

In our study, the forecaster is only allowed to train on  $T_{\text{train}}$ . Recall that we are predicting the  $h$  future values from the  $w$  values just before them. Hence, we use a sliding window of length  $w+h$  to generate the  $w$ -predictor- $h$ -response sequence in  $T_{\text{train}}$ , when the first  $w$  entries form the predictor and the last  $h$  form the response. These predictor-response pairs enable the forecaster to train on them. During the test (evaluation) phase, we do rolling forecasts. We predict based on the ground truth, not results generated from the model. It is used to prevent the accumulation of errors.

This concept is also called “Teacher forcing” in RNN [94] because the teacher’s values are “force fed” into the forecaster when we “roll” the forecaster on the  $T_{\text{test}}$  [95]. The intuition is that, suppose each question (except the first one) in an exam depends on the answers to the previous questions, rather than simply grading every answer in the end, a teacher would grade (evaluate) the answer once it is given by the student, and provide the correct answer (i.e., ground truth) to the student so he can answer the next question based on the correct answer.

To evaluate the forecaster, we used the following three evaluation metrics defined as:

- Root Mean Square Error (RMSE)

$$\text{RMSE} = \sqrt{\frac{1}{n} \sum_{i=1}^n (y_i - \hat{y}_i)^2} \quad (5.2)$$

- Weighted Absolute Percentage Error (WAPE)

$$\text{WAPE} = \frac{\sum_{i=1}^n |y_i - \hat{y}_i|}{\sum_{i=1}^n |y_i|} \quad (5.3)$$

- Mean Absolute Error (MAE)

$$\text{MAE} = \frac{1}{n} \sum_{i=1}^n |y_i - \hat{y}_i| \quad (5.4)$$

where  $n$  is the length of the time series,  $y_i$ ,  $\hat{y}_i$  is ground true value and predicted value, respectively. RMSE and MAE are widely used metrics. MAE can better reflect the actual error situation than RMSE [77]. WAPE was introduced by [96]. By rewriting Equation 5.3 to Equation 5.5, it is more obvious that it is a weighted absolute percentage error.

$$\text{WAPE} = \sum_{i=1}^n w_i \frac{|y_i - \hat{y}_i|}{|y_i|} \quad (5.5)$$

where the weights are given by

$$w_i = \frac{|y_i|}{\sum_{i=1}^n |y_i|} \quad (5.6)$$

For all of them, a lower value is better.

### 5.3.3 Gradient Boosting Regression Tree (GBRT)

Gradient boosting [97] is a boosting algorithm that ensembles a group of weak learners (usually decision trees) to make predictions. It sequentially adds learners to an ensemble, with each learner connecting its predecessor. It constructs weak learners in a way that each learner strategically corrects the predecessor's mistakes by fitting the new learner to the residual errors made by the predecessor [98, 99]. It can be used in classification and regression. In this study, we focus on its use in regression. For the usage in regression, the model is called "Gradient Boosting Regression Tree (GBRT)". Some popular optimized implementations of gradient boosting are XGBoost [100], CatBoost [101], and LightGBM [102]. In this study, we use XGBoost.

In order to apply GBRT into time series forecasting problem, we need to cast the input into an appropriate format to input into GBRT. The casting approach is similar to successful time-series forecasting models, which reconfigure the time series into windowed inputs [2]. Figure 5.1 presents the reconfiguration. For each entry of the target variable  $y_i$ , we retrieve its  $u_i$ , such as the day information from the calendar. Hence, for each  $y_i$ , it is associated with  $x_i$  and  $u_i$ . To simplify

the notation, we absorb  $u_i$  into  $x_i$ , and it is called the covariates of  $y_i$ . The 2D window, as shown on the left-hand side in Figure 5.1, with size  $w \times (1 + M)$ , where  $M$  is the total number of covariates, is flattened into a 1D array on the right-hand side with length  $w + M$ . To note, as suggested in the literature [2], only the covariates of the last time-point  $i$  are kept and appended to the final vector. By reconfiguration, we obtain the predictor-response pairs for training. In detail, the predictor is  $\textcolor{red}{y_{i-w+1}, y_{i-w+2}, \dots, y_i}$ ,  $\textcolor{blue}{x_i^1, x_i^2, \dots, x_i^M}$  where the red part refers to the current target value  $\textcolor{red}{y_i}$  and its  $w - 1$  lag values, and the blue part refers to the covariates of  $\textcolor{red}{y_i}$ . The corresponding output is  $y_{i+1}, y_{i+2}, \dots, y_{i+h}$ , with length =  $h$ . We predict the  $h$ -horizon from the  $w$ -look back window (i.e.,  $w + M$ -flattened predictor). With this predictor-response formulation, the forecasting problem becomes a multi-output regression problem. Standard XGBoost cannot return a sequence of predicted values; it only returns a single number [2]. To note, a multi-output regression problem is simply a group of single-output regression problems. In other words, XGBoost internally simply treats the prediction of  $h$ -steps as  $h$  individual problems. Hence, the final output is produced by the  $h$  individual regressors rather than by a single model. One may argue that the  $h$  regressors operate individually and hence the temporal relationship in the output sequence is lost. However, as the individual regressors are trained on the same flattened input, the prediction would still preserve the temporal relationship [2].

Our proposed method has a simple intuition. We would like to create new covariates for each time point in the time series, as in the case of using the date information to create the covariates. Given a time point  $y_i$  in  $Y$ , and a user-given  $m$ , we want to use the  $m$ -subsequence with  $y_i$  as the ending point as a query  $Q$ , and to find its left  $m$ -subsequence that is the nearest neighbor of  $Q$ . Hence, the immediate subsequence of the nearest neighbor informs us of the dynamics of the immediate subsequence of  $Q$ , which is our desired forecasting window. In Figure 5.2, the red triangle in the right gray box is  $y_i$  and the right gray box is  $Q$ . We seek its leftmost nearest neighbor, which turns out to be the left gray box. Note that we would like to perform this operation for each point  $y_j$  in the time series  $Y$ ,  $m \leq j \leq |Y|$ .

### 5.3.4 Matrix Profile

We discuss how to use a data primitive called Matrix Profile [87, 88] for this operation. In brief, a matrix profile  $P$  is a time series that annotates an input time series  $T$ , storing the z-normalized Euclidean distance between each  $m$ -subsequence

and its nearest neighbor in  $T$ . If ties happen, the nearest neighbor is chosen among them arbitrarily because of the parallel computation property. Besides, another closed related time series of  $P$ , namely the Matrix Profile Index  $I$ , stores the location of the corresponding nearest neighbor. To begin our detailed discussion, we define the distance profile of  $T$ .

**Definition 12** (Distance profile). A *distance profile*  $D_i = d_{i,1}, d_{i,2}, \dots, d_{i,n-m+1}$  of a  $T$  is a vector of the Euclidean distances between a given subsequence  $T_{i,m}$  and each subsequences in  $T$ , where  $d_{i,j}$  is the distance between  $T_{i,m}$  and  $T_{j,m}$ ,  $1 \leq i, j \leq n - m + 1$ .

The distances are measured between z-normalized time series. Equipped with the distance profile, we know all the Euclidean distances between a given subsequence  $T_{i,m}$  and each subsequences in  $T$ . From this, we define the matrix profile  $P$  and its supplementary matrix profile index  $I$  as follows.

**Definition 13** (Matrix profile). A *matrix profile*  $P = \min(D_1), \min(D_2), \dots, \min(D_{n-m+1})$  of  $T$  is a vector of Euclidean distances between every subsequence  $T_{i,m}$  of  $T$  and its nearest neighbor in  $T$ .

**Definition 14** (Matrix profile index). A *matrix profile index*  $I = I_1, I_2, \dots, I_{n-m+1}$  of  $T$  is a vector of integers, where  $I_i = j$  if  $d_{i,j} = \min D_i$ .

To retrieve a non-trivial result of the Matrix profile (index), we need to define the notion of an exclusion zone. For a given  $m$ -subsequence  $Q$ , the distance profile is zero at the location of  $Q$  (because  $Q$  must be a nearest neighbor of  $Q$ ) and close to zero just before and after it. But the corresponding  $m$ -subsequences are trivial matches of  $Q$ . We need to define a zone, namely an exclusion zone, for this region. It is defined as  $m/2$  before and after the location of  $Q$  [87]. The community implementation uses  $m/4$  instead [89].

In this study, instead of the general matrix profile (index), we are interested in the left version of it. The left version of the matrix profile informs us of the information about the left nearest neighbor of any  $m$ -subsequences in  $T$ . It is shown in Figure 5.2. The left matrix profile has high values at the beginning because it can only find the left neighbor, and there are few left subsequences initially. In contrast, the right matrix profile has low values at the beginning because there are many right subsequences there. To note, each entry  $i$  in Matrix Profile  $P_i$  is simply the minimum of  $P_i^L$  and  $P_i^R$  (i.e.,  $P_i = \min(P_i^L, P_i^R)$ ).

**Definition 15** (Left distance profile). A *left distance profile*  $D_i^L = d_{i,1}, d_{i,2}, \dots, d_{i,i-\lceil m/4 \rceil - 1}$  of  $T$  is a vector of Euclidean distances between a given subsequence

$T_{i,m}$  and each subsequence that appears before  $T_{i,m}$ . To note,  $i - \lceil m/4 \rceil - 1$  is the index location of the last eligible subsequence before  $T_{i,m}$  because of the exclusion zone.

**Definition 16** (Left matrix profile). A *left matrix profile*  $P^L = \min(D_1^L), \min(D_2^L), \dots, \min(D_{n-m+1}^L)$  of  $T$  is a vector of Euclidean distances between every subsequence  $T_{i,m}$  of  $T$  and its nearest neighbor in  $T$  before it.

**Definition 17** (Left matrix profile index). A *left matrix profile index*  $I^L$  is a vector of integers  $I_1^L, I_2^L, \dots, I_{n-m+1}^L$  of  $T$ , where  $I_i^L = j$  if  $d_{i,j} = \min D_i^L$ .

Note that the original indexing system in Matrix Profile uses the start point rather than the end point to define the subsequence. In Figure 5.2, the matrix profile is shown in the original definition. The gray boxes are associated with the start point. Hence, the red Matrix Profile starts at  $t = 1$  rather than  $t = m$ . To facilitate our discussion, from now on, we refer to Matrix Profile and its variants using the index defined on the end point instead of the start point. Formally, we use the entries of Matrix Profile at  $i - m + 1$  to be the matrix profile at  $i$  in our indexing system. Visually speaking, we shift the matrix profile to the right by  $m - 1$ .

To conclude this part, given the left matrix profile (index), we can compute, for each  $m$ -subsequence in  $T$ , the information on its left nearest neighbor, including its similarity and location. Besides, with the location (it now refers to the end point of the subsequence), we can retrieve the points after it and form the immediate subsequence with length =  $h$  of the nearest neighbor.

A natural setting for  $m$  and the size of the immediate subsequence would be the  $w$  and  $h$  as defined in Figure 5.1, respectively.

## 5.4 Experiments

The code and data are available at <https://github.com/colemanyu/matrix-profile-motif-forecasting>. To note, for all these datasets, we do not have  $x_t$ . In other words, we lack auxiliary channels. However, each time point contains a timestamp. From it, we can infer the covariates associated with the timestamp. We refer to them as the original covariates.

In this study, we focus on univariate time series forecasting. There is only one single target variable  $Y$ . We predict the future of  $Y$  only based on the past of it. The dataset used is listed in Table 5.1. For each time series  $T$  in the

Table 5.1: Dataset Statistics.  $N$  is the number of time series in the dataset, while  $|T| = n$  is the length of each time series. “rate” refers to the measuring rate.  $w$  is the size of the look-back window.  $h$  is the size of the forecasting window, also known as the forecasting horizon.  $T_{\text{train}}$  is the training subsequence of  $T$ .  $T_{\text{test}}$  is the test subsequence of  $T$ . To note,  $|T_{\text{train}}| + |T_{\text{test}}| = n$ .

| Dataset            | Data |        |         | Forecasting Task |                      |                     |
|--------------------|------|--------|---------|------------------|----------------------|---------------------|
|                    | $N$  | $n$    | rate    | $w, h$           | $ T_{\text{train}} $ | $ T_{\text{test}} $ |
| Electricity [103]  | 70   | 26,136 | hourly  | 24               | 25,968               | 168                 |
| Traffic [103]      | 90   | 10,560 | hourly  | 24               | 10,392               | 168                 |
| PeMSD7 [103]       | 228  | 12,672 | /5 mins | 9                | 11,232               | 1,440               |
| Exchange-Rate [74] | 8    | 7,536  | daily   | 24               | 6,048                | 1,488               |

dataset, it is split into two contiguous time series, namely  $T_{\text{train}} = T(1 : \text{split})$  and  $T_{\text{test}} = T(\text{split} + 1 : |T|)$ , where  $\text{split}$  defines the training-test split, which is shown in the column 6 in Table 5.1. To note, the  $N$  time series in a dataset are considered as multiple, independent univariate time series instead of a multivariate time series with channels =  $N$ . The settings of  $w$  and  $h$  are adopted from the original corresponding papers [2]. It is not necessary for them to be the same. The original papers of the comparison methods use this setting. So, we use the same setting for fair comparison.

The data used includes the target values in the form of lagged values, and its covariates.

GBRT-NN refers to a model that incorporates immediate sequence information. GBRT-NN-S refers to a model that incorporates immediate sequence information with the similarity information. The experimental results are shown in Table 5.2 and Table 5.3.

As shown in Table 5.2, in the case of working without original covariates, our methods can improve the performance among all three metrics, except in the case of RMSE in the Electricity dataset.

As shown in Table 5.3, in the case of working with original covariates, our methods can improve the performance among all three metrics, except in the case of RMSE in the Traffic dataset.

We note that in the Exchange-Rate dataset, our methods perform similarly to the original method GBRT. We argue that this is because, in this dataset, it depends solely on the look-back window and not on any far-away historical events.

Table 5.2: Experimental Results without original covariates (bold represents the best result and underlined represents the second best) (\* refers to the results reported from [2]).

| Dataset            | Metric | LSTNet* [74] | TRMF* [104]    | DARNN* [105] | ARIMA* [106] | GBRT [2]       | GBRT-NN      | GBRT-NN-S     |
|--------------------|--------|--------------|----------------|--------------|--------------|----------------|--------------|---------------|
| Electricity [103]  | RMSE   | 1095.309     | <u>136.400</u> | 404.056      | 181.210      | <b>136.254</b> | 142.035      | 138.354       |
|                    | WAPE   | 0.997        | <b>0.095</b>   | 0.343        | 0.310        | 0.103          | 0.101        | <u>0.100</u>  |
|                    | MAE    | 474.845      | <b>53.250</b>  | 194.449      | 154.390      | 57.929         | 56.464       | <u>55.972</u> |
| Traffic [103]      | RMSE   | 0.042        | 0.023          | 0.015        | 0.044        | <u>0.012</u>   | 0.016        | <b>0.008</b>  |
|                    | WAPE   | 0.102        | 0.161          | 0.132        | 0.594        | 0.108          | <u>0.079</u> | <b>0.037</b>  |
|                    | MAE    | 0.014        | 0.009          | 0.007        | 0.032        | 0.006          | <u>0.004</u> | <b>0.002</b>  |
| PeMSD7 [103]       | RMSE   | 55.405       | <b>5.462</b>   | 5.983        | 15.357       | 5.610          | 5.575        | <u>5.557</u>  |
|                    | WAPE   | 0.981        | <u>0.057</u>   | 0.060        | 0.183        | <b>0.051</b>   | <b>0.051</b> | <b>0.051</b>  |
|                    | MAE    | 53.336       | 3.329          | 3.526        | 10.304       | 2.984          | <u>2.965</u> | <b>2.957</b>  |
| Exchange-Rate [74] | RMSE   | <b>0.018</b> | <b>0.018</b>   | 0.025        | 0.123        | 0.020          | <u>0.019</u> | <u>0.019</u>  |
|                    | WAPE   | 0.017        | <b>0.015</b>   | 0.022        | 0.170        | <u>0.016</u>   | <b>0.015</b> | <b>0.015</b>  |
|                    | MAE    | 0.013        | <b>0.011</b>   | 0.016        | 0.101        | <u>0.012</u>   | <u>0.011</u> | <u>0.012</u>  |

Table 5.3: Experimental Results with original covariates (bold represents the best result and underlined represents the second best) (\* refers to the results reported from [2]).

| Dataset            | Metric | DeepGlo* [103] | GBRT [2]     | GBRT-NN        | GBRT-NN-S      |
|--------------------|--------|----------------|--------------|----------------|----------------|
| Electricity [103]  | RMSE   | 141.285        | 132.669      | <b>123.591</b> | <u>124.215</u> |
|                    | WAPE   | 0.094          | 0.0929       | <b>0.089</b>   | <b>0.089</b>   |
|                    | MAE    | 53.036         | 52.0232      | <b>49.606</b>  | <u>49.739</u>  |
| Traffic [103]      | RMSE   | 0.026          | <u>0.014</u> | 0.018          | <b>0.009</b>   |
|                    | WAPE   | 0.239          | 0.109        | <u>0.101</u>   | <b>0.062</b>   |
|                    | MAE    | 0.013          | 0.006        | <u>0.006</u>   | <b>0.003</b>   |
| PeMSD7 [103]       | RMSE   | 6.490          | 5.191        | <u>5.163</u>   | <b>5.156</b>   |
|                    | WAPE   | <u>0.070</u>   | <b>0.048</b> | <b>0.048</b>   | <b>0.048</b>   |
|                    | MAE    | 3.530          | 2.796        | <u>2.779</u>   | <b>2.778</b>   |
| Exchange-Rate [74] | RMSE   | 0.038          | <u>0.020</u> | <b>0.019</b>   | <b>0.019</b>   |
|                    | WAPE   | 0.038          | <u>0.016</u> | <b>0.015</b>   | <b>0.015</b>   |
|                    | MAE    | 0.029          | <b>0.012</b> | <b>0.012</b>   | <b>0.012</b>   |

## 5.5 Concluding Remarks

In this study, we present a method to augment the original time series by finding nearest neighbors and using their information as covariates for each subsequence. The information includes the similarity and the immediate subsequences. Experiment shows that the augmented data allow the existing model to have a better prediction result in the task of time series forecasting in terms of three evaluation metrics, which are RMSE, WAPE, and MAE.

### 5.5.1 Future Work

**Leveraging nearest neighbors' location information:** It would be beneficial to retrieve the nearest neighbors for each subsequence in a specific range with

respect to it. Real-world applications often require the separation of information of short-term and long-term repeating patterns for making accurate predictions [74]. Notably, the matrix profile also provides the locations of the nearest neighbors from the matrix profile index. Using this location (index) information, we can retrieve the nearest neighbors of each subsequence in a specified range with respect to it to find those “short-term” and “long-term” patterns.

**Extend to multidimensional case:** This study focuses on univariate time series forecasting, where there is a single target and no exogenous inputs. It only requires us to find one-dimensional nearest neighbors. When there are multiple targets or a single target with multiple exogenous inputs, we need to identify multidimensional nearest neighbors [107] and leverage their information for forecasting.

**Top- $k$  neighbors and motifs:** A simple extension is to consider the information not just from the nearest neighbor but from the  $k$ -nearest neighbors. Besides, we can use motifs instead of neighbors to obtain more stable “future” information for each window. Recall that a time series motif is a repeated pattern that consists of at least two occurrences. A motif can be considered as a family of nearest neighbors  $A$  nearest neighbor is a historical occurrence that instantiates this motif. The motif captures the ideal behavior. By finding the occurrences of a motif and considering their immediate subsequences, we can make a more confident guess about this motif. We outline the approach for finding members of a motif<sup>1</sup> Given a subsequence  $A$  in a time series  $T$ , we denote the left-hand side of  $A$  in  $T$  as  $T_L$ . We find  $A$ ’s nearest neighbor in  $T_L$ , denoted as  $B$ . They are the two members of a motif  $M$ . We want to identify other subsequences in  $T_L$  that belong to  $M$ . We define a threshold  $\theta = r \times \text{ED}(A, B)$ , where  $r > 1$ . The center  $M_C$  of  $M$  is defined as the average of  $A$  and  $B$ . Then, we compute the distance profile between  $M_C$  and  $T_L$ . Any part of the distance profile that is smaller than  $\theta$  points to a member of  $M$  in  $T_L$ . These members can then be added to  $M$ . After identifying all the members of  $M$  and excluding these members in the next consideration, we can find the next left nearest neighbor of  $A$  in  $T_L$ , and repeat the same process for finding the next motif. Given a set of immediate subsequences of members (occurrences) of  $M$ , we can compute a more stable immediate subsequence (future) associated with  $M$  by excluding the outliers among them or using the ensemble value, such as the mean or median of them, to cancel the noise.

**Identify outliers of immediate subsequences:** When we have a set of immediate subsequences, we can determine whether an immediate subsequence is an outlier or not by comparing it with others. We provide a heuristic to identify an

---

<sup>1</sup>The idea has been mentioned in <https://www.cs.ucr.edu/~eamonn/TimeSeriesMotifs/>.

outlier as follows. Recall that the length of a nearest neighbor and its immediate subsequence is  $m$  and  $h$ , respectively. We concatenate all nearest neighbors into a single long time series  $T'$ . To establish a clear boundary, we append a NaN value after each of them. It ensures that all matrix profile computations do not consider subsequences that span multiple neighbors. Then, we compute a distance profile of  $T'$  to find the nearest neighbor distance  $d_i$  of each neighbor  $i$ . Let  $S_i$  be the sequence consisting of neighbor  $i$  of length  $m$  and its immediate subsequence of length  $h$ . The expected nearest neighbor distance of  $S_i$  (found within the set of all extended sequences) should be proportional to the increase in length:  $d_i \times \frac{m+h}{m}$ . If the actual nearest neighbor distance of  $S_i$  is greater than  $r' \times (d_i \times (m+h)/m)$  among the others, where  $r'$  is a user-given value, the immediate subsequence in  $S_i$  is considered as an outlier.

# Chapter 6

## Conclusion and Future Directions

In this thesis, we contribute to time series analysis by addressing three aspects, with applications in bioinformatics. The first is to frame the prediction of biological sequence problems as time series classification tasks. The second addresses a fundamental limitation in existing time series distance measures. The third is to augment the original data with the nearest neighbors of each subsequence. Models that are trained on the augmented data have a better result than models that are trained on the original data.

In the first study, we investigate the prediction of human Dicer cleavage sites. This task is important for the biogenesis of microRNAs (miRNAs). Accurate prediction of Dicer cleavage sites is crucial for elucidating mechanisms of post-transcriptional gene regulation. Computationally, this task is a classification problem. First, we curate the dataset based on existing studies. The resulting datasets are 14-strings. Then, they are transformed into time series. We employ ROCKET-based classifiers for the classification. The main contributions are summarized as follows. We are the first to frame this problem as a multivariate time series classification problem. We introduced nine encoding methods for the transformation. In the transformation, to our surprise, we are the first to use the base-pair probabilities derived from the predicted secondary structure. We employ state-of-the-art time-series classifiers, namely ROCKET-based classifiers. They use random convolutional kernels to generate the summary statistics and then use a simple ridge classifier to generate the final results. Because of the simplicity of the transformation method and the classifiers we adopted, our framework, namely MTSCCleave, is fast. It achieved predictive performance comparable to or even better than deep learning-based state-of-the-art methods. Furthermore, MTSCCleave demonstrated substantial computational efficiency, with speedups ranging from 3.7X to 28.8X relative to existing methods. We carried out perturbation-based experi-

ments to identify the subsequence that are important for the classification. We found that regions near the center of the pre-miRNA secondary structure are most critical for Dicer cleavage site determination. It aligns with the existing study. Future work for this study is as follows. We make use of the predicted secondary structure information to construct the complementary strand and the base pair probability sequence for the input strand. However, there is more than one predicted secondary structure for the given RNA sequence. One future work is to make use of all potential secondary structures, each with its own pair probability sequence, and encode this data into a multivariate time series with more channels. Another area for future work is to use interpretable time series classifiers, such as those based on time series shapelets. By doing this, we can study which subsequence is critical for the definition of the classes, namely “5p cleav”, “5p non-cleav”, “3p leav”, and “3p non-cleav” because shapelets serve as the subsequence that has the most discriminating power between classes.

The second study develops a new distance measure framework, namely PSD. It aims to release a fundamental assumption that the prior studies have overlooked. There is only one scaling rate throughout the entire time series. However, there are much data that exhibits multiple rates. For example, human motion or music performance. They consist of phases. Each phase has its own expression rate. Existing distance measures cannot account for such variations. For example, DTW is designed for handling local distortions. US assumes that there is only one scaling factor in the whole series. To address this, we introduced the Piecewise Scaling Distance (PSD) framework, the first of its kind to account for multiple scaling factors. Recall that PSD is agnostic to the base measure we used. We can use any existing distance measure as the base measure. We studied the two instantiations of it. They are PSED (using Euclidean Distance as the base measure) and PSDTW (using DTW as the base measure). We provided an exact dynamic programming solution to compute PSD and three general ways to speed it up. In particular, we proposed a constrained version of it that limits the search space based on allowed segment lengths derived from scaling factor bounds. Besides, we use parallel computing and early abandoning to further accelerate it. For PSDTW, due to its quadratic complexity, we can further speed it up using lower-bounding techniques. Experiments show that PSD, and in particular PSED, perform best when the query contains multi-rate distortions, compared with ED, DTW and the other five DTW-based methods.

Future work on it is as follows. Currently, the number of segments  $P$  is given by users. It is preferable to develop a heuristic or algorithmic approach to automat-

ically determine  $P$ . A simple heuristic is to test a range of possible  $P$ . Besides, while we have successfully applied a lower bound on PSDTW and accelerated it, the computational overhead of calculating a lower bound on PSED outweighs the pruning benefit and makes the computation slower eventually. Developing a specialized lower bound for PSED could further improve its running time. In addition, some existing works on speeding up DTW such as “incremental DTW” can reuse the accumulated cost matrix  $D$ . However, it is challenging to apply a similar method to USDTW and PSDTW due to time series interpolation.

The third study develops a new method to create covariates for time series data using the immediate subsequences of the left nearest neighbor of each forecasting windows. We have studied the effect of the length of the immediate subsequences on the forecaster. Future work of this study includes finding nearest neighbors in a specific range to capture the short pattern and long pattern, extending the framework to a multivariate time series forecasting task, using motif family instead of simply top- $k$  nearest neighbors, and handling the outliers among the immediate subsequences.



# Bibliography

- [1] M. Middlehurst, P. Schäfer, and A. Bagnall, “Bake off redux: A review and experimental evaluation of recent time series classification algorithms,” *Data Mining and Knowledge Discovery*, vol. 38, no. 4, pp. 1958–2031, Jul. 2024.
- [2] S. Elsayed, D. Thyssens, A. Rashed, H. S. Jomaa, and L. Schmidt-Thieme, “Do we really need deep learning models for time series forecasting?” Oct. 2021.
- [3] H. Sakoe and S. Chiba, “Dynamic programming algorithm optimization for spoken word recognition,” *IEEE Transactions on Acoustics, Speech, and Signal Processing*, vol. 26, no. 1, pp. 43–49, Feb. 1978.
- [4] E. J. Keogh and M. J. Pazzani, “Derivative dynamic time warping,” in *Proceedings of the 2001 SIAM International Conference on Data Mining (SDM)*, ser. Proceedings. Society for Industrial and Applied Mathematics, Apr. 2001, pp. 1–11.
- [5] Y.-S. Jeong, M. K. Jeong, and O. A. Omitaomu, “Weighted dynamic time warping for time series classification,” *Pattern Recognition*, vol. 44, no. 9, pp. 2231–2240, Sep. 2011.
- [6] J. Zhao and L. Itti, “**shapeDTW**: Shape dynamic time warping,” *Pattern Recognition*, vol. 74, pp. 171–184, Feb. 2018.
- [7] E. Keogh, K. Chakrabarti, M. Pazzani, and S. Mehrotra, “Dimensionality reduction for fast similarity search in large time series databases,” *Knowledge and Information Systems*, vol. 3, no. 3, pp. 263–286, Aug. 2001.
- [8] B.-K. Yi and C. Faloutsos, “Fast time sequence indexing for arbitrary **Lp Norms**,” in *Proceedings of the 26th International Conference on Very Large Data Bases*, ser. VLDB ’00. San Francisco, CA, USA: Morgan Kaufmann Publishers Inc., Sep. 2000, pp. 385–394.

- [9] J. Zhao and L. Itti, “Decomposing time series with application to temporal segmentation,” in *2016 IEEE Winter Conference on Applications of Computer Vision (WACV)*, Mar. 2016, pp. 1–9.
- [10] M. Herrmann and G. I. Webb, “**Americing**: An intuitive and effective constraint for dynamic time warping,” *Pattern Recognition*, vol. 137, p. 109333, May 2023.
- [11] L. A. Urry, M. L. Cain, S. A. Wasserman, P. V. Minorsky, R. B. Orr, and N. A. Campbell, *Campbell Biology*, twelfth ed. New York, NY: Pearson, 2020.
- [12] B. Alberts, *Molecular Biology of the Cell*, 7th ed. New York: W. W. Norton & Company, 2022.
- [13] W. W. Cohen, *A Computer Scientist’s Guide to Cell Biology: A Travelogue from a Stranger in a Strange Land*. New York, NY: Springer-Verl, 2007.
- [14] Y. Lee, K. Jeon, J.-T. Lee, S. Kim, and V. N. Kim, “**MicroRNA** maturation: Stepwise processing and subcellular localization,” *The EMBO Journal*, vol. 21, no. 17, pp. 4663–4670, Sep. 2002.
- [15] S. Gu, L. Jin, Y. Zhang, Y. Huang, F. Zhang, P. N. Valdmanis, and M. A. Kay, “The loop position of **shRNAs** and **Pre-miRNAs** is critical for the accuracy of dicer processing *in vivo*,” *Cell*, vol. 151, no. 4, pp. 900–911, Nov. 2012.
- [16] Y. Feng, X. Zhang, P. Graves, and Y. Zeng, “A comprehensive analysis of precursor **microRNA** cleavage by human dicer,” *RNA*, vol. 18, no. 11, pp. 2083–2092, Nov. 2012.
- [17] I. J. MacRae, K. Zhou, and J. A. Doudna, “Structural determinants of **RNA** recognition and cleavage by dicer,” *Nature Structural & Molecular Biology*, vol. 14, no. 10, pp. 934–940, Oct. 2007.
- [18] F. Ahmed, R. Kaundal, and G. P. Raghava, “**PHDcleav**: A **SVM** based method for predicting human dicer cleavage sites using sequence and secondary structure of **miRNA** precursors,” *BMC Bioinformatics*, vol. 14, no. 14, p. S9, Oct. 2013.

- [19] Y. Bao, M. Hayashida, and T. Akutsu, “**LBSizeCleav**: Improved support vector machine (**SVM**)-based prediction of dicer cleavage sites using loop/bulge length,” *BMC Bioinformatics*, vol. 17, no. 1, p. 487, Nov. 2016.
- [20] P. Liu, J. Song, C.-Y. Lin, and T. Akutsu, “**ReCGBM**: A gradient boosting-based method for predicting human dicer cleavage sites,” *BMC Bioinformatics*, vol. 22, no. 1, p. 63, Feb. 2021.
- [21] L. Mu, J. Song, T. Akutsu, and T. Mori, “**DiCleave**: A deep learning model for predicting human dicer cleavage sites,” *BMC Bioinformatics*, vol. 25, no. 1, p. 13, Jan. 2024.
- [22] L. Mu and T. Akutsu, “**DiCleavePlus**: A transformer-based model to detect human dicer cleavage sites within cleavage patterns,” *Genes to Cells*, vol. 31, no. 1, p. e70074, 2026.
- [23] S. Griffiths-Jones, H. K. Saini, and S. van Dongen, “**miRBase**: Tools for **microRNA** genomics,” *Nucleic Acids Research*, vol. 36, no. suppl\_1, pp. D154–D158, Jan. 2008.
- [24] T. Xu, N. Su, L. Liu, J. Zhang, H. Wang, W. Zhang, J. Gui, K. Yu, J. Li, and T. D. Le, “**miRBaseConverter**: An r/bioconductor package for converting and retrieving **miRNA** name, accession, sequence and family information in different versions of **miRBase**,” *BMC Bioinformatics*, vol. 19, no. 19, p. 514, Dec. 2018.
- [25] M. J. Zvelebil, J. O. Baum, and M. Zvelebil, *Understanding Bioinformatics*. New York: Garland Science, 2008.
- [26] R. Lorenz, S. H. Bernhart, C. Höner zu Siederdissen, H. Tafer, C. Flamm, P. F. Stadler, and I. L. Hofacker, “**ViennaRNA** package 2.0,” *Algorithms for Molecular Biology*, vol. 6, no. 1, p. 26, Nov. 2011.
- [27] C. C. Aggarwal, *Data Mining: The Textbook*. Cham: Springer International Publishing, 2015.
- [28] G. Mendizabal-Ruiz, I. Román-Godínez, S. Torres-Ramos, R. A. Salido-Ruiz, and J. A. Morales, “On **DNA** numerical representations for genomic similarity computation,” *PLOS ONE*, vol. 12, no. 3, p. e0173288, Mar. 2017.
- [29] D. Anastassiou, “Genomic signal processing,” *IEEE Signal Processing Magazine*, vol. 18, no. 4, pp. 8–20, Jul. 2001.

- [30] T. Rakthanmanon, B. Campana, A. Mueen, G. Batista, B. Westover, Q. Zhu, J. Zakaria, and E. Keogh, “Searching and mining trillions of time series subsequences under dynamic time warping,” in *Proceedings of the 18th ACM SIGKDD International Conference on Knowledge Discovery and Data Mining*, ser. KDD ’12. New York, NY, USA: Association for Computing Machinery, Aug. 2012, pp. 262–270.
- [31] P. D. Cristea, “Conversion of nucleotides sequences into genomic signals,” *Journal of Cellular and Molecular Medicine*, vol. 6, no. 2, pp. 279–303, 2002.
- [32] N. Chakravarthy, A. Spanias, L. D. Iasemidis, and K. Tsakalis, “Autoregressive modeling and feature analysis of **DNA** sequences,” *EURASIP Journal on Advances in Signal Processing*, vol. 2004, no. 1, pp. 1–16, Dec. 2004.
- [33] J. Zhao, X. W. Yang, J. P. Li, and Y. Y. Tang, “**DNA** sequences classification based on wavelet packet analysis,” in *Wavelet Analysis and Its Applications*. Springer, Berlin, Heidelberg, 2001, pp. 424–429.
- [34] T. Holden, R. Subramaniam, R. Sullivan, E. Cheung, C. Schneider, G. T. Jr, A. Flamholz, D. H. Lieberman, and T. D. Cheung, “ATCG nucleotide fluctuation of deinococcus radiodurans radiation genes,” in *Instruments, Methods, and Missions for Astrobiology X*, vol. 6694. SPIE, Oct. 2007, pp. 402–411.
- [35] A. S. Nair and S. P. Sreenadhan, “A coding measure scheme employing electron-ion interaction pseudopotential (**EIIP**),” *Bioinformation*, vol. 1, no. 6, pp. 197–202, Oct. 2006.
- [36] M. Akhtar, J. Epps, and E. Ambikairajah, “On **DNA** numerical representations for period-3 based exon prediction,” in *2007 IEEE International Workshop on Genomic Signal Processing and Statistics*, Jun. 2007, pp. 1–4.
- [37] R. Zhang and C.-T. Zhang, “**Z Curves**, an intutive tool for visualizing and analyzing the **DNA** sequences,” *Journal of Biomolecular Structure and Dynamics*, vol. 11, no. 4, pp. 767–782, Feb. 1994.
- [38] J. A. Berger, S. K. Mitra, M. Carli, and A. Neri, “Visualization and analysis of **DNA** sequences using **DNA** walks,” *Journal of the Franklin Institute*, vol. 341, no. 1, pp. 37–53, Jan. 2004.

- [39] A. Bagnall, J. Lines, A. Bostrom, J. Large, and E. Keogh, “The great time series classification bake off: A review and experimental evaluation of recent algorithmic advances,” *Data Mining and Knowledge Discovery*, vol. 31, no. 3, pp. 606–660, May 2017.
- [40] A. P. Ruiz, M. Flynn, J. Large, M. Middlehurst, and A. Bagnall, “The great multivariate time series classification bake off: A review and experimental evaluation of recent algorithmic advances,” *Data Mining and Knowledge Discovery*, vol. 35, no. 2, pp. 401–449, Mar. 2021.
- [41] A. Dempster, F. Petitjean, and G. I. Webb, “**ROCKET**: Exceptionally fast and accurate time series classification using random convolutional kernels,” *Data Mining and Knowledge Discovery*, vol. 34, no. 5, pp. 1454–1495, Sep. 2020.
- [42] A. Dempster, D. F. Schmidt, and G. I. Webb, “**MiniRocket**: A very fast (almost) deterministic transform for time series classification,” in *Proceedings of the 27th ACM SIGKDD Conference on Knowledge Discovery & Data Mining*, ser. KDD ’21. New York, NY, USA: Association for Computing Machinery, Aug. 2021, pp. 248–257.
- [43] C. W. Tan, A. Dempster, C. Bergmeir, and G. I. Webb, “**MultiRocket**: Multiple pooling operators and transformations for fast and effective time series classification,” *Data Mining and Knowledge Discovery*, vol. 36, no. 5, pp. 1623–1646, Sep. 2022.
- [44] A. Dempster, D. F. Schmidt, and G. I. Webb, “**Hydra**: Competing convolutional kernels for fast and accurate time series classification,” *Data Mining and Knowledge Discovery*, vol. 37, no. 5, pp. 1779–1805, Sep. 2023.
- [45] B. W. Matthews, “Comparison of the predicted and observed secondary structure of **T4** phage lysozyme,” *Biochimica et Biophysica Acta (BBA) - Protein Structure*, vol. 405, no. 2, pp. 442–451, Oct. 1975.
- [46] J. Gorodkin, “Comparing two k-category assignments by a k-category correlation coefficient,” *Computational Biology and Chemistry*, vol. 28, no. 5, pp. 367–374, Dec. 2004.
- [47] T.-c. Fu, “A review on time series data mining,” *Engineering Applications of Artificial Intelligence*, vol. 24, no. 1, pp. 164–181, Feb. 2011.

- [48] C. Rose, B. Guenter, B. Bodenheimer, and M. F. Cohen, “Efficient generation of motion transitions using spacetime constraints,” in *Proceedings of the 23rd Annual Conference on Computer Graphics and Interactive Techniques*, ser. SIGGRAPH ’96. New York, NY, USA: Association for Computing Machinery, Aug. 1996, pp. 147–154.
- [49] Y. Li, T. Wang, and H.-Y. Shum, “**Motion Texture**: A two-level statistical model for character motion synthesis,” *ACM Trans. Graph.*, vol. 21, no. 3, pp. 465–472, Jul. 2002.
- [50] R. B. Dannenberg, W. P. Birmingham, G. P. Tzanetakis, C. P. Meek, N. P. Hu, and B. P. Pardo, “The **MUSART** testbed for query-by-humming evaluation,” *Comput. Music J.*, vol. 28, no. 2, pp. 34–48, Jun. 2004.
- [51] K.-C. Li, M. Yan, and S. Yuan, “A simple statistical model for depicting the **Cdc15**-synchronized yeast cell-cycle regulated gene expression data,” *Statistica Sinica*, vol. 12, no. 1, pp. 141–158, 2002.
- [52] G. E. A. P. A. Batista, E. J. Keogh, O. M. Tataw, and V. M. A. de Souza, “**CID**: An efficient complexity-invariant distance for time series,” *Data Mining and Knowledge Discovery*, vol. 28, no. 3, pp. 634–669, May 2014.
- [53] A. W.-C. Fu, E. Keogh, L. Y. H. Lau, C. A. Ratanamahatana, and R. C.-W. Wong, “Scaling and time warping in time series querying,” *The VLDB Journal*, vol. 17, no. 4, pp. 899–921, Jul. 2008.
- [54] Y. Shen, Y. Chen, E. Keogh, and H. Jin, “Searching time series with invariance to large amounts of uniform scaling,” in *2017 IEEE 33rd International Conference on Data Engineering (ICDE)*, Apr. 2017, pp. 111–114.
- [55] ——, “Accelerating time series searching with large uniform scaling,” in *Proceedings of the 2018 SIAM International Conference on Data Mining (SDM)*, ser. Proceedings. Society for Industrial and Applied Mathematics, May 2018, pp. 234–242.
- [56] C. C. Aggarwal and C. K. Reddy, Eds., *Data Clustering: Algorithms and Applications*, 1st ed. Boca Raton: Chapman and Hall/CRC, Aug. 2013.
- [57] P. Esling and C. Agon, “Time-series data mining,” *ACM Computing Surveys*, vol. 45, no. 1, pp. 1–34, Nov. 2012.

- [58] T. Rakthanmanon, B. Campana, A. Mueen, G. Batista, B. Westover, Q. Zhu, J. Zakaria, and E. Keogh, “Addressing big data time series: Mining trillions of time series subsequences under dynamic time warping,” *ACM Trans. Knowl. Discov. Data*, vol. 7, no. 3, pp. 10:1–10:31, Sep. 2013.
- [59] C. W. Tan, F. Petitjean, and G. I. Webb, “Elastic bands across the path: A new framework and method to lower bound **DTW**,” in *Proceedings of the 2019 SIAM International Conference on Data Mining (SDM)*, ser. Proceedings. Society for Industrial and Applied Mathematics, May 2019, pp. 522–530.
- [60] A. Shifaz, C. Pelletier, F. Petitjean, and G. I. Webb, “Elastic similarity and distance measures for multivariate time series,” *Knowledge and Information Systems*, vol. 65, no. 6, pp. 2665–2698, Jun. 2023.
- [61] S. Salvador and P. Chan, “Toward accurate dynamic time warping in linear time and space,” *Intelligent Data Analysis*, vol. 11, no. 5, pp. 561–580, Oct. 2007.
- [62] E. Keogh, T. Palpanas, V. B. Zordan, D. Gunopoulos, and M. Cardle, “Indexing large human-motion databases,” in *Proceedings of the Thirtieth International Conference on Very Large Data Bases - Volume 30*, ser. VLDB ’04. Toronto, Canada: VLDB Endowment, Aug. 2004, pp. 780–791.
- [63] D. Yankov, E. Keogh, J. Medina, B. Chiu, and V. Zordan, “Detecting time series motifs under uniform scaling,” in *Proceedings of the 13th ACM SIGKDD International Conference on Knowledge Discovery and Data Mining*, ser. KDD ’07. New York, NY, USA: Association for Computing Machinery, Aug. 2007, pp. 844–853.
- [64] Y. Zhu and D. Shasha, “Warping indexes with envelope transforms for query by humming,” in *Proceedings of the 2003 ACM SIGMOD International Conference on Management of Data*, ser. SIGMOD ’03. New York, NY, USA: Association for Computing Machinery, Jun. 2003, pp. 181–192.
- [65] F. Itakura, “Minimum prediction residual principle applied to speech recognition,” *IEEE Transactions on Acoustics, Speech, and Signal Processing*, vol. 23, no. 1, pp. 67–72, Feb. 1975.

- [66] E. Keogh and C. A. Ratanamahatana, “Exact indexing of dynamic time warping,” *Knowledge and Information Systems*, vol. 7, no. 3, pp. 358–386, Mar. 2005.
- [67] S.-W. Kim, S. Park, and W. Chu, “An index-based approach for similarity search supporting time warping in large sequence databases,” in *Proceedings 17th International Conference on Data Engineering*, Apr. 2001, pp. 607–614.
- [68] C. W. Tan, M. Herrmann, G. Forestier, G. I. Webb, and F. Petitjean, “Efficient search of the best warping window for dynamic time warping,” in *Proceedings of the 2018 SIAM International Conference on Data Mining (SDM)*, ser. Proceedings. Society for Industrial and Applied Mathematics, May 2018, pp. 225–233.
- [69] C. A. Ratanamahatana and E. Keogh, “Everything you know about dynamic time warping is wrong,” in *3 Rd International Workshop on Mining Temporal and Sequential Data (TDM-04)*. Citeseer, 2004.
- [70] H. A. Dau, A. Bagnall, K. Kamgar, C.-C. M. Yeh, Y. Zhu, S. Gharghabi, C. A. Ratanamahatana, and E. Keogh, “The **UCR** time series archive,” *IEEE/CAA Journal of Automatica Sinica*, vol. 6, no. 6, pp. 1293–1305, Nov. 2019.
- [71] M. Middlehurst, A. Ismail-Fawaz, A. Guillaume, C. Holder, D. Guijo-Rubio, G. Bulatova, L. Tsaprounis, L. Mentel, M. Walter, P. Schäfer, and A. Bagnall, “**Aeon**: A **Python** toolkit for learning from time series,” *Journal of Machine Learning Research*, vol. 25, no. 289, pp. 1–10, 2024.
- [72] N. Tatbul, T. J. Lee, S. Zdonik, M. Alam, and J. Gottschlich, “Precision and recall for time series,” in *Advances in Neural Information Processing Systems*, vol. 31. Curran Associates, Inc., 2018.
- [73] M. Leodolter, C. Plant, and N. Brändle, “**IncDTW**: An **R** package for incremental calculation of dynamic time warping,” *Journal of Statistical Software*, vol. 99, pp. 1–23, Sep. 2021.
- [74] G. Lai, W.-C. Chang, Y. Yang, and H. Liu, “Modeling long- and short-term temporal patterns with deep neural networks,” in *The 41st International ACM SIGIR Conference on Research & Development in Information Retrieval*, ser. SIGIR ’18. New York, NY, USA: Association for Computing Machinery, Jun. 2018, pp. 95–104.

- [75] C. Chatfield, *The Analysis of Time Series: An Introduction, Sixth Edition*, 6th ed. New York: Chapman and Hall/CRC, Jul. 2003.
- [76] O. Y. Al-Jarrah, P. D. Yoo, S. Muhaidat, G. K. Karagiannidis, and K. Taha, “Efficient machine learning for big data: A review,” *Big Data Research*, vol. 2, no. 3, pp. 87–93, Sep. 2015.
- [77] W. Li and K. L. E. Law, “Deep learning models for time series forecasting: A review,” *IEEE Access*, vol. 12, pp. 92 306–92 327, 2024.
- [78] N. I. Sapankevych and R. Sankar, “Time series prediction using support vector machines: A survey,” *IEEE Computational Intelligence Magazine*, vol. 4, no. 2, pp. 24–38, May 2009.
- [79] Z. Chen, M. Ma, T. Li, H. Wang, and C. Li, “Long sequence time-series forecasting with deep learning: A survey,” *Information Fusion*, vol. 97, p. 101819, Sep. 2023.
- [80] J. F. Torres, D. Hadjout, A. Sebaa, F. Martínez-Álvarez, and A. Troncoso, “Deep learning for time series forecasting: A survey,” *Big Data*, vol. 9, no. 1, pp. 3–21, Feb. 2021.
- [81] D. B. da Silva, D. Schmidt, C. A. da Costa, R. da Rosa Righi, and B. Es-kofier, “**DeepSigns**: A predictive model based on deep learning for the early detection of patient health deterioration,” *Expert Systems with Applications*, vol. 165, p. 113905, Mar. 2021.
- [82] N. Wu, B. Green, X. Ben, and S. O’Banion, “Deep transformer models for time series forecasting: The influenza prevalence case,” Jan. 2020.
- [83] F. Martínez-Álvarez, G. Asencio-Cortés, J. F. Torres, D. Gutiérrez-Avilés, L. Melgar-García, R. Pérez-Chacón, C. Rubio-Escudero, J. C. Riquelme, and A. Troncoso, “Coronavirus optimization algorithm: A bioinspired meta-heuristic based on the **COVID-19** propagation model,” *Big Data*, vol. 8, no. 4, pp. 308–322, Aug. 2020.
- [84] F. Martínez, M. P. Frías, M. D. Pérez, and A. J. Rivera, “A methodology for applying k-nearest neighbor to time series forecasting,” *Artificial Intelligence Review*, vol. 52, no. 3, pp. 2019–2037, Oct. 2019.

- [85] S. Tajmouati, B. E. L. Wahbi, A. Bedoui, A. Abarda, and M. Dakkon, “Applying k-nearest neighbors to time series forecasting: Two new approaches,” *Journal of Forecasting*, vol. 43, no. 5, pp. 1559–1574, 2024.
- [86] D. T. Thi, N. T. Phong, and N. D. Bui, “Forecast timeseries based on **Matrix Profile**,” *Journal of Informatics and Innovative Technologies (JIIT)*, 2021.
- [87] C.-C. M. Yeh, Y. Zhu, L. Ulanova, N. Begum, Y. Ding, H. A. Dau, D. F. Silva, A. Mueen, and E. Keogh, “**Matrix Profile** i: All pairs similarity joins for time series: A unifying view that includes motifs, discords and shapelets,” in *2016 IEEE 16th International Conference on Data Mining (ICDM)*. Barcelona, Spain: IEEE, Dec. 2016, pp. 1317–1322.
- [88] Y. Zhu, M. Imamura, D. Nikovski, and E. Keogh, “**Matrix Profile** vii: Time series chains: A new primitive for time series data mining,” in *2017 IEEE International Conference on Data Mining (ICDM)*, Nov. 2017, pp. 695–704.
- [89] S. M. Law, “**STUMPY**: A powerful and scalable **Python** library for time series data mining,” *Journal of Open Source Software*, vol. 4, no. 39, p. 1504, Jul. 2019.
- [90] G. E. P. Box, G. M. Jenkins, G. C. Reinsel, and G. M. Ljung, *Time Series Analysis: Forecasting and Control*. John Wiley & Sons, May 2015.
- [91] G. E. P. Box and D. A. Pierce, “Distribution of residual autocorrelations in autoregressive-integrated moving average time series models,” *Journal of the American Statistical Association*, vol. 65, no. 332, pp. 1509–1526, 1970.
- [92] B. Lim and S. Zohren, “Time-series forecasting with deep learning: A survey,” *Philosophical Transactions of the Royal Society A: Mathematical, Physical and Engineering Sciences*, vol. 379, no. 2194, p. 20200209, Feb. 2021.
- [93] G. U. Yule, “On a method of investigating periodicities in disturbed series, with special reference to Wolfer’s sunspot numbers,” *Philosophical Transactions of the Royal Society of London. Series A, Containing Papers of a Mathematical or Physical Character*, vol. 226, pp. 267–298, 1927.

- [94] R. J. Williams and D. Zipser, “A learning algorithm for continually running fully recurrent neural networks,” *Neural Computation*, vol. 1, no. 2, pp. 270–280, Jun. 1989.
- [95] K. P. Murphy, *Probabilistic Machine Learning: An Introduction*, ser. Adaptive Computation and Machine Learning. Cambridge, Massachusetts London, England: The MIT Press, 2022.
- [96] S. Kolassa and W. Schütz, “Advantages of the **MAD**/mean ratio over the **MAPE**,” *Foresight: The International Journal of Applied Forecasting*, vol. 6, pp. 40–43, 2007.
- [97] J. H. Friedman, “Greedy function approximation: A gradient boosting machine.” *The Annals of Statistics*, vol. 29, no. 5, pp. 1189–1232, Oct. 2001.
- [98] L. G. Serrano and S. Thrun, *Grokking Machine Learning*. Shelter Island: Manning, 2021.
- [99] A. Géron, *Hands-On Machine Learning with Scikit-Learn and PyTorch: Concepts, Tools, and Techniques to Build Intelligent Systems*. US: O'Reilly Media, 2025.
- [100] T. Chen and C. Guestrin, “**XGBoost**: A scalable tree boosting system,” in *Proceedings of the 22nd ACM SIGKDD International Conference on Knowledge Discovery and Data Mining*, ser. KDD '16. New York, NY, USA: Association for Computing Machinery, Aug. 2016, pp. 785–794.
- [101] A. V. Dorogush, V. Ershov, and A. Gulin, “**CatBoost**: Gradient boosting with categorical features support,” in *Workshop on ML Systems at NIPS 2017*, 2017.
- [102] G. Ke, Q. Meng, T. Finley, T. Wang, W. Chen, W. Ma, Q. Ye, and T.-Y. Liu, “**LightGBM**: A highly efficient gradient boosting decision tree,” in *Advances in Neural Information Processing Systems*, vol. 30. Curran Associates, Inc., 2017.
- [103] R. Sen, H.-F. Yu, and I. S. Dhillon, “Think globally, act locally: A deep neural network approach to high-dimensional time series forecasting,” in *Advances in Neural Information Processing Systems*, vol. 32. Curran Associates, Inc., 2019.

- [104] H.-F. Yu, N. Rao, and I. S. Dhillon, “Temporal regularized matrix factorization for high-dimensional time series prediction,” in *Advances in Neural Information Processing Systems*, vol. 29. Curran Associates, Inc., 2016.
- [105] Y. Qin, D. Song, H. Cheng, W. Cheng, G. Jiang, and G. W. Cottrell, “A dual-stage attention-based recurrent neural network for time series prediction,” in *Proceedings of the 26th International Joint Conference on Artificial Intelligence*, ser. IJCAI’17. Melbourne, Australia: AAAI Press, Aug. 2017, pp. 2627–2633.
- [106] S. Makridakis and M. Hibon, “**ARMA** models and the **Box–Jenkins** methodology,” *Journal of Forecasting*, vol. 16, no. 3, pp. 147–163, 1997.
- [107] C.-C. M. Yeh, N. Kavantzas, and E. Keogh, “**Matrix Profile vi**: Meaningful multidimensional motif discovery,” in *2017 IEEE International Conference on Data Mining (ICDM)*, Nov. 2017, pp. 565–574.